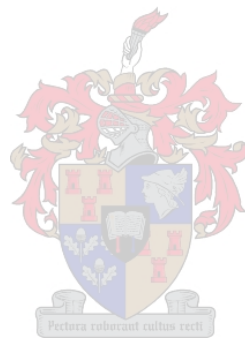


*The Design, Development and Vibration Analysis
of a High-speed Aerostatic Bearing*

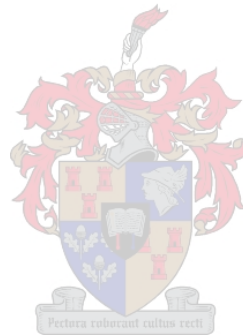


D.A. Frew
23rd November 2006

The Design, Development and Vibration Analysis of a High-speed Aerostatic Bearing

David Anthony Frew

Thesis presented in partial fulfilment of the requirements for the degree of Master of
Engineering Science (Mechanical) at the University of Stellenbosch



Supervisor: Prof. C. Scheffer

March 2007

Declaration

I, the undersigned, hereby declare that the work contained in this thesis is my own original work and that I have not previously in its entirety or in part submitted it at any university for a degree.

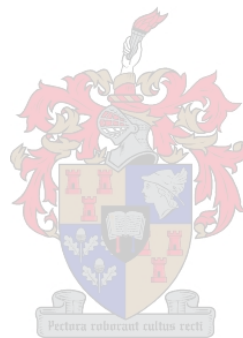
Signature:

Date: 28th February 2007



Copyright © 2007 Stellenbosch University

This report is dedicated to my father, Tony Frew, for the support he provided throughout the project and the encouragement he has given me to pursue the honorable profession of mechanical engineering.



Acknowledgements

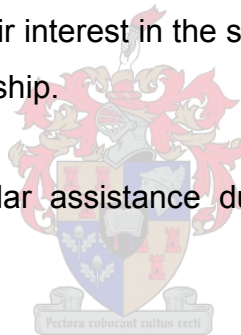
The success of this project was made possible by the generous input of many people, and the least that can be done is to give the following individuals and sponsors heartfelt thanks.

Karl Deckert, the brainchild behind the project, and a constant source of ideas and enthusiasm. His assistance during the project was invaluable.

HBD Venture #7 Pty. Ltd. for the funding made available for the prototype development.

Mike Sheridan and Norbert Leicher at Daliff Precision Engineering for the machining work they completed. They were always accommodating to any concepts being tested and their interest in the success of the project can be seen in the standard of their workmanship.

Ferdi Zietsman, for his regular assistance during the experimental testing and component manufacture.



Carl Zietsman and Anton van der Berg, for the machining work carried out, often at short notice. The effort made to complete the work as soon as possible was always greatly appreciated.

Professor W. van Niekerk, for his valuable assistance during the modal testing as well as for the use of the vibrations laboratory and equipment.

Professor S. Heyns and Abrie Oberholster at the University of Pretoria for the use of their laser vibrometer equipment as well as their assistance during the test session.

And last, but certainly not least, my study supervisor, Professor Cornie Scheffer, for making this and many other opportunities available for myself. His help, experience and enthusiasm made the project enjoyable throughout.

Table of Contents

Abstract.....	i
Opsomming.....	ii
Acknowledgements.....	iv
Table of Contents.....	v
List of Tables.....	viii
List of Figures.....	ix
Nomenclature.....	xiii
1. Introduction to Diamond Processing and the Project Objectives.....	1
2. Literature survey.....	9
2.1. Recent research in bearing concepts for the diamond saw.....	9
2.2. Recent research in gas film bearings.....	10
2.3. Recent research in high-speed rotordynamics.....	14
3. The Design of the Rotor and Aerostatic Bearing.....	17
3.1. Customer requirements for the new bearing design.....	17
3.2. Engineering requirements for the new bearing design.....	18
3.3. Bearing concepts - reasons for the use of an aerostatic bearing.....	19
3.4. General bearing description.....	20
3.5. Bearing component design.....	21
3.5.1. The journal shaft.....	21
3.5.2. The bearing bush.....	23
3.5.3. The feed jets.....	23
3.5.4. The thrust faces.....	25
3.5.5. The blade flanges.....	27
3.6. Bearing design strategy.....	29
4. Modelling of the Aerostatic Bearing and Rotor.....	33
4.1. The flexible body analysis of the rotor (Design A).....	33
4.1.1 FEM analysis of an isolated rotor – no air film.....	34
4.1.2. FEM analysis of a supported rotor – with air film.....	35
4.2. The rigid body analysis of the rotor.....	37
4.2.1. The pressure distribution within the bearing.....	37
4.2.2. The modified Euler 3-dimensional numerical model.....	39
4.2.3. Natural mode frequencies for the two rotor designs.....	42
4.2.4. The effect of rotor speed on the system frequencies.....	45

4.2.5. The effect of rotor mass, rotor inertia, bearing stiffness and the position of the centre of gravity on the system frequencies.....	46
4.2.6. The effect of imbalance on rotor motion amplitudes.....	47
4.2.7. The bearing angular stiffness.....	50
5. Experimental Modal Analysis and Results.....	55
5.1. Modal analysis experimental set up.....	55
5.2. Investigation of the flexible body modes for Design A.....	56
5.3. Investigation of the frequencies of the rigid body modes.....	57
5.3.1. The x translation (axial) mode.....	58
5.3.2. The \varnothing and θ angular (transverse) modes.....	59
5.4. Investigation of the damping of the rigid body modes.....	60
5.4.1. The x translation (axial) mode.....	62
5.4.2. The \varnothing and θ angular (transverse) modes.....	64
5.4.3. The y and z translation (radial) modes.....	65
5.5. Rotor amplitude investigation.....	69
5.6. Sawing tests – vibration levels for the conventional and aerostatic machines.....	70
5.7. Operational runs – housing vibration for motor and turbine drive.....	73
6. Conclusions and Recommendations.....	75
6.1. The FEM analysis, Euler rigid body model and EMA.....	75
6.2. An improved bearing and rotor design – Design C.....	76
6.3. The design of the surrounding components.....	79
6.4. The diamond sawing process.....	80
6.5. Possible further investigation – EMA on rotating components.....	80
References.....	81
Bibliography.....	85
Appendix A: Formula Derivation for the Rotor Modelling.....	A1
A1. The model basis.....	A1
A2. The Euler modified equation of motion.....	A2
A2.1. Transformation equations.....	A2
A2.2. The frame and body velocities.....	A3
A2.3. Euler's modified rotational equations of motion.....	A3
A2.4. Euler's modified translational equations of motion.....	A6
A3. The forces applied to the rotor.....	A7
A3.1. The turbine-drive forces.....	A7
A3.2. The normal cutting force on the blade.....	A9
A3.3. The friction force due to cutting.....	A9

A3.4. The force components of the imbalance in the rotor.....	A10
A3.5. The weight of the rotor.....	A10
A3.6. The forces due to the air stiffness.....	A10
A3.6.1. Derivation of the spring stiffness distribution.....	A11
A3.6.2. Even number of springs used for the model.....	A12
A3.6.3. Odd number of springs used in the model.....	A12
A3.6.4. Spring forces due to translation y and rotation \emptyset	A13
A3.6.5. Spring forces due to translation z and rotation θ	A14
A3.7. Spring stiffness – axial.....	A15
A3.8. Damping forces.....	A15
A3.8.1. Damping forces due to translational velocity \dot{y} and angular velocity $\dot{\emptyset}$	A15
A3.8.2. Damping forces due to translational velocity \dot{z} and angular velocity $\dot{\theta}$	A16
A3.9. Damping forces – axial.....	A17
A3.10. Translation of rotor (mass $M-m$).....	A17
A4. The moments applied to the rotor.....	A18
A4.1. Moments due to the turbine drive.....	A18
A4.2. Moment due to cutting force.....	A19
A4.3. Moment due to the frictional force.....	A19
A4.4. Moment due to rotor imbalance.....	A20
A4.5. Moments due to spring forces.....	A20
A4.5.1. Moment due to translation y and rotation \emptyset	A20
A4.5.2. Moment due to translation z and rotation θ	A21
A4.6. Moments due to damping forces.....	A22
A4.6.1. Moment due to translational velocity \dot{y} and angular velocity $\dot{\emptyset}$	A22
A4.6.2. Moment due to translational velocity \dot{z} and angular velocity $\dot{\theta}$	A23
A4.7. Rotation of the rotor.....	A23
Appendix B: Aerostatic Bearing Design Calculations.....	B1
B1. The input parameters.....	B1
B2. The approximate load capacities from bearing dimensions.....	B1
B3. The approximate bearing flow rate.....	B2
B4. The simple jet size from the MRC.....	B3
B5. The annular jet size from the MRC.....	B4

B6. The theoretical load capacity – the load coefficient C_j	B4
B7. The theoretical flow rate.....	B5
B8. The theoretical pressure drop over the jet.....	B6
B9. The axial bearing load capacity and stiffness.....	B7
Appendix C: Computer Programs.....	C1
C1. Bearing design program.....	C1
Appendix D: Experimental Data.....	D1
D1. Sawing tests.....	D1
D2. Specifications of equipment used in the EMA.....	D2

List of Tables

Chapter 3

Table 3.1: Bearing design specifications.....	30
Table 3.2: Theoretical bearing performance specifications.....	31

Chapter 4

Table 4.1: Frequencies of the natural modes from FEM analysis and the Euler model.....	36
Table 4.2: The accuracy of the angular stiffness calculation as per the number of model springs.....	51

Chapter 5

Table 5.1: Damping ratio estimates from the bearing clearance ratio (Grassam and Powell, 1964).....	68
Table 5.2: RMS vibration measurements taken during sawing tests.....	72

List of Figures

Chapter 1

Figure 1.1: Flow diagram illustrating the basic steps involved in diamond preparation.....	1
Figure 1.2: The implements used in diamond cleaving.....	2
Figure 1.3: The lines marked in black ink used to denote the desired sawing plane.....	3
Figure 1.4: A typical belt-driven diamond saw in use today.....	4
Figure 1.5: A typical saw spindle with saw blades.....	5
Figure 1.6: Diamond sawing.....	6
Figure 1.7: A Bettonville COMBI Laser System – diamond sawing, bruting and shape cutting all in one.....	7
Figure 1.8: An automatic feed upgrade using a stepper motor.....	7

Chapter 2

Figure 2.1: The sliding bearing design by van Schalkwyk (2006).....	10
Figure 2.2: A cross-sectional view through a typical micro-rotor.....	11
Figure 2.3: A comparison of theoretical and experimental load capacities for an aerodynamic micro-bearing (Wong, 2002).....	11
Figure 2.4: Test set up for the micro-turbine incorporating hybrid gas bearing (Piers, 2004).....	13
Figure 2.5: The natural frequencies and damping ratio plotted against rotor speed for the rigid rotor (Friswell, 2000).....	16

Chapter 3

Figure 3.1: The graphite v-block bearings used in the conventional diamond sawing machine.....	17
Figure 3.2: The three possible design layouts for the new bearing.....	20
Figure 3.3: The generic form of the designed aerostatic bearing.....	21
Figure 3.4: Half- versus quarter-station jet positions.....	24
Figure 3.5: The effective flow areas of simple and annular jets.....	24
Figure 3.6: A sketch of a simple jet, sealed by a brass washer.....	25

Figure 3.7: The problem encountered with using an integral thrust/journal bearing surface.....	26
Figure 3.8: The various problems related to radiused bore and shaft edges.....	26
Figure 3.9: An exaggerated sketch showing that rotor contact would never be encountered with the thrust faces.....	27
Figure 3.10: Various design options regarding the front thrust face and blade flanges.....	28
Figure 3.11: The bearing design strategy.....	29
Figure 3.12: Design A in cross-section.....	32
Figure 3.13: Design B in cross-section.....	32

Chapter 4

Figure 4.1: The non-constrained FEM model.....	34
Figure 4.2: The FEM model incorporating an 'air film'.....	35
Figure 4.3: Pressure distribution in the aerostatic bearing model.....	37
Figure 4.4: Theoretical pressure and equivalent spring stiffness distribution used for modelling purposes.....	38
Figure 4.5: The rotor attached to the xyz reference frame and moving within the inertial XYZ frame.....	39
Figure 4.6: Linear coil springs used to represent the air stiffness.....	41
Figure 4.7: Solution path of the Euler simulation of the rigid rotor.....	41
Figure 4.8: The FFT of the y response for Design A (10 000 rpm).....	42
Figure 4.9: The FFT of the x response for Design A (10 000 rpm).....	43
Figure 4.10: The FFT of the y response for Design B (10 000 rpm).....	44
Figure 4.11: The FFT of the x response for Design B (10 000 rpm).....	44
Figure 4.12: The variation in the frequency of the angular modes with rotor speed (Design B, no damping).....	45
Figure 4.13: Whirl amplitude of the rotor end as a function of the residual imbalance and rotor speed – no damping assumed.....	47
Figure 4.14: Whirl amplitude of the rotor end as a function of residual imbalance and rotor speed – damping assumed.....	48
Figure 4.15: Whirl amplitude of the rotor end as a function of axial imbalance position and rotor speed – no damping assumed.....	49

Figure 4.16: Whirl amplitude of the rotor end as a function of axial imbalance position and rotor speed – damping assumed.....	49
Figure 4.17: The angular bearing stiffness plotted against the number of springs used to represent the gas film stiffness.....	50
Figure 4.18: The effect of the radial stiffness and the centre of gravity position on the angular stiffness.....	51
Figure 4.19: The effect of the position of the rotor’s centre of gravity on the angular stiffness for different spring stiffness ratios.....	52
Figure 4.20: The effect of the bearing length and the centre of gravity position on the angular stiffness.....	53
Figure 4.21: Variation of the constant H against the spring stiffness ratio Q	54
Figure 4.22: Effect of stiffness ratio and bearing length on angular stiffness.....	54

Chapter 5

Figure 5.1: Diagram illustrating the test set up for the modal analysis using impulse and random excitation.....	55
Figure 5.2: Transfer function showing the first two bending modes of the rotor.....	56
Figure 5.3: Transfer function showing the axial mode of the rotor.....	57
Figure 5.4: A transfer function for an axial impulse test on Design A.....	58
Figure 5.5: A transfer function for an axial impulse test on Design B.....	59
Figure 5.6: A transfer function for a radial impulse test on Design A.....	59
Figure 5.7: A transfer function for a radial impulse tests on Design B.....	60
Figure 5.8: A characteristic response to an axial impulse in the time domain.....	61
Figure 5.9: The half-power point method using a specific peak in the transfer function to estimate the damping of the mode.....	61
Figure 5.10: Distortion of an axial mode by a nearby housing mode.....	62
Figure 5.11: The axial damping ratios for the two rotors.....	63
Figure 5.12: The axial damping coefficients for the two rotors.....	63
Figure 5.13: The angular damping ratios for the two rotors.....	64
Figure 5.14: The angular damping coefficients for the two rotors.....	65
Figure 5.15: The $\Sigma\Sigma/s$ term plotted against the number of model springs.....	66
Figure 5.16: The radial damping coefficients for the two rotors.....	67
Figure 5.17: The radial damping ratios for the two rotors.....	68
Figure 5.18: The blade flange displacement in the y direction (10 200 rpm).....	69

Figure 5.19: The amplitude of the blade flange motion plotted against rotor speed for the y and z direction.....	70
Figure 5.20: The accelerometer placement on the conventional machine.....	70
Figure 5.21: The accelerometer placement on the aerostatic machine.....	71
Figure 5.22: An FFT of the response for a sawing test on the conventional saw at 12 000 rpm.....	71
Figure 5.23: An FFT of the response for a sawing test on the aerostatic saw at 12 000 rpm.....	72
Figure 5.24: FFT taken on Design B housing at 12 000 rpm – turbine drive.....	73
Figure 5.25: FFT taken on Design B housing at 12 000 rpm – motor drive.....	73

Chapter 6

Figure 6.1: A transfer function for an impulse test on the bare housing of Design A.....	79
--	----

Appendix A

Figure A1: The Euler 2-3-1 transformation of the xyz axes.....	A1
Figure A2: The rotor axis system xyz within the inertia axis system XYZ	A2
Figure A3: The maximum range of angles θ and ϕ	A5
Figure A4: Forces applied to the rotor.....	A7
Figure A5: The two turbine nozzle forces and the phase difference between them.....	A8
Figure A6: The resulting turbine nozzle force on the rotor.....	A9
Figure A7: Sketch of representation of air stiffness using linear coil springs.....	A10
Figure A8: The pressure and spring stiffness distribution of the bearing model.....	A11
Figure A9: Pressure distribution in bearing using an even number of springs.....	A12
Figure A10: Pressure distribution in bearing model using an odd number of springs.....	A12
Figure A11: Spring deflections caused by translation y and rotation ϕ	A13
Figure A12: Spring deflections caused by translation z and rotation θ	A14
Figure A13: Forces due to translational velocity \dot{y} and angular velocity $\dot{\phi}$	A15
Figure A14: Forces due to translational velocity \dot{z} and angular velocity $\dot{\theta}$	A16
Figure A15: Applicable dimensions of the rotor.....	A18

Nomenclature

Roman symbols

A – the cross-sectional area of the jet orifice.

a (with subscript) – the acceleration of the rotor, further designated by a subscript.

a (no subscript) – the axial distance from the centre of gravity to the position of the mass imbalance.

B – the amplitude of the oscillating turbine force.

b – the axial distance from the centre of gravity to the first turbine nozzle.

C – the radial, angular or axial damping of the air film, further designated by a subscript.

C_l – the load coefficient of the bearing.

C_d – the discharge coefficient of the bearing.

c – the axial distance from the centre of gravity to the second turbine nozzle.

D – the diameter of the journal section of the bearing.

d – the diameter of the jet orifice.

E – the mean turbine force.

e – the eccentric position of the mass imbalance away from the rotor axis.

F – a force applied to the rotor, further designated by a subscript.

f – the axial distance from the centre of gravity to the turbine face.

fr – the gas flow rate of the bearing.

g – the gravitational acceleration constant.

H – the constant used in the calculation of the angular bearing stiffness.

h – the axial distance from the centre of gravity to the blade.

I – the moment of inertia of the rotor, either transverse or polar, further designated by a subscript.

j – the axial distance from the jets to the nearest journal end.

K – the radial, angular or axial stiffness of the air film, further designated by a subscript.

K_{go} – the gauge pressure ratio of the journal section of the bearing.

k – correction factors for the bearing design.

l – a length dimension of the rotor, further designated by a subscript.

M – the mass of the rotor.

m – the mass imbalance present in the rotor.

n – the number of turbine pockets around the circumference of the turbine.

P – the pressure at a specific point in the bearing, further designated by a subscript.

Q – the ratio of the middle spring stiffness to that of the springs at each end of the journal.

R – the gas constant of the bearing gas.

r – a radius dimension of the rotor, further designated by a subscript.

s – the number of springs and dampers used to represent the air film in the Euler rigid body model.

T – the mean temperature of the bearing gas.

u – the number of jets per row of the bearing bush.

v (with subscript) – the velocity of the rotor, further designated by a subscript.

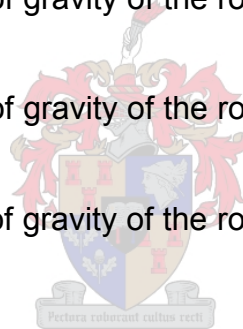
v (without subscript) – the number denoting a specific spring or damper (i.e. $v = [1:s]$).

W – the weight of the rotor.

x – the position of the centre of gravity of the rotor relative to its equilibrium position along the x axis.

y – the position of the centre of gravity of the rotor relative to its equilibrium position along the y axis.

z – the position of the centre of gravity of the rotor relative to its equilibrium position along the z axis.



Greek symbols

α – the phase difference between the two nozzles forces.

Δ – the elongation of a specific spring due to rotation of the rotor about its centre of gravity.

Σ – a term defining the damping force applied to the rotor due to rotation of the rotor as well as the damping moment applied to the rotor due to translational velocity of the rotor (defined in Appendix A).

ϵ – the eccentricity ratio of the rotor.

$\Sigma\Sigma$ – a term relating the total radial coefficient to the angular damping coefficient (defined in Appendix A).

Γ – a term defining the spring force due to rotation of the rotor as well as the spring torque applied to the rotor due to translation of the rotor (defined in Appendix A).

θ – the angle of the rotor around the y axis, relative to the rotor equilibrium position.

Φ – the angle of the rotor around the z axis, relative to the rotor equilibrium position.
 Ψ – the spin angle of the rotor around the x axis.
 ω – a general angular velocity, further designated by a subscript.
 μ – the dynamic coefficient of friction between the blade and the diamond.
 γ – the ratio of the specific heats of the bearing gas.

Subscripts

a – indicates the pressure concerned is that of the atmosphere.
ang – indicates the stiffness or damping concerned relates to the angular mode of the rotor.
ax – indicates that the stiffness or damping concerned applies to the axial direction.
b – signifies that the dimension concerned applies to the blade.
cri – *critical*, used to denote the critical damping coefficient.
cut – indicates the force concerned is the normal cutting force.
d1 – indicates the pressure concerned is that at the exit of the feed jets.
d2 – indicates the pressure concerned is that at the journal exhaust/thrust inlet.
damp – signifies the damping concerned is of a single representative damper.
fric – indicates the force concerned is due to friction.
fw1 – signifies the force concerned applies to the first turbine nozzle in the forward direction.
fw2 – signifies the force concerned applies to the second turbine nozzle in the forward direction.
j – signifies that the dimension concerned applies to the journal.
o – indicates the pressure concerned is that of the supply.
rad – indicates that the stiffness or damping concerns applies to the entire journal.
s – signifies that the dimension concerned applies to the blade flanges and thrust faces.
spr – signifies the stiffness concerned is that of a single representative spring.
t – signifies that the dimension concerns applies to the turbine.
unb – signifies that the dimension concerned applies to the imbalance mass.
v – the v^{th} spring or damper in a series of s springs.
xx – indicates the moment of inertia is that along the x axis (polar moment of inertia).

yy – indicates the moment of inertia is that along the y axis (transverse moment of inertia).

zz – indicates the moment of inertia is that along the z axis (transverse moment of inertia).

Time derivatives

' – first derivative against time (for example, \dot{x}).

** – second derivative against time (for example, \ddot{x}).

Abbreviations

DOF – Degrees of freedom

CFD – Computational fluid dynamics

CG – Centre of gravity

CVD – Chemical vapour deposition (coating)

EMA – Experimental modal analysis

FEM – Finite element methods

FRF – Frequency response function

HPP – Half-power point (method)

LD – Logarithmic decrement (method)

MAC – Mean axial clearance

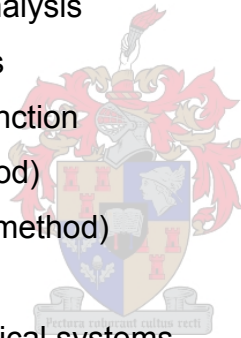
MEMS – Micro-electromechanical systems

MRC – Mean radial clearance

RMS – Root mean squared (vibration measurement)

SDOF – Single degree of freedom

TD – Thermal deposition (coating)



Abstract

This thesis examines the development of a specialized, high-speed bearing in order to reduce vibration levels, reduce cutting times and increase blade stability during diamond sawing.

The sawing process is required to be smooth, straight and unhindered – a task which is made difficult by the extreme hardness of the diamond as well as unseen grains which could potentially ruin the cut by deflecting the blade. This has an adverse effect on the quality of the cut and the yield obtained from the stone. The current equipment used for diamond sawing is very basic and a significant improvement can be made in terms of quality and sawing speed with the addition of an improved bearing.

An aerostatic bearing was designed in order to achieve lower vibration levels and increased spindle speeds. A speed of 18 500 rpm was achieved with this bearing. A numerical model of the bearing was built with the aim of predicting the bearing's dynamic behaviour. A finite element method (FEM) analysis was done to confirm the rigid body assumption made. Experimental modal analysis (EMA) was done to determine the frequencies and damping ratios of the natural modes of the rotor. The model was seen to predict the frequencies of the modes to within 6%. This model would be used for future design work to ensure that the frequencies of these modes are designed outside of the operating speed range of the aerostatic bearing.

Tests were done to compare the vibration levels between the conventional machine and the aerostatic machine during sawing. The overall RMS acceleration was reduced by 70% on the housing of the aerostatic machine and by 50% on the diamond clamp.

Opsomming

Hierdie tesis ondersoek die ontwikkeling van 'n gespesialeerde, hoë-spoed laer om vibrasie en sny tye te verminder, asook om lem stabiliteit te verhoog in die diamant sny proses.

Die sny proses moet glad, reguit en akkuraat wees, maar dit is nie altyd moontlik nie as gevolg van die variasie in hardheid van die diamant asook die naat in die daimant wat die lem maklik kan laat akwyk. Hierdie het 'n negative effek op die kwaliteit van die snit. Die konvensionele diamant saag masjien is baie eenvoudig en 'n groot verbetering in die snit kwaliteit en lemspoed is moontlik as 'n nuwe laer ontwerp en implementeer kan word.

'n Aerostatische laer en rotor is ontwikkel om die vibrasie te verminder en die lemspoed te verhoog. 'n Lemspoed van 18 500 rpm was verkry met die nuwe laer. 'n Numeriese model is ontwikkel om die beweging van die rotor dinamies te bereken. Die Eindige Element Metode (EEM) is gebruik om te bepaal of die aanname dat die rotor rigied is, wel aanvaarbaar is. Eksperimentele Modale Analise (EMA) is gebruik om die natuurlike frekwensies en die dempingsverhoudings vir die rotor te bepaal. Die model het die frekwensies tot binne 6% van die werklike waardes bereken. Hierdie model sal in die toekoms gebruik kan word vir die ontwerp van aerostatische laers om te verseker dat die natuurlike frekwensies buite die spoedbereik van die aerostatische masjien val.

Toetse is gedoen om die vibrasievlakke van die huidige en die aerostatiese masjien te meet tydens die snyproses. Die totale WGK versnelling het met 70% op die huls van die aerostatische masjien, en met 50% op die diamant dop, verminder.

Chapter 1: Introduction to Diamond Processing and the Project Objectives

The preparation of diamonds for gem use is a complex, time consuming profession that requires personnel with significant experience and skill. Only a small percentage of mined rough diamonds are suitable for gem use (the majority are impure, low grade stones suitable for industrial purposes only) and the gem producers are expected to achieve a high percentage yield with the stones that they do receive.

Each rough gem stone forms the basis for several finished products - the initial task in the preparation involves studying the rough stone to decide on the most profitable manner in which to pare it. The position for the initial cut is decided upon by the marker and drawn in ink on the stone as a guide for the person responsible for the paring. The paring is achieved by either cleaving or sawing – tasks on which the quality of the finished stone is strongly dependant. These techniques are also used to rough-cut each stone to the desired shape prior to polishing.

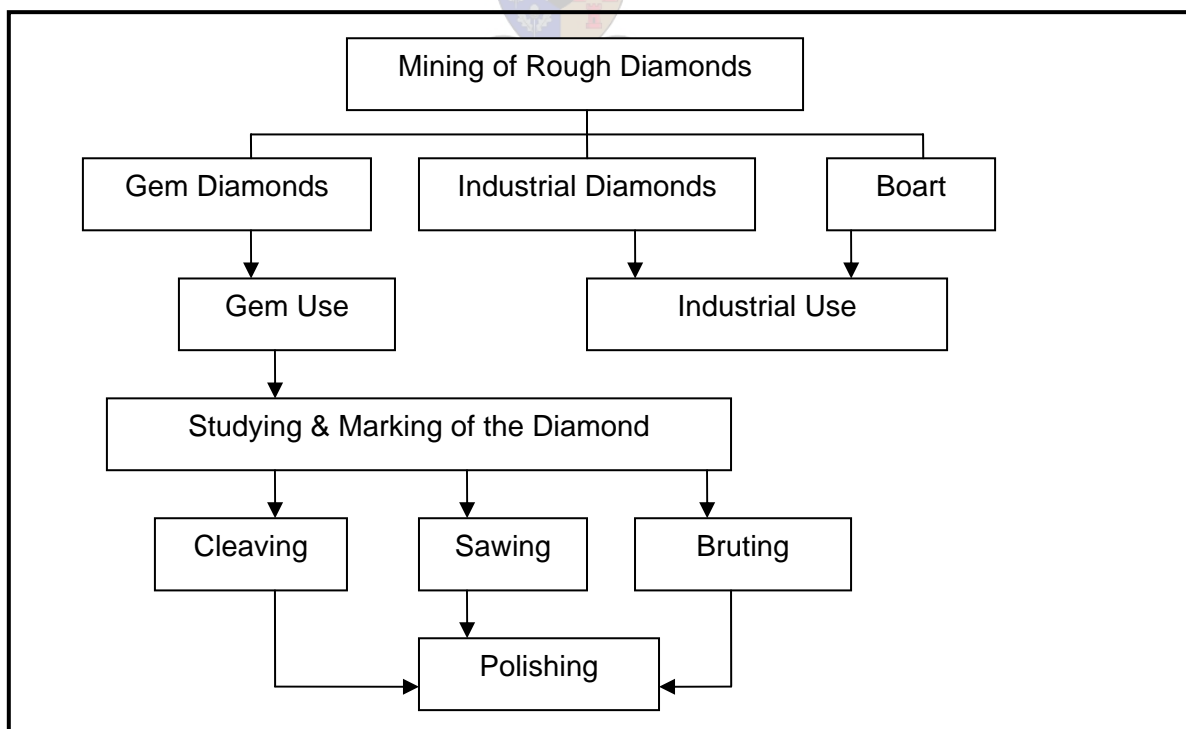


Figure 1.1: Flow diagram illustrating the basic steps involved in diamond preparation.

Diamond cleaving originating in India several centuries ago and was the first known method of shaping a rough diamond. It thrived because it was the ideal method for producing the octahedron shape, the basis for the point cut popular at the time. The continued preference of round brilliants (a specific diamond cut) caused cleaving to become almost obsolete, until a revival of the art in the 1970s due to the introduction of the Princess cut (Watermeyer, 1982).

Cleaving involves splitting the stone using a blade and mallet. The stone is cemented into a holder after which a groove, termed the *kerf*, is ground into the marked lines of a single plane, normally using the sharp edge of a sawn off stone. The blade is held in the kerf and tapped sharply using a steel rod or wooden mallet with the intention of splitting the stone cleanly along the marked lines.

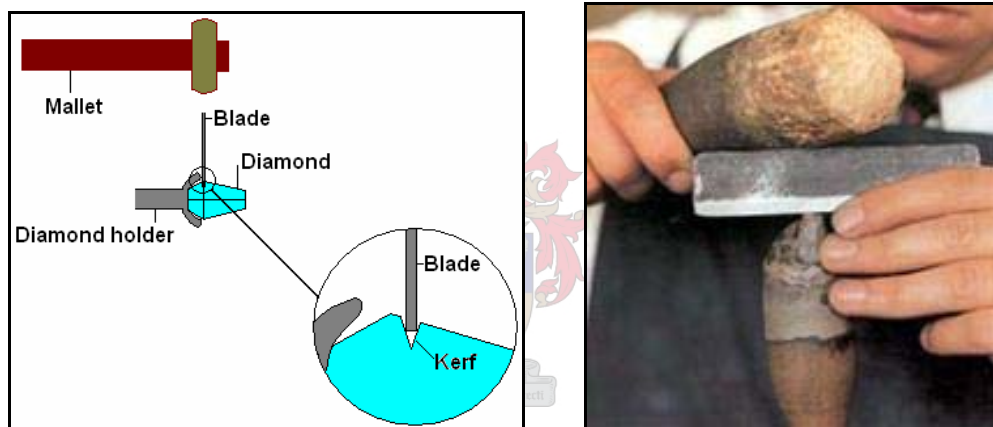


Figure 1.2: The implements used in diamond cleaving.

While sounding straightforward, cleaving is a practice requiring great precision and its success relies heavily on the experience of the cleaver. Experienced cleavers will admit that cleaving is never without risk as unknown variables such as inclusions and internal stresses in the diamond make the outcome unpredictable. The path of the fracture could easily deviate from the desired course, either shattering the stone or at least resulting in a situation from which it is difficult to salvage any good stones to work with. Cleaving is thus not as popular nowadays as sawing which, while taking significantly longer (as much as a few days), is more predictable, can be readily mechanized and does not rely as heavily on worker experience (Watermeyer, 1982).

Bruting is a process similar to metal turning on a lathe, where a work stone (termed the 'sharp') is used to shape the product stone. It is not an alternative method to cleaving or sawing (as it is not a paring method as such) but is used for general shaping before or after the paring process.

Diamond sawing originated from a method of separating diamonds using a fine wire (of brass or iron) coated in oil and diamond powder (first documented in 1823). A kerf is ground in the stone and the wire drawn repeatedly through it – teeth would eventually form on the wire by the fine diamond particles which become embedded in it. In this way the stone would be cut through, albeit very slowly with large stones taking several months to separate. The first report of circular diamond sawing, which uses a circular blade in a driven spindle, occurred in 1874, but due to the steps taken to keep the method a secret, it was 40 years later that the practice came into general use. Thus the method was never properly developed, and it is only of late that it is reaching its full potential. Circular diamond sawing is now considered a necessary task in diamond processing (Watermeyer, 1982).

The rough stones come from the marker who has marked out the specific cut line. The sawing needs to be completed accurately in terms of this line to maximise the yield from the stone. There is only one opportunity for a successful cut and any interruption to correct a deviation in the sawing line is rarely recoverable. This requires that the process be smooth and exact – a task which is complicated by the hardness of the diamond and the presence of unseen grains and imperfections which deflect the blade and ruin the cut (Wilks and Wilks, 1994). For such an important process, the sawing equipment currently available is very basic and does not produce very reliable cuts.

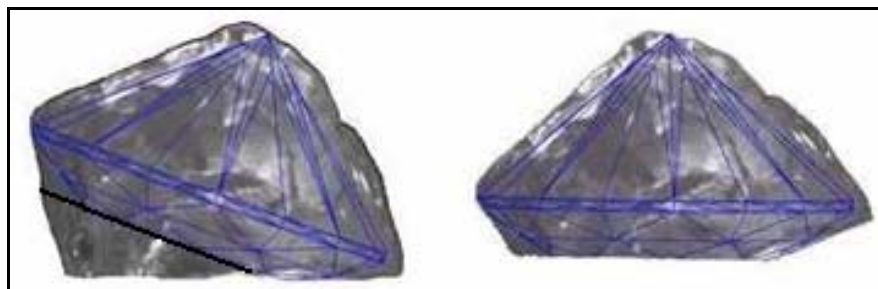


Figure 1.3: The lines marked in black ink used to denote the desired sawing plane (Lexus-com diamond equipment).

The machine, which has remained largely unchanged since the 1960's, consists of a rotating spindle and bed on which the machine arm pivots. The diamond is clamped between two cups on the machine head which is at the end of the machine arm. The adjustable machine head and bed allows the diamond to be accurately positioned above the blade. The adjustable machine head and bed allows the diamond to be accurately positioned above the blade.



Figure 1.4: A typical belt-driven diamond saw in use today.

The force of the diamond on the blade is controlled by the position of a brass ball attached to the machine arm (gravity feed) and the feed rate controlled by a rod threaded to the arm. During sawing the arm is adjusted down when the diamond cutter hears the blade running free. A soft rubber pad present on the base (and on which the adjusting rod rests) acts as a damper for the machine arm.

The hardened steel spindle rests in two graphite bearing v-blocks and is driven by an electric motor (with a power rating of between 120 W and 380 W) via a flat belt. The spindle is stepped up to speeds of between 5000 rpm and 12000 rpm (smaller stones requiring higher rotational speeds) and is able to be driven in both directions

via a reverse switch on the motor. The blocks and the belt tension control the radial position of the spindle and suitable steps on the spindle itself control the axial positioning.



Figure 1.5: A typical saw spindle, left, with saw blades, right (Bettonville, Belgium).

The phosphor-bronze blade (55 mm to 80 mm in diameter) is held between two flanges (termed *scaifes*) on the spindle. The blade varies in thickness from 0.075 mm to 0.160 mm (thicker blades are used for larger stones) and is dressed with oil and diamond dust prior to sawing. As the blade saws through the stone, the diamond particles which are released impregnate and charge the blade. Used blades normally require trimming before use, bearing in mind that enough blade material must extend beyond the flanges (the available blade annulus) in order to saw through the stone in one operation – changing blades during a sawing operation is rarely successful.

On larger stones, sawing will be initiated with a kerf blade – one that is slightly thicker than a regular saw blade. It would be only slightly larger than the flanges used to hold it (to maximise its rigidity) and its purpose is to start a groove in the diamond that the regular saw blade can follow. The kerf blade is used because a regular blade with the correct radius for the cut is not rigid enough to start the cut on its own. Once the kerf has been cut, the regular blade is inserted onto the spindle and normal sawing commences (Watermeyer, 1982).

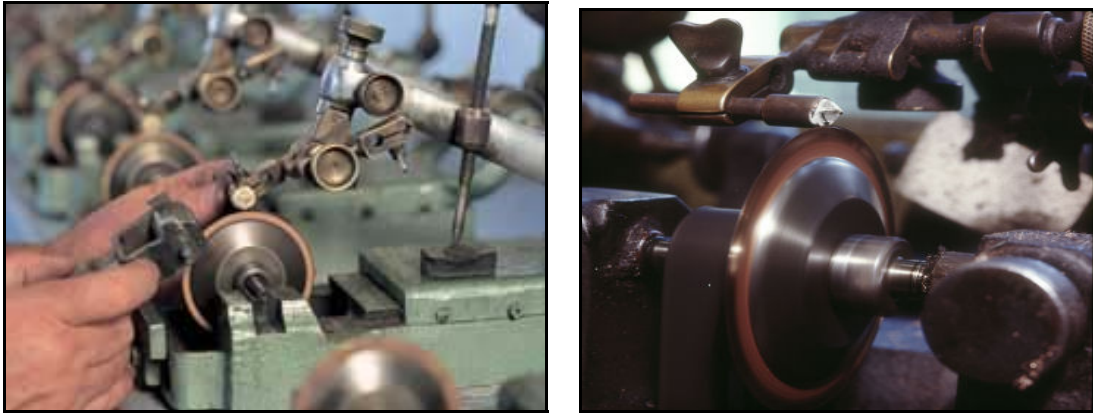


Figure 1.6: Diamond sawing (Rand Precision Cut Diamonds, South Africa).

The combination of the belt-drive and v-blocks results in a spindle that is susceptible to a high level of vibration. The v-blocks do not provide sufficient support and damping for the spindle and have a tendency to wear unevenly due to the asymmetrical position of the belt – this results in the spindle and blade losing their parallelism to the diamond sawing line. This is one of the main causes of skew-cuts which, once present, are extremely difficult to correct and very rarely result in satisfactory cuts. While this is not normally a problem with the paring of very small diamonds, it can cause serious problems with large rough stones. The use of the electric motor and belt drive also limits the rotational speed, which, due to the small blade diameter, results in a low cutting speed of approximately 30 m/s (at 7000 rpm). This results in lengthy cutting times, as much as a few weeks for medium-sized stones. The other main cause of skew cuts is that the blade is not rigid enough at these low speeds and it tends to bend if the feed force applied is too great. Another disadvantage of the design is that when the blade gets caught in a stone it is generally not noticed until the motor burns out.

It can safely be stated that, to date, no significant development work has been applied to the original diamond circular sawing equipment. There have been various small alterations carried out on the machines mostly in the areas of digital control. Technology such as computer-controlled feed rate has been successfully applied (Figure 1.8). Laser paring machines have been developed which are capable of sawing, bruting, cleaving and kerf cutting (Figure 1.7), but these machines are larger, more complex and more expensive than the original circular diamond saw which is referred to here.



Figure 1.7: A Bettonville COMBI Laser System – diamond sawing, bruting and shape cutting all in one.



Figure 1.8: An automatic feed upgrade using a stepper motor.

A specific investigation of the spindle bearing has the capacity to significantly improve the accuracy and results of diamond paring by circular sawing. Such an investigation would have to include an alternative spindle and bearing design as well as a suitable drive to reduce vibration and increase rotational speed. A study has been done on conical sliding bearings where various cone angles, materials and surface coatings were investigated (van Schalkwyk, 2006). However, some problems were encountered with wear of the bearing surfaces which could not be

resolved. Vibration levels tended to be too high and so it was decided that another look at an alternative bearing design would be beneficial.

The aim of this project was to develop a superior, high-speed bearing to replace the system used on conventional diamond sawing machines. Vibration levels and cutting times were to be reduced in order to decrease cycle times and increase production. In addition, a consistent and accurate blade position had to be ensured to facilitate accurate sawing. A higher blade speed would also increase the rigidity of the blade and help reduce the risk of skew cuts. The ultimate goal would be the elimination of skew cuts, thus ensuring a higher production yield.

This report details the design and development of a high speed rotor supported by an aerostatic bearing. Also included in the report are details of the modelling of the rotor in order to accurately predict its dynamic characteristics at high speeds (specifically natural modes and whirl magnitudes), so that stability of the sawing operation can be assured. The modelling predominantly follows the principle of rigid rotor dynamics, but a short investigation is done into flexible rotor analysis to ascertain the validity of the rigid rotor assumption. The rotor is intended to be driven by a mechanism of low vibration. The drive mechanism has been developed, but the details are beyond the scope of this report.

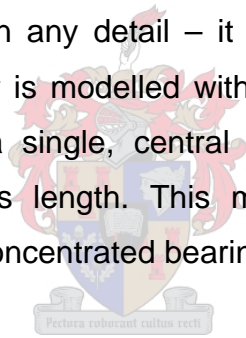
Pectora cubant cibus celi

The next chapter gives a brief review of previous research that is relevant to the project. Chapter 3 details the development of the aerostatic bearing prototypes and provides specifications for the two prototypes that were used for comparison against the rotor models. The formulation of the finite element method (FEM) and Euler rotor models is presented in Chapter 4, which also includes the results obtained from these models. Chapter 5 presents the results obtained from experimental modal analysis (EMA) of the two bearing systems, which are compared with the model predictions. The conclusions and recommendations are given in Chapter 6.

Chapter 2: Literature Survey

In this chapter, previous research relevant to the project is reviewed. Previous relevant research can be divided into two areas: aerostatic bearing design and the dynamic analysis of rotating shafts (rotordynamics). A large amount of attention has been given to both of these areas as separate fields of study. However, the amount of literature concerning the rotordynamics of aerostatic journal bearings is limited.

This in itself is not a problem as the principles of rotordynamics can readily be applied to the case of aerostatic bearings. Most of the research available focuses on either flexible shafts with a concentrated mass between two supports or the whirl of rigid shafts supported by hydrodynamic bearings (Surial and Kaushal, undated; Abulrub *et al.* 2005; Nicholas *et al.* undated; Antkowiak and Nelson, 1997). What makes this study distinct is that, contrary to hydrodynamic bearing research, it does not consider fluid dynamics in any detail – it is a rotordynamic study applied to aerostatic bearings. The rotor is modelled with a non-symmetric centre of gravity (CG) and is supported by a single, central bearing area with a non-constant stiffness distribution along its length. This makes it different to the research concerned with two or more concentrated bearing supports of specific stiffness.



2.1. Recent research in bearing concepts for the diamond saw

In order to address the requirement for reduced vibration, a new bearing concept for the diamond saw was the main focus in the early stages of the project, done by van Schalkwyk (2006). The initial concept was a spindle with conical ends which rotated within female bushes. This type of dry, sliding bearing was similar to the graphite bearings of the conventional saw and if successful would be a simple modification. Various tests were conducted with the aim of determining the most appropriate material combination of the spindle and bushes.

A tool-steel spindle with a chemical vapour deposition (CVD) coating, running in similarly coated carbide bushes tended to wear heavily after approximately 10 hours of operation, with the majority of the wear occurring on the rotor and not on the bushes which would have been preferred. An improved spindle with detachable conical ends allowed a harder thermal diffusion (TD) coating to be used.

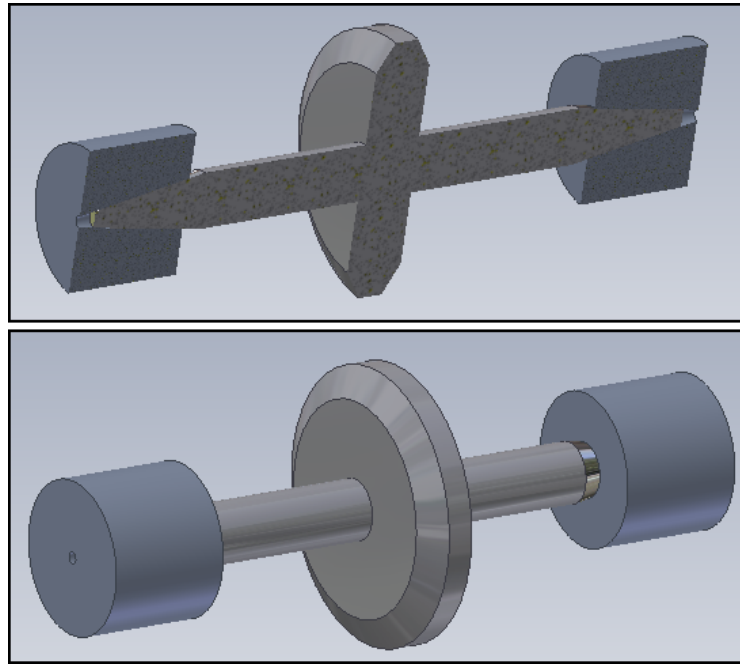


Figure 2.1: The sliding bearing design by van Schalkwyk (2006).

When run in graphite bushes no visible wear on the spindle occurred, however the graphite was too soft and brittle to be considered for the application. Ceramic bushes were more successful in terms of strength, but particles tended to break away from the bushes, wearing the coated spindle heavily (van Schalkwyk, 2006).

2.2. Recent research in gas film bearings

Much research has been done in recent years on gas film bearings for modern-technology applications. Focus has specifically been given to micro-electromechanical systems (MEMS), micro-scale machines (compressors, turbines *etc.*) for propulsion and mobile power generation *etc* (Piers *et al.* 2003). These micro-machines must rotate at very high speeds (on the order of 1×10^6 rpm) in order to achieve power densities comparable with normal-scale turbomachines, and thus low friction bearings are required. Current limitations in microfabrication techniques result in low length-to-diameter (aspect) ratios (0.1:1) compared to typical gas-film bearings in industrial applications (1:1 to 4:1). The clearance ratios are also much larger than typical gas film bearings. Figure 2.2 shows a typical micro-motor - the thin outer rim of the bearing provides radial support with thrust bearings at each end. One face would typically house either a motor or a generator.

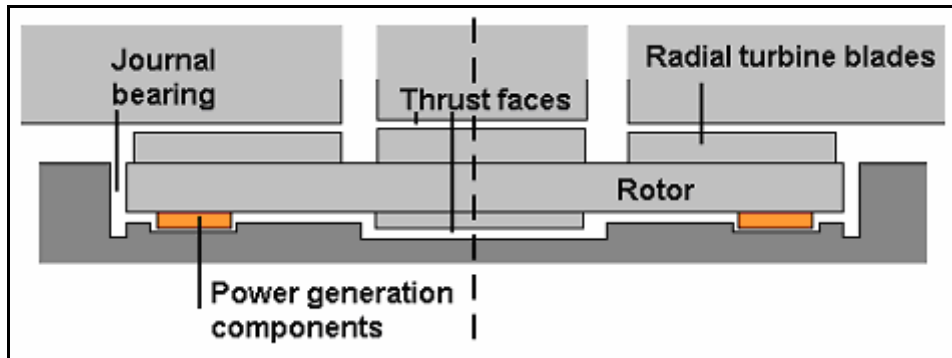


Figure 2.2: A cross-sectional view through a typical micro-rotor.

Wong *et al.* (2002) developed a self-acting (aerodynamic) bearing of 4.2 mm diameter for a high speed micro-rotor. It was successfully rotated at 450 000 rpm, driven by a micro-scale radial inflow turbine. It was suggested that without the design constraints present, more than 1×10^6 rpm would be possible. The aerodynamic principle was researched to eliminate two disadvantages present with an aerostatic bearing – the air supply requirement and the increased manufacturing complexity of using feed orifices in micro-machines.

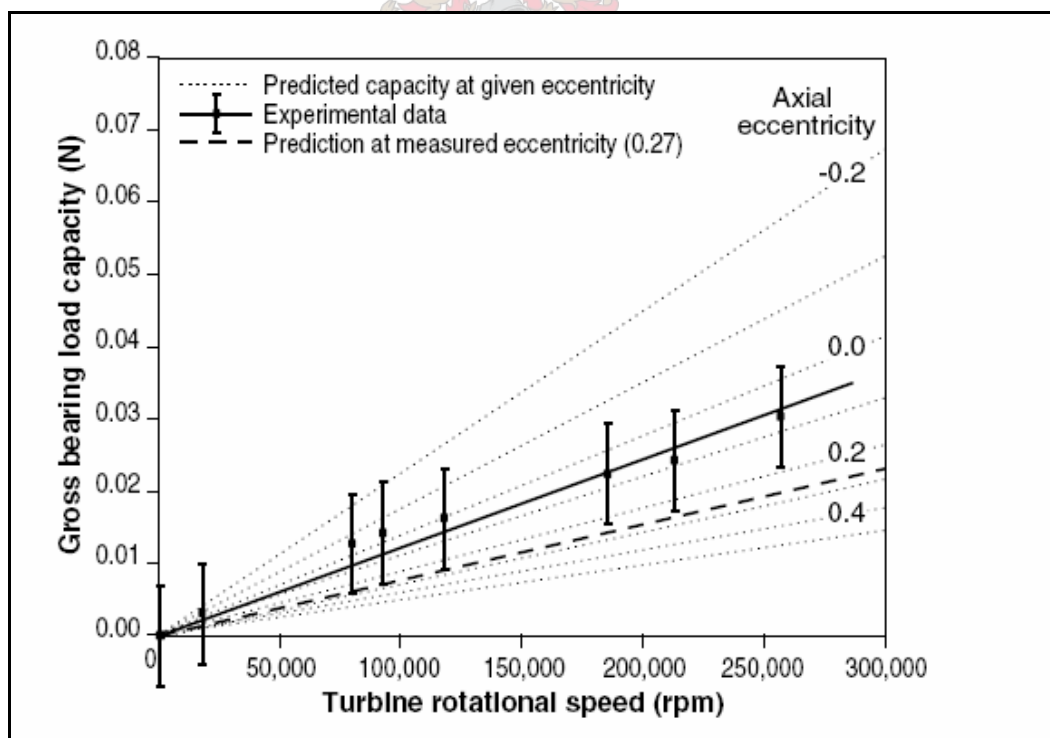


Figure 2.3: A comparison of theoretical and experimental load capacities for an aerodynamic micro-bearing (Wong, 2002).

Equations for load carrying capacity and drag (which are dependent on rotor speed) were derived. A full profile spiral groove was incorporated into the thrust face to maximise load capacity and bearing stiffness. The stiffness was proportional to the rotor speed and reached 6×10^5 N/m at 820 000 rpm (constant 3×10^5 N/m for the aerostatic bearing). It was shown that at speeds below 100 000 rpm the aerodynamic load capacity was less than that required to support the aft rotor forces (aerostatic support was used to carry the rotor above this speed). At speeds exceeding 169 0000 rpm the aerodynamic capacity alone was sufficient. The gross load carrying capacity of the bearing was approximately 50% greater than predicted by the theory, but followed the same trend with increasing speed.

A second-order, two degree of freedom (DOF) model was developed by Savoulides *et al.* (2000) to analyse the stability region and whirling frequency of a balanced micro-scale gas bearing. This model development was prompted by the inability of conventional theory and design tools to adequately model these unique bearings.

For increased stability, high and low pressure plenums were used to impart a net load on the rotor thereby displacing it radially from the bearing's geometric centre. Thus the eccentricity of the rotor could be controlled during testing. Stiffness coefficients consisted of hydrodynamic stiffness (derived from numerical simulation of the Reynolds equation) and hydrostatic stiffness (derived from a numerical model for axial flow through a short bearing, developed by Piekos). Damping coefficients were derived from the Full-Sommerfeld short-width bearing theory. The stability boundary (defined by a load parameter) plotted by the model against the bearing number showed good agreement with the compressible Reynolds equation. While the model results are slightly lower than the full numerical simulation, they are obtained much quicker, and illustrate the same trend. In conclusion, it was noted that aerostatic support was beneficial at low speeds (making start-up at the high eccentricities possible) with a transition to aerodynamic support at higher speeds.

Piers *et al.* (2004) developed a hybrid gas bearing to replace the high-speed ball-bearings in a micro-gas turbine (Figure 2.4). A maximum rotational speed of 96 000 rpm was attained with the gas bearing. In order to maximise the efficiency and output of these micro-turbines the rotational speed has to be extremely high.

The turbine's optimal speed of 210 000 rpm was not reached by the ball-bearings (maximum of 150 000 rpm), with the result that the compressor pressure ratio was less than desired.

A hybrid bearing was designed using the advantages of aerostatic bearings (stability) and aerodynamic bearings (no jacking air required). A small amount of air is tapped from a compressor to stabilise the bearing at high speeds. It was driven by a single-stage axial impulse (Laval) turbine. Tests concluded that a vertical rotor always experienced half-speed whirl. A plain, horizontal bearing with a length-to-diameter (slenderness) ratio of 1:2 showed a half-speed whirl onset speed of 9600 rpm – in agreement with tests completed by Reynolds and Gross. The whirl amplitude was noted to grow very quickly beyond the onset speed. In order to increase the onset speed of whirl, axial grooves were incorporated into the bearing surface, a single orifice feed hole was used to displace the rotor radially (greater eccentricity) and three equi-spaced orifice feed holes were incorporated to create a hybrid bearing.

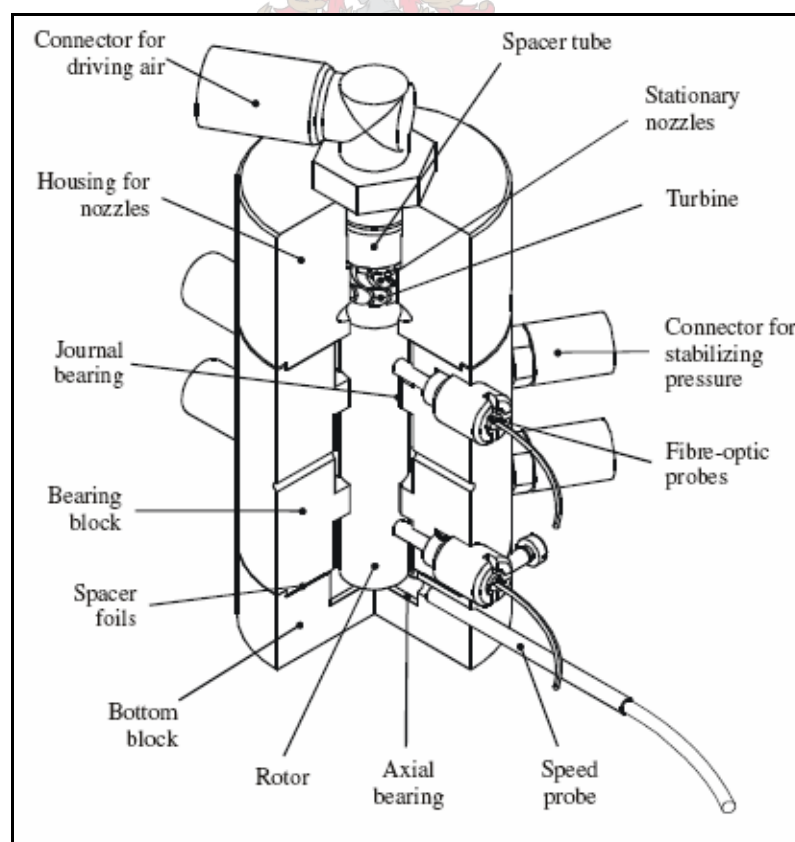


Figure 2.4: Test set up for the micro-turbine incorporating hybrid gas bearing (Piers, 2004).

The axially grooved bearing was limited to 26 000 rpm (horizontally) and 18 000 rpm (vertically). It was noted that the 26 000 rpm limit on the horizontal rotor was due to fractional-speed whirl. Starting the rotor with a single orifice feed was difficult and no reliable conclusions could be drawn. The hybrid bearing was able to reach 96 000 rpm before limited by fractional whirl.

J.P. Khatait *et al.* (2005) investigated the effect of orifice diameter, clearance, supply pressure and bearing diameter on the load capacity and stiffness of an aerostatic thrust bearing with the aim of using simple tools to build low cost, high performance air bearings. In addition, a computational fluid dynamics (CFD) analysis was done to plot the pressure distribution radially along the bearing surface. This also agreed well with the theory, except for a pressure drop at the pocket edge, which was attributed to throttling. Experimental testing showed good agreement with his analysis at large clearances, with some deviation occurring at smaller clearances.

2.3. Recent research in high-speed rotordynamics

In the past decade, new methods to increase rotational speeds and improve stability and control of rotating machinery have remained key focus areas for manufacturing, power production and aerospace industries. This has resulted in ongoing research focusing specifically in areas of high-speed rotordynamics.

G.V. Brown *et al.* (2006) developed a superior control system for magnetic bearings which support high-speed flywheels. The specific aim of the research was to stabilize the forward and backward tilt whirling modes, the frequencies of which depend on the shaft speed due to gyroscopic effects. These modes are normally unstable and exhibit low damping and thus often prevent the attainment of the desired shaft speed.

A rigid shaft was considered, treated as a free body and acted upon only by the speed dependent gyroscopic torques and the support forces from the two magnetic bearings. Only the tilt modes were considered – all of the pure translation modes were ignored. It was noted that the product of the absolute values of the frequencies was approximately constant with rotor speed and that the damping

ratios of the two modes were identical. However, the damping coefficient of the forward-whirl mode is greater than the backward-whirl mode due to the fact that the mode occurs at a higher frequency.

Cross-axis proportional gains are investigated as a superior alternative to same-axis derivative or cross-axis derivative gains in magnetic bearing control systems. Due to the tilt mode's dependency on rotor speed it is possible to completely eliminate the need for differentiation of the displacement to obtain shaft velocity. However the cross-axis proportional gain required to stabilise the forward-whirl mode destabilizes the backward-whirl mode and vice-versa. This was overcome by taking advantage of the increased difference in the frequencies of the two modes that occurs at high rotor speeds. Two parallel paths are utilized in the controller separated by high- and low-pass filters. The path using the low-pass filter stabilizes the backward-whirl mode using an appropriate signed cross-axis proportional gain, and other using the high-pass filter stabilizes the forward-whirl mode with an oppositely-signed cross-axis proportional gain.

The effectiveness of using cross-axis proportional gains was investigated in an energy storage flywheel at speeds of up to 60 000 rpm. An unfiltered cross-axis gain could only reduce the amplitude of one of the whirl modes at a time. A filtered cross-axis gain was effective in reduce the amplitude of both whirl modes simultaneously.

The research of M.I. Friswell *et al.* (2000) focused on how gyroscopic forces and bearing characteristics cause bifurcation of the natural frequencies and damping ratios of the tilt modes as the shaft rotational speed is increased. Two cases for rigid rotors were considered: one for when the bearing supports are isotropic in terms of stiffness and damping and the other where the supports display isotropic stiffness but anisotropic damping.

A theoretical derivation for the first case (isotropic damping) showed that the natural frequencies will separate but the damping ratio will stay the same for the two modes. Above a certain speed the same trend is displayed for the second case (anisotropic damping), but the behaviour is dependent on the mean of the damping

coefficients rather than on the shared damping coefficient as in the first case. This specific speed is the point at which bifurcation occurs. Below this speed the natural frequencies are equal. The damping ratios of the two modes are separate below this speed, merge at this speed and are equal above it (Figure 2.5).

A uniform rigid rotor (0.2 m diameter by 0.5 m long) supported by anisotropic bearings was analysed from rest to 500 rpm and results were as predicted, with a bifurcation speed occurring at 194.6 rpm.

A flexible shaft (0.05 m diameter by 1.5 m long) with two dissimilar discs placed at quarter positions was modelled using 6 Timosenko beam elements. Hydrostatic bearings were used to support the shaft. Results showed that at low speeds the frequencies were very close, but not equal. Bifurcation was clearly illustrated at the defined speed. However, the damping ratios did not converge after this speed and were not symmetrically placed below it. The presented theory held more for simple rigid rotors and more detailed investigation would be required for complex flexible shafts.

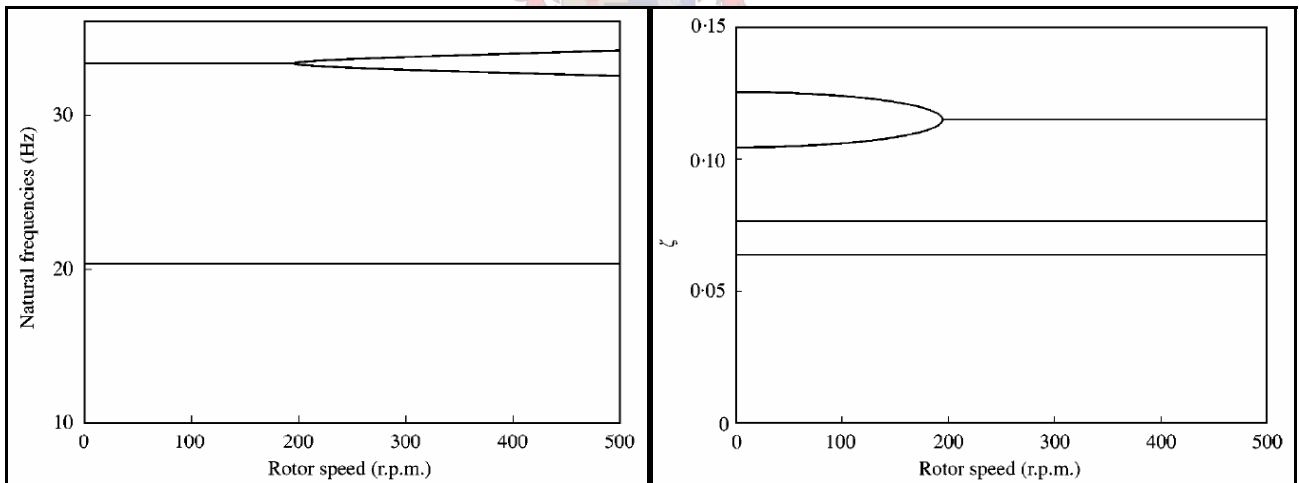


Figure 2.5: The natural frequencies and damping ratio plotted against rotor speed for the rigid rotor (Friswell, 2000).

Chapter 3: The Design of the Rotor and Aerostatic Bearing

This chapter concerns the design of the rotor and the aerostatic bearing in which it would run. It includes customer requirements and specifications for the diamond saw, general information on the bearing design as well as individual component specifications. A design strategy for the aerostatic bearing is also included.

The aerostatic bearing would replace the spindle and v-block bearing in the conventional diamond saw, and would have to be superior in terms of support stiffness and vibration suppression. In order to realize these goals certain design requirements had to be stated.

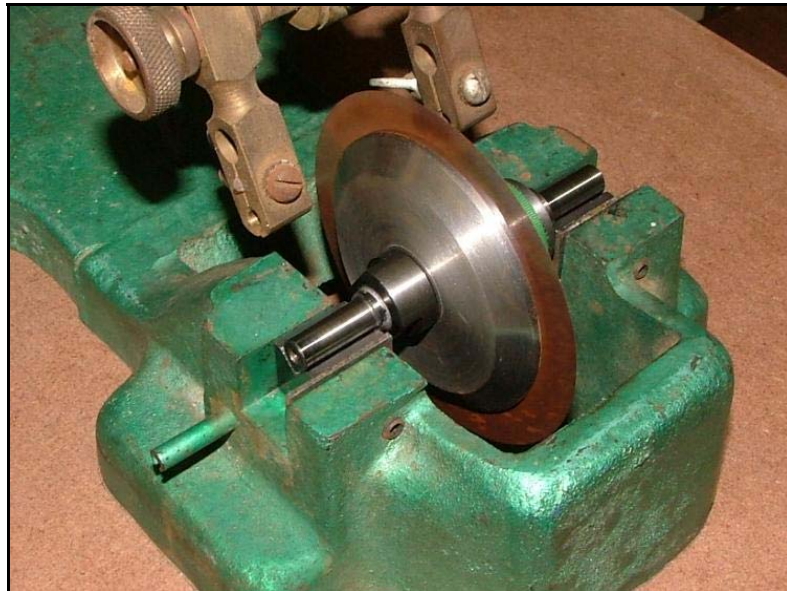


Figure 3.1: The graphite v-block bearings used in the conventional diamond sawing machine.

3.1. Customer requirements for the new bearing design

According to the customer, the new diamond saw should:

- Allow a higher rotational speed in order to decrease sawing times.
- Reduce the vibration to below that experienced with the conventional saw.
- Be compact and able to be retro-fitted in place of the conventional saw.

At the start of the project it was the wish of the customer for the new spindle to be driven by a pneumatic turbine, as it was reasoned that this drive mechanism would

combine high speeds with the lowest vibration transmission. Thus, additional customer requirements were specified for the turbine:

- The rotor should be driven in both directions by a pneumatic turbine.
- The turbine should operate off a common workshop air supply.
- The turbine should be efficient in terms of power consumption.

3.2. Engineering requirements for the new bearing design

The following engineering requirements were specified for the new saw:

- The operating speed should be increased to 20 000 rpm. The lowest natural frequency of the system should be 20% higher than the highest operational speed (i.e. greater than 24 000 rpm, 400 Hz).
- The RMS acceleration value in the range 0 - 2 kHz measured on the bearing housing at 20 000 rpm should be less 0.04 m/s².
- The bearing lifetime should be no less than five years (maintenance free) and as long as practically possible.
- The minimum power output of the rotor drive should be 500 W at 25 000 rpm.
- The radial load capacity of the bearing should be at least 20 N.
- The bearing should operate off a 5 bar workshop air supply.
- The turbine, if used, should be small enough in size and weight not to dominate the rotor's dynamic characteristics.
- The coupling of the rotor to the drive should be of such a design that no ill-effect is suffered in the case of the blade catching in the stone.
- The entire saw should fit in the space occupied by the existing spindle and able to be retro-fitted in place of it.
- The total air consumption of the saw should be less than 200 l/min.

Concerning the drive, a simple radial air-turbine was investigated utilizing the same air source as the bearing. In addition a high speed brushless DC motor was also considered. Values of the cutting force during sawing were not available making it difficult to accurately predict the power requirement for successful sawing at 20 000 rpm. The power requirement of 500 W has been calculated from the fact that 120 W machines are conventionally being used to saw stones at 7000 rpm. However, the design and selection of the drive mechanism is beyond the scope of this report.

3.3. Bearing concepts – reasons for the use of an aerostatic bearing

The bearing concepts considered for the new sawing machine were sliding bearings, rolling contact bearings (ball or roller), magnetic bearings, liquid lubricated bearings and gas lubricated bearings. The first of these bearing types were eliminated as possibilities for various reasons, leaving the gas lubricated bearing as the most capable concept for the application.

As mentioned in the literature survey (Chapter 2), conical sliding bearings were investigated and eliminated on the following grounds:

- Friction and subsequent heat build-up limited high speed operation.
- Vibration levels were too high.
- A lack of suitable bearing materials.

Rolling contact bearings would have been limited in the speed requirement of the new saw. Special roller bearings rated at 25 000 rpm are available, but require cooling and would have a limited lifespan. A gas lubricated bearing would be able to run at the desired operating speed without any cooling system required, and the vibration transmitted would be lower than with roller contact bearings. In addition the gas bearing would have lower friction, allowing for a less powerful drive and a longer bearing life. Roller contact bearings would also make axle removal (in the case of blade changing) impossible if the original design layout was retained.

Magnetic bearings would have been another promising bearing type to consider in terms of vibration and friction, but were eliminated due to the complexity of the control system required and the added risk on ensuring a constant power source.

Similarly, liquid bearings could have been successfully implemented but would have required a cooling system, a pumping system and a storage volume, none of which is required for an aerostatic type. The larger load capacity of the liquid bearing would not be required in the diamond saw application, and the friction would be larger than that of a gas bearing.

Of the gas lubricated bearing types, an aerostatic bearing was considered superior to an aerodynamic type in terms of load capacity, stability, ease of manufacture and

surface wear. It was therefore chosen as the bearing type to be used in the new diamond saw, and would provide the following advantages:

- Low levels of friction allowing for low vibration and high speeds without cooling. Low vibration transmission and moderate damping properties of the air film would allow for a lighter rotor housing and base.
- Only an additional small compressor would be required; no cooling systems or gas storage volume tanks would be necessary.
- The load capacity of a medium sized aerostatic bearing would be sufficient in the low-load application of the diamond saw.

3.4. General bearing description

The bearing development occurred over a 10 month period, during which four prototypes were manufactured, all sharing the same general design. The last two prototypes were used for testing and are termed Design A and Design B. A single journal runs in a static bearing bush with the drive mechanism and blade attachments being in an overhung arrangement at either end (Figure 3.2a). This eliminated the difficulties arising from aligning two separate bearing surfaces to the required precision (Figure 3.2b) or the complexity of designing a rotor to be assembled inside a twin-bore bearing (Figure 3.2c).

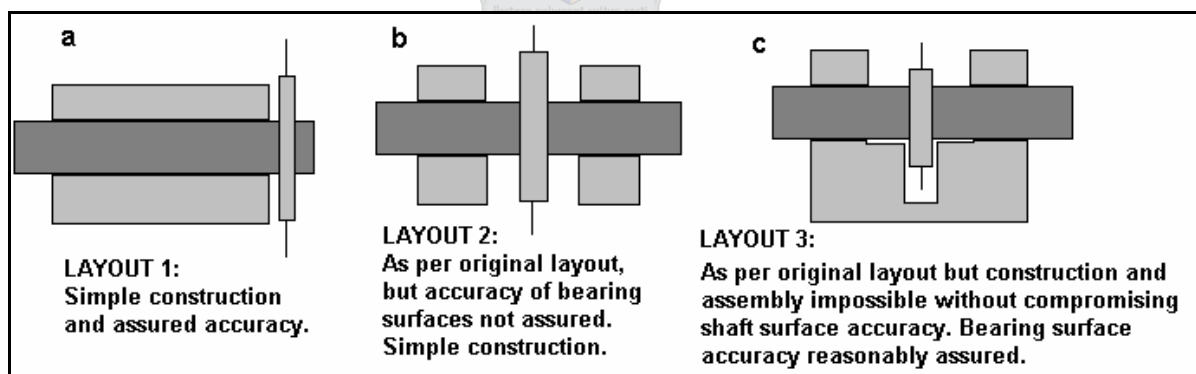


Figure 3.2: The three possible design layouts for the new bearing.

The journal is of the plain type, i.e. a cylinder of circular cross-section with no grooves of any kind, for the sake of simplicity during manufacture. Rows of eight feed jets in the bearing bush feed air to the clearance between the journal and the bush. Air exhausting from the journal feeds the two thrust bearings at each end (Figure 3.3). This design minimises air consumption (as apposed to separate jet fed

thrust faces) and can only be considered in cases where the thrust loads are small. In this type of design the two thrust faces are preloaded against each other when pressurised, resulting in a bearing twice as stiff as a single isolated thrust bearing under the same load (which is important, as the axial vibration frequency would be higher) although the load carrying capacity is reduced by almost 50%, which is not important in this low load application. (Powell, 1970; New Way Precision, 2005).

The pressurised air chamber feeding the jets is made up of the bearing bush which is inserted into a housing sealed by o-rings. As well as being a simple design, it ensures all the jets are under the same supply pressure, eliminating any pressure variation along the journal.

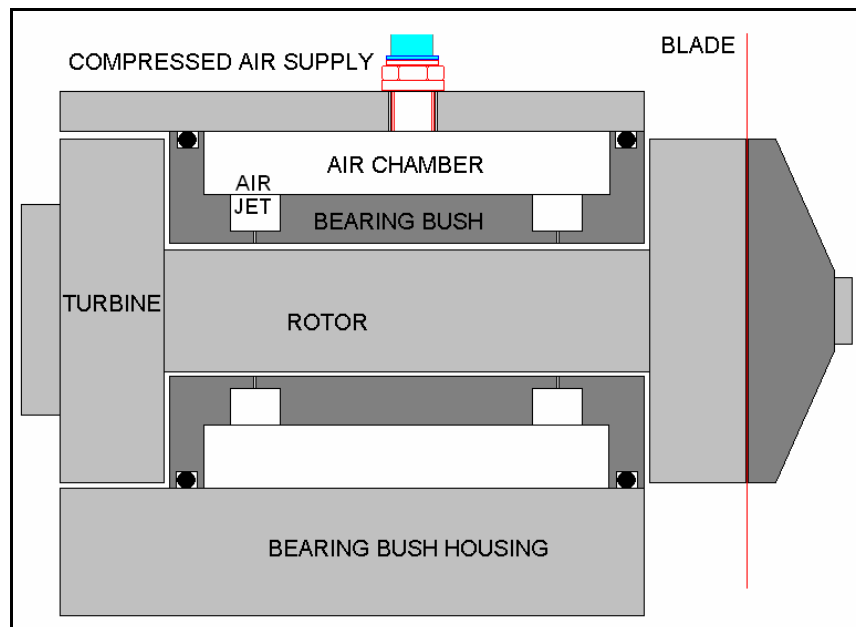


Figure 3.3: The generic form of the designed aerostatic bearing.

3.5. Bearing component design

3.5.1. The journal shaft

A shaft diameter and length of 22 mm and 36 mm respectively was used in the initial designs, but was increased to 25 mm and 45 mm respectively for the fourth prototype in order to increase the angular stiffness. The specified diametrical clearance of the initial prototypes was 25 μm ; the fourth prototype was allowed a

diametrical clearance of 36 μm to ease manufacture. These clearances are considered medium to large by aerostatic bearing standards.

It is generally recommended that the tolerance on the shaft diameter be no more than one-third of that of the mean radial clearance (MRC). As the MRC was 12.5 μm (18 μm for the fourth prototype), the shaft diameter was limited to a 5 μm tolerance along its length (6 μm for the fourth prototype). This tolerance is not small by aerostatic component standards, but was considered very tight by the machinists. The MRC was thus a compromise between the reliable accuracy of the machinists and the air consumption of the bearing, which is normally required to be an absolute minimum, bearing in mind that the air consumption increased with the cubed power of the MRC. This applies to the bearing bush machining as well.

Shaft material was initially hard-anodised aluminium (chosen to reduce rotor mass), which was inadequate in the event of rotor contact. The shafts have to be ground to size, which is only possible on an aluminium component if it is hard-anodised. It would mark easily and anodised particles would come free, blocking the clearance and making it necessary to disassemble and clean the bearing.

Taking into account the fact that a high polar moment of inertia for the rotor was as an important criteria as low mass, a high-carbon, high-chromium tool steel (*Bohler* K110) was specified for the fourth prototype. This provided the necessary surface finish after grinding and could also be finished to the required tolerance more reliably than the anodized aluminium. The increased eccentric position of the heavier rotor would theoretically result in greater stability due to higher damping (which increases with the eccentricity ratio). Also, small imbalance inducing events (blade damage *etc*) would have less of an effect on the overall balance of the rotor if it were heavier. However the steel also tended to mark in the event of rotor contact, though not as badly as with the hard-anodised aluminium.

Regarding material choice and the rotor's natural frequencies, a compromise has to be made against the mass and polar moment of inertia of the rotor. The highest inertia possible is desired while still ensuring that the lowest natural mode is higher than 400 Hz. As stainless-steel was used for the bearing bush, it was never considered as a shaft material in view of its tendency to seize when run together.

Shaft surface material selection was never considered more important than eliminating the risk of rotor contact itself (which should not occur until the most arduous conditions are reached). However, material selection is important from the point of view that should contact occur (due to a broken blade, inferior balancing or insufficient bearing pressure) it should be a minor event limited to investigation into the cause and not requiring extensive repairs.

3.5.2. The bearing bush

The journal shaft rotates within the bearing bush which houses the air feed jets. Both aluminium and stainless steel were used as materials, with the stainless steel being preferable for the following reasons:

- The aluminium bush could only be turned to size (anodising was not an option in the bore) whereas the stainless-steel could be ground and/or honed to size. This improved the ability to ensure the correct shaft tolerance.
- The surface finish obtained on the stainless bush was slightly better than with the aluminium.
- The stainless-steel was more wear resistant than the aluminium.
- With the use of simple jets (discussed in Section 3.5.3), the stainless-steel bush would be less prone to distortion when the jets are inserted – this is very important considering the small clearances involved.

The two flat faces of the bush form part of the axial thrust bearings and are thus finished as per the journal shaft, with special attention given to ensure that they are perpendicular to the bore axis. Each end of the bush makes provision for an o-ring to seal the air cavity that is created when the bush is inserted into the housing.

3.5.3. The feed jets

Two jet positions were investigated – *half-station* and *quarter-station*. This refers to the position of the jet relative to each end of the journal. A half-station bearing has a single row of jets halfway along the journal length. A quarter-station bearing has two rows of jets positioned one-quarter of the journal length from each end; this improves bearing stiffness at the expense of air consumption, which is effectively doubled (Figure 3.4).

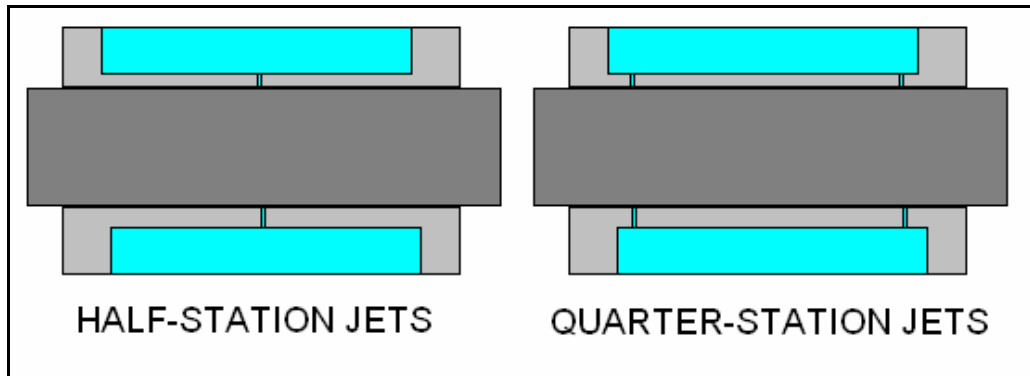


Figure 3.4: Half- versus quarter-station jet positions.

Investigation was also done in the type of jet used, the options being *annular* or *simple* jets. Annular jets result from drilling the feed holes directly through the wall of the bearing bush, while simple jets are designed to incorporate a small air pocket between the ends of the jets and the bore clearance. This is normally accomplished by the use of separate jets fixed in the bearing, sitting slightly below (~ 0.1 mm) the bearing surface. The use of annular jets results in a bearing of lower stiffness than in the case of simple jets. This is because for annular jets the jet area (and thus the gas velocity in the jet) is dependent on the MRC. As the shaft is loaded and the clearance decreases, the jet area decreases. The decrease in jet gas velocity is due to both the decrease in MRC and the decreased area. The pressure loss over the jet is thus lower due to the decreased velocity and the jet throat pressure does not increase as rapidly had the area remained constant. The increase in throat pressure is greater for the simple jet where the area is independent of the MRC (Figure 3.5). Annular jets, by the nature of their design, are larger in diameter (for the same MRC and gauge pressure ratio) than simple jets.

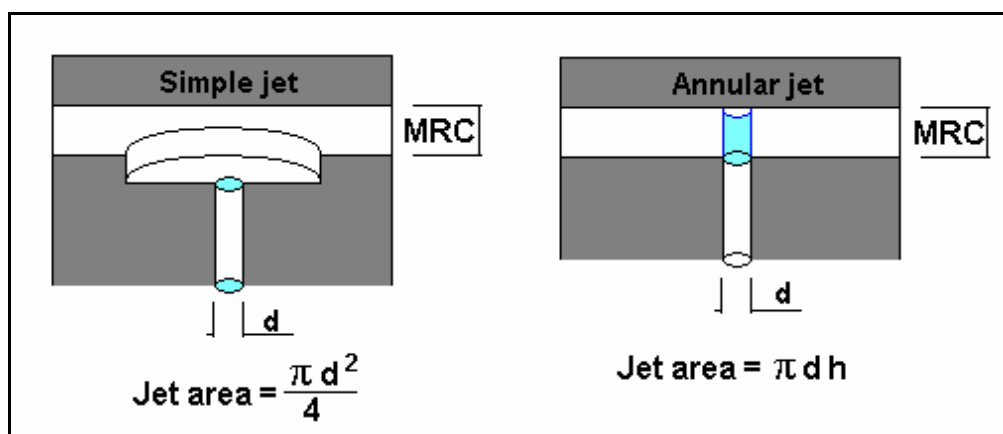


Figure 3.5: The effective flow areas of simple and annular jets.

Each simple jet utilized a brass washer to seal the pocket from the pressurized air chamber used to feed the jets, as shown in Figure 3.6. The jet diameter was limited to 0.2 mm for manufacturing considerations.

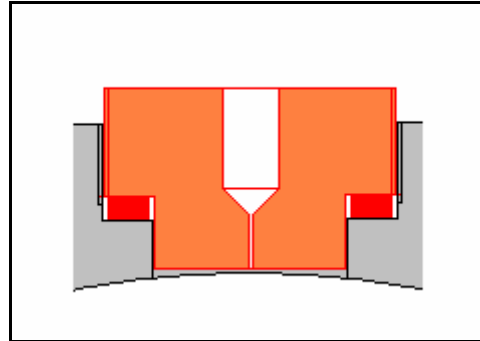


Figure 3.6: A sketch of a simple jet, sealed by a brass washer.

The first jet design investigated were half-station, annular jets used because of their simplicity in manufacture and their economical air consumption. The lack of angular stiffness of the bearing was apparent with this design, and the use of simple jets improved the situation slightly. The greatest improvement in stiffness came with a quarter station design. While simple jets require a more complicated design they have a significant advantage over annular jets in that if they become blocked they can be disassembled and cleared or replaced. A blocked annular jet which is irreparable makes it necessary to replace the bearing bush – an expensive component of the assembly.

3.5.4. The thrust faces

The rotor is supported axially by two thrust bearings. These bearings are formed by two end caps (placed at each end of the journal shaft) and the two faces of the bearing bush. One of the faces can be made integral with the shaft, but the small, inevitable radius present at the bottom of the thrust face tends to cause problems with the sharp edge of the honed bush. If the radius is bigger than the mean axial clearance (MAC), then the pre-loading characteristic of the two thrust bearings will cause the sharp edge of the bush to be forced against the radius of the shaft (Figure 3.7). The shaft is then effectively locked when the bearing is pressurised. This problem can be solved by chamfering the edge of the bore in the bush or by making both thrust faces separate components from the shaft.

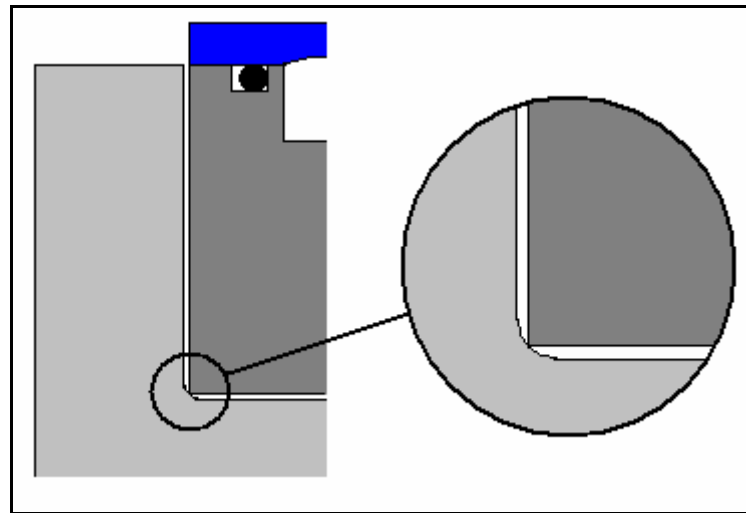


Figure 3.7: The problem encountered with using an integral thrust/journal bearing surface.

If the bush is radiused to solve the problem, additional issues could occur (Figure 3.8). Firstly, any large difference in the radii will result in either a storage volume for the passing air (known to be the cause of rotor instabilities) or the 'rotor locking' situation. Theoretically it is preferable to have a 90° change in flow than a gentle curve, the reason being the form of compensation provided by the restriction at the bend. Perfectly 90° flow paths are created when separate thrust faces are used but it is difficult to ensure that these faces are perpendicular to the journal axis during assembly. This is not a problem if the face is integral with the shaft.

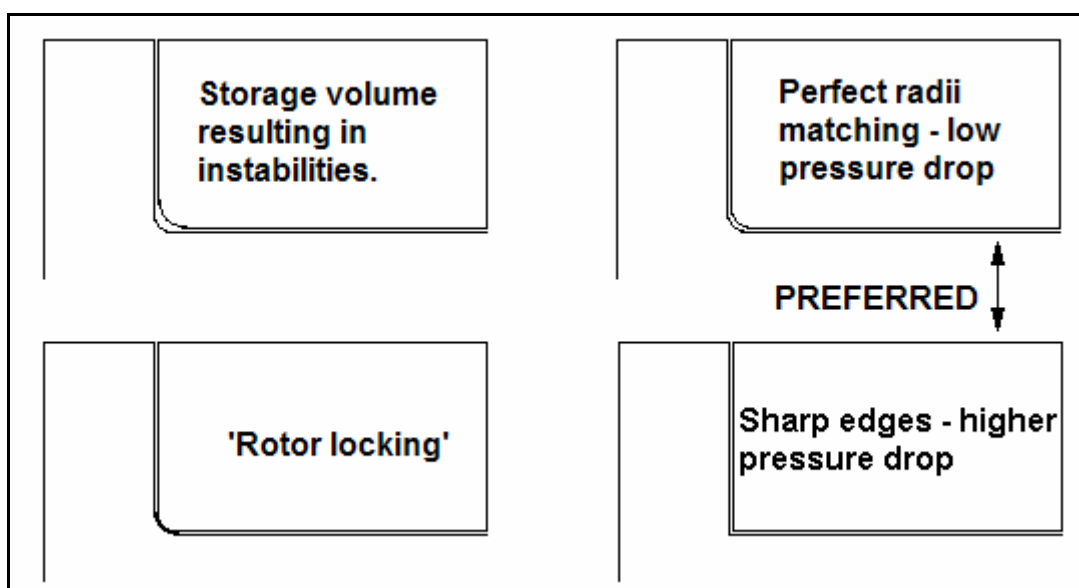


Figure 3.8: The various problems related to radiused bore and shaft edges.

The thrust faces were manufactured from aluminium and hard-anodized to enable them to be ground to tolerance. This would also ensure a long life of the bearing surfaces. In the event of rotor contact the journal would contact the bore before the thrust faces would contact the bush thrust faces. For this reason the wear problems associated with the journal were never encountered with the thrust faces (Figure 3.9).

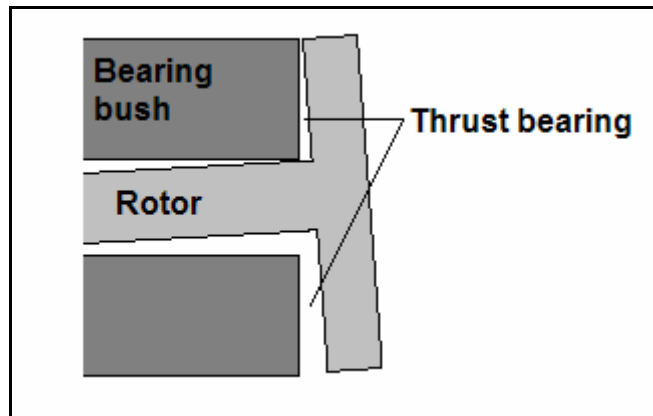


Figure 3.9: An exaggerated sketch showing that rotor contact would never be encountered with the thrust faces.

The MAC for a thrust bearing design of this nature should be made slightly larger than the MRC. If the MAC is allowed to become too small then the pressure drop across the journal length will be reduced which would impair the radial load capacity and stiffness. In practice it was noted that a MAC of up to 35 μm could be tolerated and the main objective in keeping it smaller was to ensure the axial stiffness (and axial vibration frequency) was kept high.

3.5.5. The blade flanges

The blade flanges need to clamp the flimsy sawing blade (thickness of 80 μm) firmly, ensuring it is free from buckles and kept perpendicular to the rotor axis. One of the flanges can double as a thrust face, although this is not possible if the sawing machine is designed to incorporate several flanges of different diameters. The flange/thrust face should be left on the bearing during a blade change to ensure that the thrust face fit on the shaft is not disturbed. The conventional machine can accept all the commercially available flanges, which range from 50 mm to 80 mm in diameter. Figure 3.10 displays the flange design options.

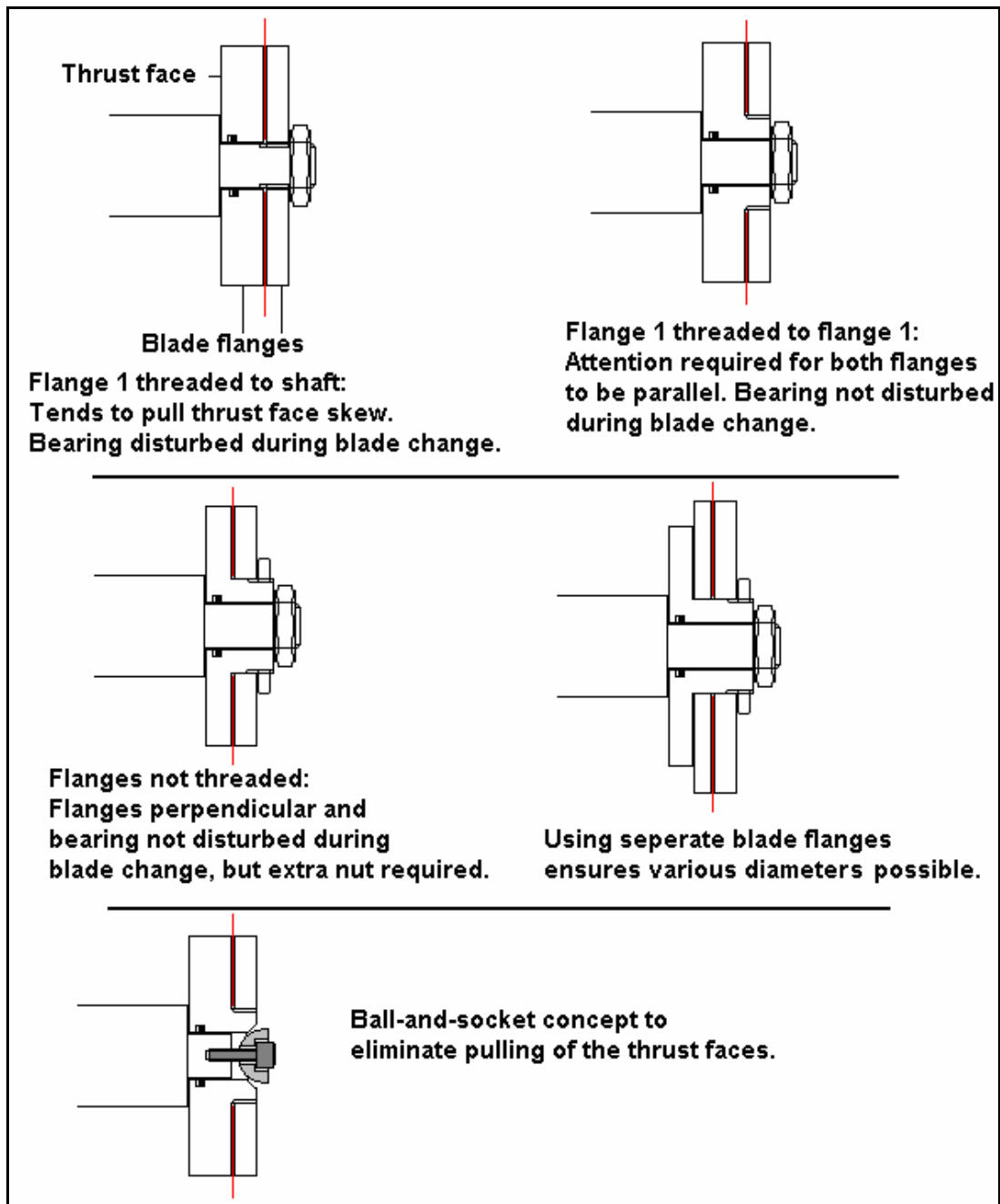


Figure 3.10: Various design options regarding the front thrust face and blade flanges.

The other flange is either held on with a threaded nut, or is threaded itself – which is a much simpler arrangement. However, this flange cannot be threaded to the shaft, as it will tend to pull the other flange, as well as the thrust face, skew. The second flange must thus be threaded to the thrust face, so that there is no mechanical connection between it and the shaft. In addition, the fit of the threaded components must be relatively slack so that the two blade flanges pull fully square against each other. Another solution to this problem would be the use of a ball-and-socket type attachment which would eliminate any pulling of the thrust faces.

3.6. Bearing design strategy

The process of designing the bearing begins with the target load capacity and air consumption from which approximate journal dimensions are obtained. Exact dimensions, clearances and jet diameters are then obtained by available plots and/or equations provided by aerostatic theory. The strategy of designing the bearing is summarised in Figure 3.11 below.

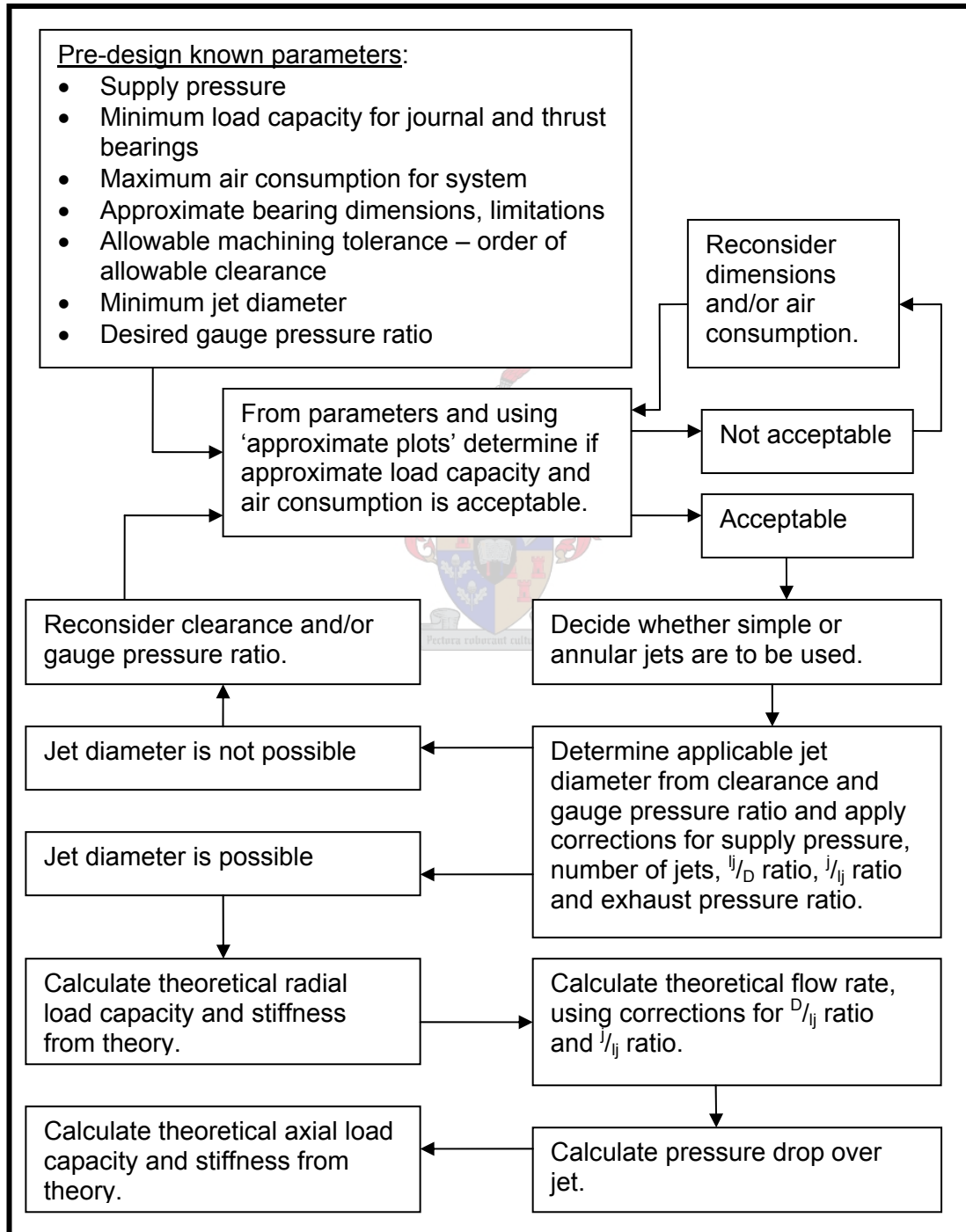


Figure 3.11: The bearing design strategy.

The correction ratios mentioned above for the calculation of the jet diameter are the ratio of the journal length to journal diameter (l_j/D) and the ratio of the jet position to the journal length (j/l_j). The bearing design procedure and equations are provided in Appendix B, with the design software program included in Appendix C. The last two designs will form part of the modal testing in order to calibrate the theoretical rotor models. The specifications for the two investigated designs are given below.

Table 3.1: Bearing design specifications

	Design A	Design B
Journal diameter	22 mm	25 mm
Journal length	36 mm	45 mm
Thrust diameter	55 mm	50 mm
Mean radial clearance	0.0125 mm	0.0180 mm
Mean axial clearance	0.025 mm	0.025 mm
Jet position	Quarter-station	Quarter-station
Jet type	Annular jet	Simple jet
Jet material	N/A	Brass
Jet diameter	0.5 mm	0.2 mm
Jets per row	8	8
Bearing material	304 Stainless-steel	304 Stainless-steel
Rotor material	Hard-anodised aluminium	K110 <i>Bohler</i> high-carbon tool steel, hardened
Drive type	Terry-type turbine	DC brushless motor & Terry-type turbine
Rotor mass	249 g	489 g **
Rotor polar moment of inertia	$90 \times 10^{-6} \text{ kg}\cdot\text{m}^2$	$105 \times 10^{-6} \text{ kg}\cdot\text{m}^2$ **
Rotor transverse moment of inertia	$264 \times 10^{-6} \text{ kg}\cdot\text{m}^2$	$484 \times 10^{-6} \text{ kg}\cdot\text{m}^2$ **
Centre of gravity*	18.8 mm	25.8 mm **

*Measured from the rear thrust face.

**Less the coupling and turbine.

Table 3.2: Theoretical bearing performance specifications*

	Design A	Design B
Radial load capacity	76 N	151 N
Radial stiffness	12 MN/m	16.8 MN/m
Angular stiffness	973 Nm/rad	2123.8 Nm/rad
Axial load capacity	42.5 N	34.3 N
Axial stiffness	4.9 MN/m	3.9 MN/m
Air consumption	11.2 l/min	29.6 l/min

*At a supply pressure of 6 bar and a journal exhaust pressure of 0.6 bar.

The angular stiffness of the bearing is related to the radial stiffness and the journal length by the following equation:

$$K_{ang} = \frac{K_{rad} l_j^2}{H} \quad (\text{Nm/rad}) \quad (3.1)$$

where H is a constant, usually taken as 16 for a quarter station bearing but dependent on the pressure ratio across the journal length (Powel, 1970). For half-station bearings the constant would be greater than 16 as the angular stiffness is less. This constant is dealt with in more detail in Chapter 4 which discusses the rotor modelling.

It became apparent that the angular stiffness of the bearing was more critical than the radial stiffness from a reliability point of view. If a rotor, balanced to within 2 gm·mm, is operated at 20 000 rpm, the maximum radial force due to imbalance would be 8.8 N – well within the limits of the designs discussed above. However, if this imbalance is present at the saw blade position, approximately 45 mm from the centre of gravity, the torque on the rotor due to imbalance would be 0.4 N·m which, with an angular stiffness of 500 N·m/rad, would allow a rotor whirl angle of 0.0008 rad (0.045°). This translates to 36 µm at the edge of a 45 mm long rotor, which is enough to allow rotor contact, even though the radial load capacity might be ten times higher than the imbalance force.

Cross sectional views of the two designs are provided below:

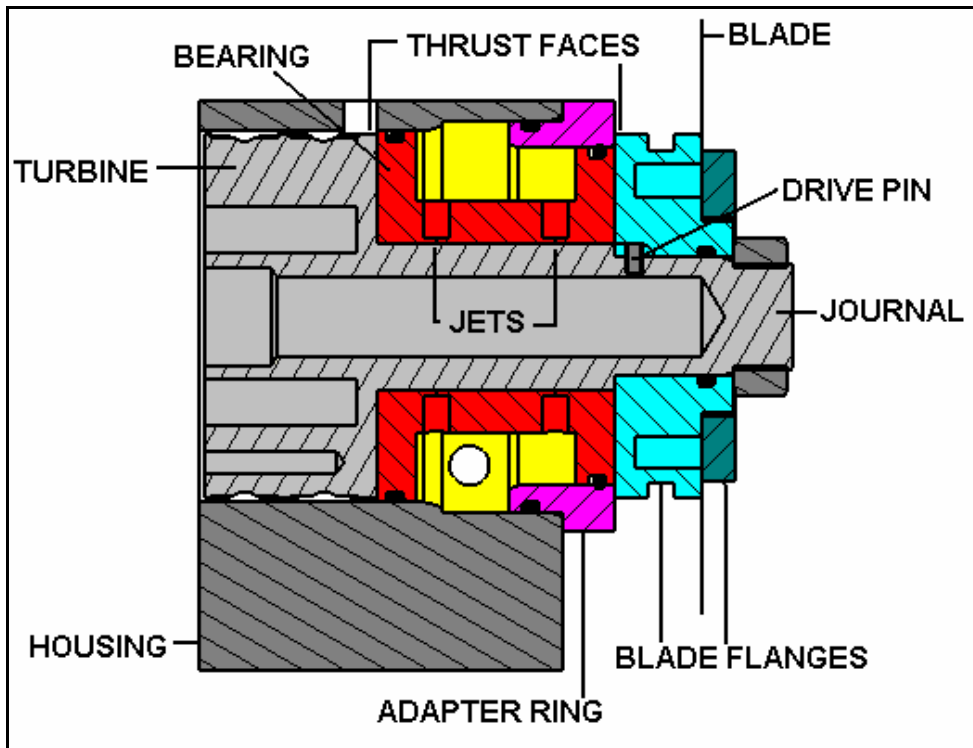


Figure 3.12: Design A in cross-section.

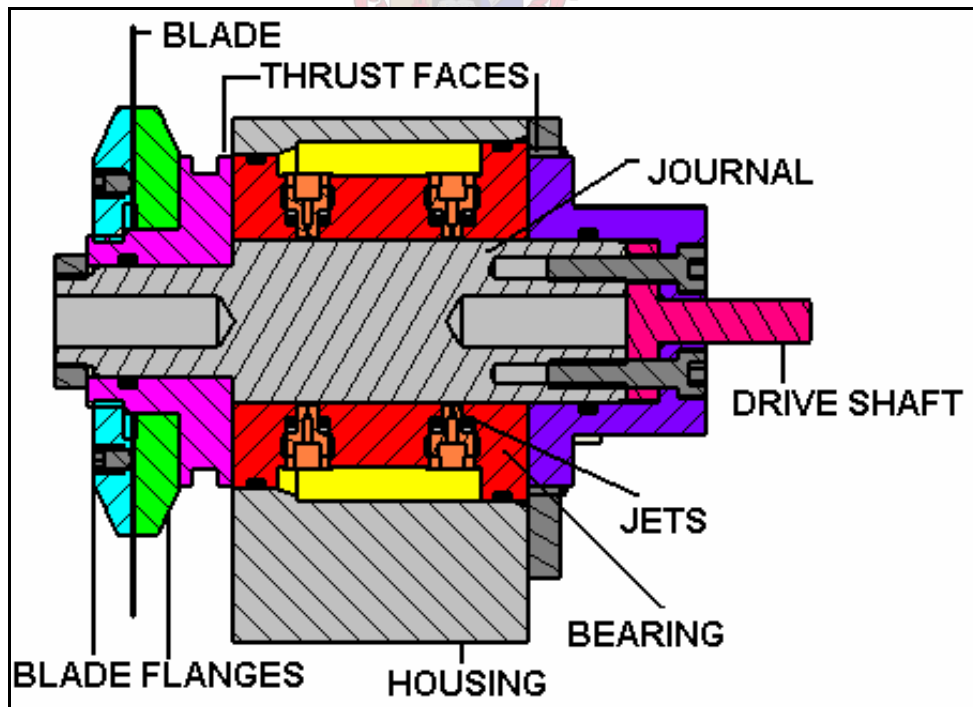


Figure 3.13: Design B in cross-section. Note the separate thrust faces, separate blade flanges and the simple jets.

Chapter 4: Modelling of the Aerostatic Bearing and Rotor

This chapter details the purpose and execution of the models used to evaluate the dynamic behaviour of the rotor both as a rigid and flexible entity. The ultimate goal of this modelling was to enable the design of a rotor that is stable (in terms of resonant frequencies and motion amplitudes) at all speeds up to its maximum operating speed. In this way, maximum bearing life and reliability of the final product would be assured.

4.1. The flexible body analysis of the rotor (Design A)

Considering a rotor as rigid (and thus not considering bending or torsional vibration modes) is valid if the frequency of operation (the sawing speed) is less than half the frequency of the lowest flexible body mode (Harker, 1983; Hartog, 1956). In this case, for a rigid assumption to be justified, the lowest flexible body mode would thus have to be higher than 660 Hz (~40 000 rpm).

It was expected that the assumption would be valid, as a shaft is only generally considered flexible if its length is greater than ten times its diameter and/or a concentrated mass is positioned away from its supports – conditions which are not applicable in this case. However, the validity of the assumption is examined in this section by considering bending, torsion and axial vibration of the rotor using a finite element method (FEM) analysis.

The rotor was analysed as both a flexible rotor in space (i.e. no constraints applied) as well as a flexible rotor surrounded by a medium (representing the air film) which was constrained at its free surfaces. It was expected that the stiffness of the air film would be negligible compared with the stiffness of the rotor and that the frequencies of the modes would be very similar (although slightly higher) when the air film is incorporated into the model. The FEM analyses were done only for Design A which has a hollow aluminium rotor. This is because it is more flexible and the respective modes would occur at a lower frequency than Design B (which uses a solid steel rotor). The analyses were done in MSC Nastran using 3D solids with approximately 50 000 Hexagon elements.

4.1.1. FEM analysis of an isolated rotor – no air film

This model was constructed by revolving the rotors' general cross-section - the models were therefore axisymmetric and did not consider any asymmetrical features of the rotor, such as the spanner flats and the turbine pockets. Also, the blade flanges and nut are modelled as being integral with the rotor, i.e. only one solid is present, and the steel nut was given the same material properties as the aluminium rotor.

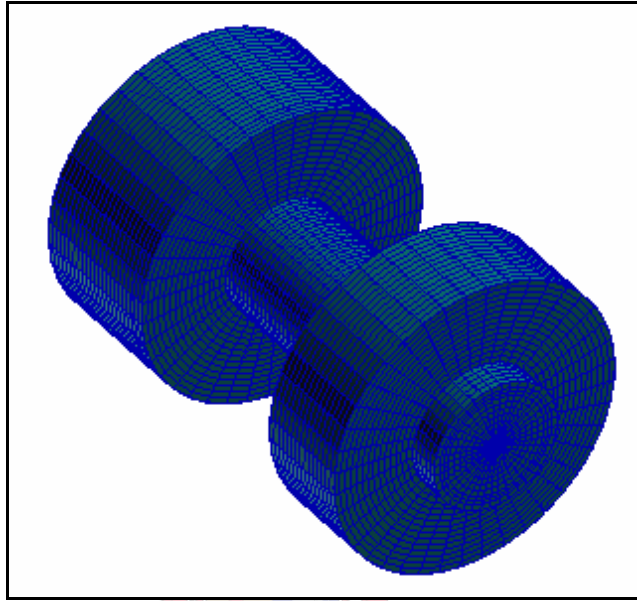


Figure 4.1: The non-constrained FEM model.

The objective of this model was to compare the frequencies of the flexible body vibration modes to those of the rigid body modes calculated by the Euler model (discussed in Section 4.2). A high degree of accuracy was not important with this model as a general comparison was all that was required. The frequencies of the first six rigid modes were all zero in accordance with the six free degrees of freedom (x , y , z , ψ , θ and ϕ , defined in Section 4.2). The mode with the lowest frequency was the torsion of the rotor along the x -axis at 3525 Hz. The next mode was the first bending mode at 3599 Hz, followed by the axial vibration mode at 7873 Hz. From these results it was seen that the assumption of the rotor being a rigid body was indeed valid as the lowest vibration modes were considerably larger than 660 Hz.

4.1.2. FEM analysis of a supported rotor – with air film

Additional FEM models were built with an ‘air-film’ incorporated. This consisted of an additional solid with its own unique material properties surrounding the journal.

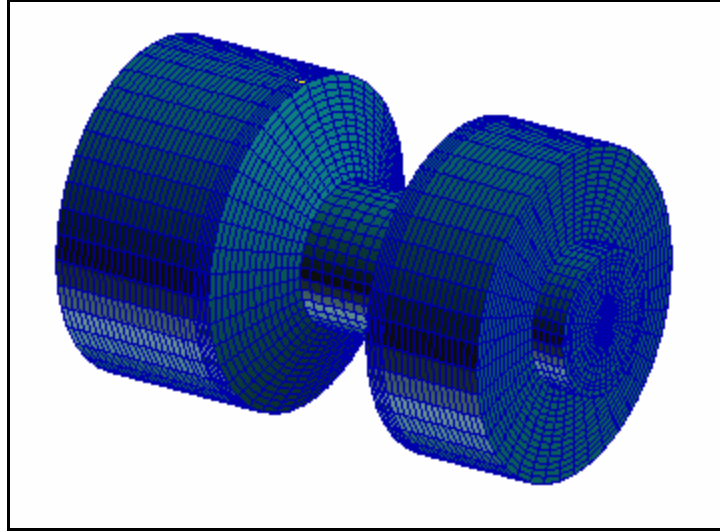


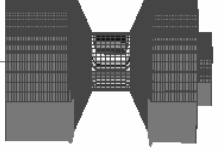
Figure 4.2: The FEM model incorporating an ‘air film’.

The ‘air film’ solid was shaped so that it represented the fall in air pressure along the journal. The properties of this ‘air film’ solid were adjusted until the frequencies of the five rigid body modes (x , y , z , θ and ϕ) approximated that of the Euler model. The FEM analysis calculated an additional axial torsion by considering the shear strength of the air film which is negligible in reality. The purpose of this FEM analysis was to determine whether the air film has any significant effect on the modal frequencies of the free flexible rotor.

The frequencies of the flexible body modes for the constrained model were slightly higher than that obtained with the free model. Although it was not possible to construct the model so that it would mimic the results of the Euler model exactly, it was clear that the effect of the air film was very small.

The results for the frequencies of the rotor’s natural modes obtained from the two FEM models as well as the Euler model are presented in Table 4.1. Although the Euler model has yet to be discussed, displaying the results here enables the FEM results to be put in perspective.

Table 4.1: Frequencies of the natural modes from FEM analysis and the Euler model.

Mode	Mode description	Mode frequency (Hz)		
		Non-constrained	Constrained	Euler
1 and 2 (Rigid body)	Angular vibration around the y and z axes. 	0	373	281 & 338
3 (Rigid body)	Axial vibration along x axis. 	0	704	706
4 and 5 (Rigid body)	Transverse vibration along the y and z axes. 	0	854	1113
6 (Flexible body)	Torsion about the x axis. 	3525	3528	/
7 and 8 (Flexible body)	First bending mode in the xy and xz planes. 	3599	3687	/
9 (Flexible body)	Axial rotor vibration (x axis). 	7873	7902	/
10 and 11 (Flexible body)	Second bending mode in the xy and xz planes. 	7998	8026	/

4.2. The rigid body analysis of the rotor

A rigid body model was used to predict the natural frequencies and simulate the motion of the rotor. This was accomplished by developing a software program that calculates the orientation and position of the rotor as a function of time. The system's frequencies were obtained by expressing the resulting time response in the frequency domain using a Fast Fourier Transform (FFT). In considering the goal of maximum rotor stability, the following items were investigated:

- The natural frequencies of the rigid modes of the two rotor designs.
- The effect of the rotor mass, rotor inertia, bearing stiffness, centre of gravity (CG) position and rotor speed on the natural frequencies of the rigid modes.
- The effect of the residual imbalance, the axial position of the imbalance and the rotor speed on the motion amplitudes.

4.2.1. The pressure distribution within the bearing

Before the modelling itself is dealt with, the pressure distribution within the bearing will be discussed. The pressure losses considered are due to the gas flow through the feed jets and along the journal and the thrust clearances. The pressure is assumed to drop linearly across these flow paths. The pressure distributions within a half-station and a quarter-station bearing are shown in Figure 4.3 below.

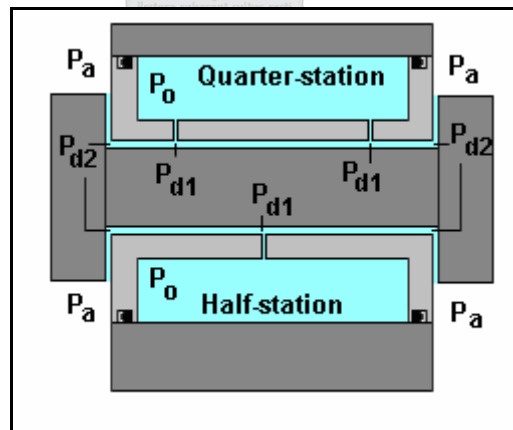


Figure 4.3: Pressure distribution in the aerostatic bearing model.

The pressure of the gas drops from the supply pressure (P_o) to the jet throat pressure (P_{d1}) as it flows through the jets, before dropping to the journal exhaust pressure (P_{d2}). The thrust bearings exhaust to atmospheric pressure (P_a). Of particular importance is the pressure drop along the journal length as this is what the radial and

angular bearing stiffness are dependent on. Shown below (Figure 4.4a) are the theoretical pressure distributions for half- and quarter-station bearing types (New Way Precision Bearings, 2003).

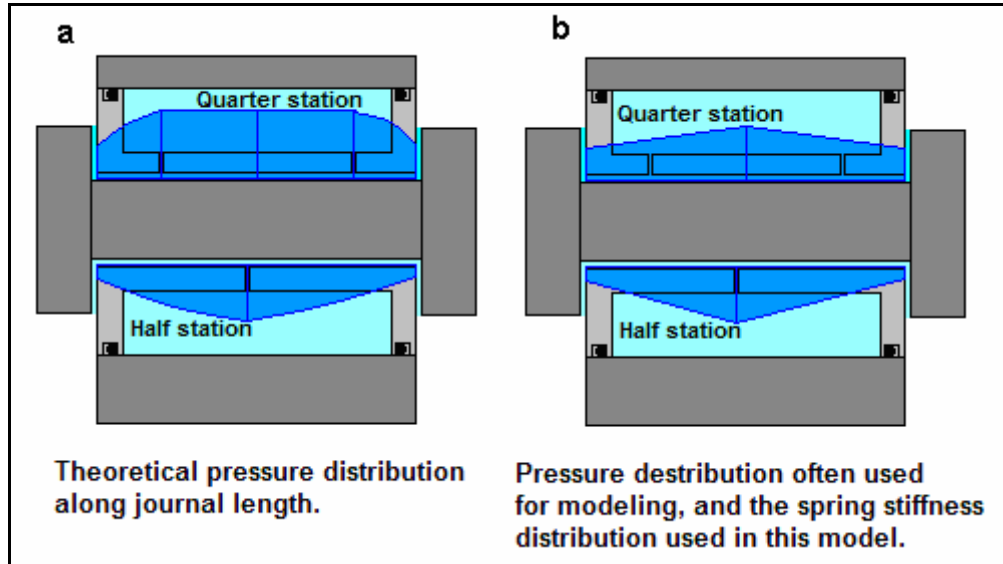


Figure 4.4: Theoretical pressure (left) and equivalent spring stiffness (right) distribution used for modelling purposes.

The rigid body model uses linear coil springs to represent the air stiffness (Figure 4.6), with the stiffness constants decreasing linearly along the journal length to represent the fall in journal pressure. Different gradients for the spring stiffness reductions are used for the quarter- and half-station designs. A spring stiffness ratio Q is used to calculate the angular stiffness from a given radial stiffness. Q is defined as the ratio of the middle spring stiffness to that of the springs at each end. For a half-station bearing Q would be similar to the ratio of the jet throat pressure to the journal exhaust pressure, as the spring stiffness distribution resembles the theoretical pressure distribution. However for the quarter-station design the stiffness distribution does not accurately resemble the pressure distribution and Q is calculated to provide the correct ratio of angular to radial stiffness defined in the theory. For two bearings of equal radial stiffness Q would be lower for the quarter-station bearing due to its larger angular stiffness.

4.2.2. The modified Euler 3-dimensional numerical model

In this model, the rotor is attached to a reference frame xyz which moves in an inertial reference frame XYZ . The rotor is spinning about the x axis (which is aligned with the symmetric axis of the rotor) and its motion is described by the rotation of the reference frame around the y and z axis (θ and \varnothing respectively) as well as the translation of the origin of the reference frame (which coincides with the rotor's CG) within the inertial frame (x , y and z). This definition of the rotor motion is described by the modified Euler equations of motion which takes gyroscopic effects into account (Baruh, 1999). The derivation of the model is presented in Appendix A.

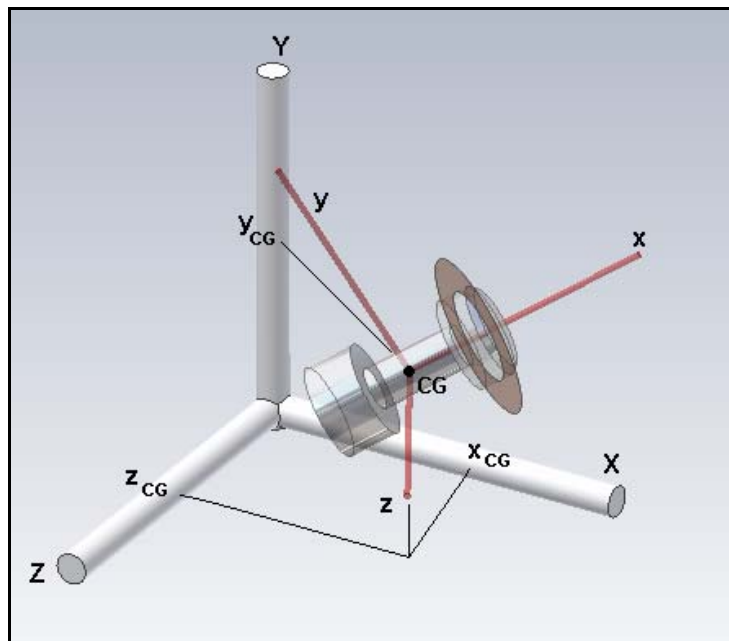


Figure 4.5: The rotor attached to the xyz reference frame and moving within the inertial XYZ frame.

Although six degrees of freedom (DOF) are normally associated with a rigid body moving in a 3-dimensional space, in this case one angular rotational motion is a free body motion – the spinning of the rotor around the x -axis. Thus the model described here has five rigid body DOFs, listed below:

- Translation along the x -axis, x
- Translation along the y -axis, y
- Translation along the z -axis, z
- Rotation about the y -axis, θ
- Rotation about the z -axis, \varnothing

The corresponding equations of motion are (as derived in Appendix A):

$$\begin{aligned} \Sigma F(\underline{i}): & -K_{ax}x - C_{ax}\dot{x} + B[\sin(n\psi t) - \sin(n\psi t + \alpha)]\theta + F_{fric}\theta - F_{cut}\phi - W\phi \\ & - m(\ddot{e}\cos\psi t - \ddot{\phi}e\sin\psi t - 2\dot{\theta}\dot{\psi}e\sin\psi t - 2\dot{\phi}\dot{\psi}e\cos\psi t) = M\dot{v}_x + (M - m)(\dot{\phi}v_y + \dot{\theta}v_z) \end{aligned} \quad (4.1)$$

$$\begin{aligned} \Sigma F(\underline{j}): & -K_{rad}y - \phi\Gamma - C_{rad}\dot{y} - C_{damp}\dot{\phi}\Sigma - B[\sin(n\psi t) - \sin(n\psi t + \alpha)]\theta\phi \\ & - F_{fric}\theta\phi - F_{cut} - W - m(\ddot{\phi}a - e\dot{\psi}^2\sin\psi t) = M\dot{v}_y + (M - m)(\dot{\phi}v_x - \dot{\theta}v_z) \end{aligned} \quad (4.2)$$

$$\begin{aligned} \Sigma F(\underline{k}): & -K_{rad}z + \theta\Gamma - C_{rad}\dot{z} + C_{damp}(\dot{\theta} - \dot{\phi}\theta\phi)\Sigma - B[\sin(n\psi t) - \sin(n\psi t + \alpha)] \\ & - F_{fric} - m(\ddot{\theta}a - e\dot{\psi}^2\cos\psi t) = M\dot{v}_z + (M - m)(-\dot{\theta}v_x + \dot{\theta}\phi v_y) \end{aligned} \quad (4.3)$$

$$\begin{aligned} \Sigma M(\underline{i}): & r_t[B(\sin(n\omega t) + \sin(n\omega t + \alpha))] + m(\dot{v}_y + \ddot{\phi}a - e\dot{\psi}^2\sin\psi t)e\cos\psi t \\ & - m(\dot{v}_z + \ddot{\theta}a - e\dot{\psi}^2\cos\psi t)e\sin\psi t = I_{xx}(\ddot{\psi} + \ddot{\theta}\phi + \dot{\theta}\dot{\phi}) \end{aligned} \quad (4.4)$$

$$\begin{aligned} \Sigma M(\underline{j}): & z\Gamma - \theta K_{ang} + \dot{z}C_{damp}\Sigma - (\dot{\theta} - \dot{\phi}\theta\phi)C_{damp}\Sigma\Sigma + cB[\sin(n\omega t + \alpha) - \sin(n\omega t)] \\ & + h\mu F_{cut} + am(\dot{v}_z - e\dot{\psi}^2\cos\psi t) - m(\dot{v}_x - \ddot{\phi}e\sin\psi t - 2\dot{\theta}\dot{\psi}e\sin\psi t - 2\dot{\phi}\dot{\psi}e\cos\psi t)e\cos\psi t \\ & = (I_{yy} - a^2m + e^2m\cos^2\psi t)\ddot{\theta} - I_{yy}(\dot{\theta}\dot{\phi}\phi) + I_{xx}(\dot{\phi}\dot{\theta}\phi + \dot{\phi}\dot{\psi}) - I_{zz}(\dot{\phi}\dot{\theta}\phi) \end{aligned} \quad (4.5)$$

$$\begin{aligned} \Sigma M(\underline{k}): & -y\Gamma - \phi K_{ang} - \dot{y}C_{damp}\Sigma - \dot{\phi}C_{damp}\Sigma\Sigma + cB[\sin(n\psi t) - \sin(n\psi t + \alpha)]\theta\phi \\ & + r_t[2E + B(\sin(n\psi t) + \sin(n\psi t + \alpha))]\theta + r_b F_{cut}\phi - hF_{cut} - h\mu F_{cut}\theta\phi \\ & - r_b\mu F_{cut}\theta + m(\dot{v}_x + \ddot{\theta}e\cos\psi t - 2\dot{\theta}\dot{\psi}e\sin\psi t - 2\dot{\phi}\dot{\psi}e\cos\psi t)e\sin\psi t \\ & - am(\dot{v}_y - e\dot{\psi}^2\sin\psi t) = \ddot{\phi}(I_{zz} + e^2m\sin^2\psi t + a^2m) + I_{yy}(\dot{\theta}^2\phi) - I_{xx}(\dot{\theta}^2\phi + \dot{\theta}\dot{\psi}) \end{aligned} \quad (4.6)$$

The rotor is modelled as a geometrically-uniform shaft with a non-symmetric CG. A mass imbalance is incorporated into the model at an axial distance a from the CG and a radial distance e from the journal axis. The springs and viscous dampers representing the air film support the journal axially as well as radially. The stiffness and damping coefficients are independent of the rotor displacement and velocity respectively, i.e. they exhibit linear behaviour.

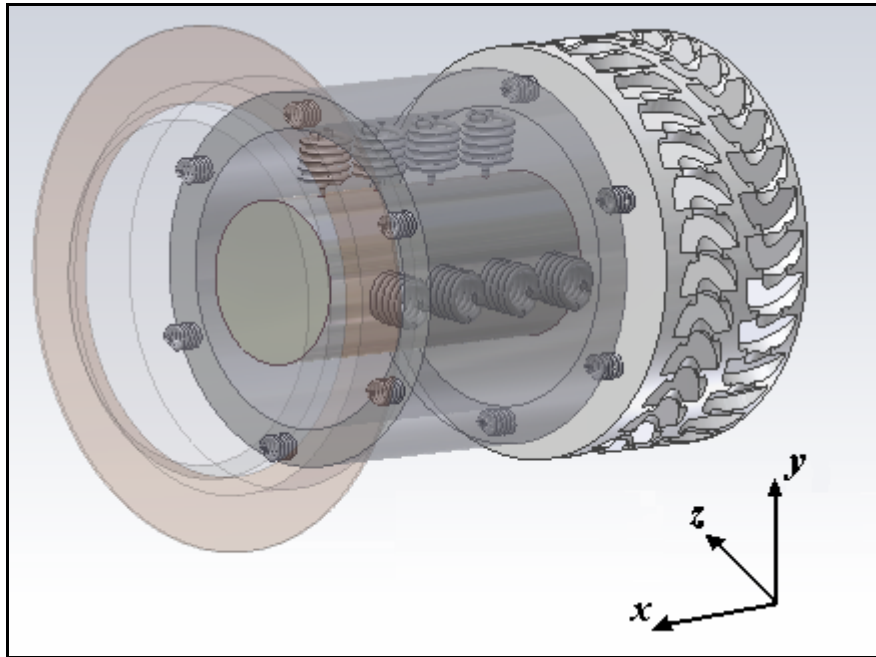


Figure 4.6: Linear coil springs used to represent the air stiffness.

The solution of the Euler equations was done using a Matlab Simulink model (shown in Appendix C). The Runge-Kutta method was used for the solution. The sequence of the rigid body solution is shown below.

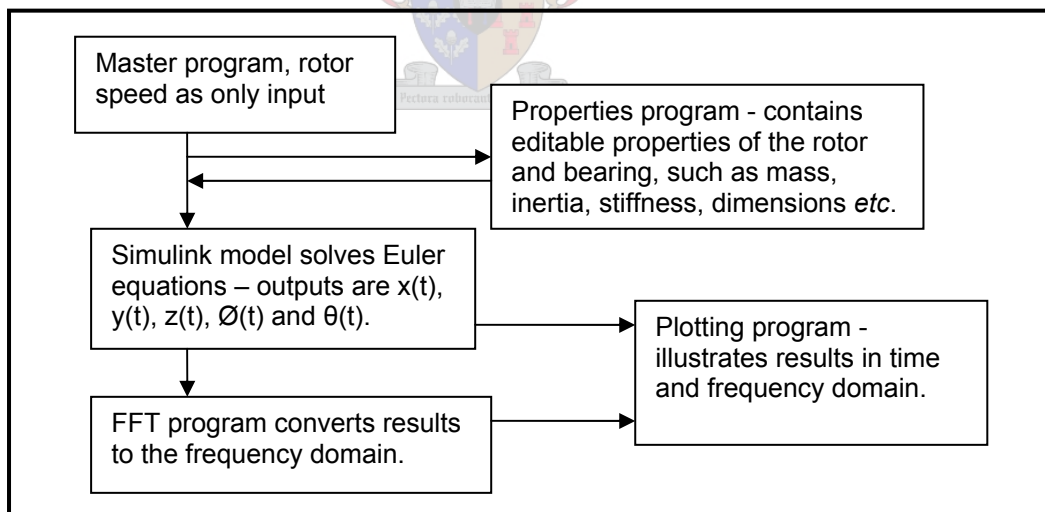


Figure 4.7: Solution path of the Euler simulation of the rigid rotor.

Once the time responses for the five DOFs are obtained, an FFT is used to express the results in the frequency domain, and thus illustrate the dominant frequencies of the system. These results will now be discussed.

4.2.3. Natural mode frequencies for the two rotor designs

The system frequencies calculated for the two rotor designs are discussed below. No damping is assumed and the bearing properties are as stated in Chapter 3 (i.e. the supply pressure is 6 bar with a journal exhaust pressure of 0.6 bar). For brevity, only the response of the y and x co-ordinates are shown, as all the system frequencies can be obtained from these two plots. The rotor speed is 10 000 rpm.

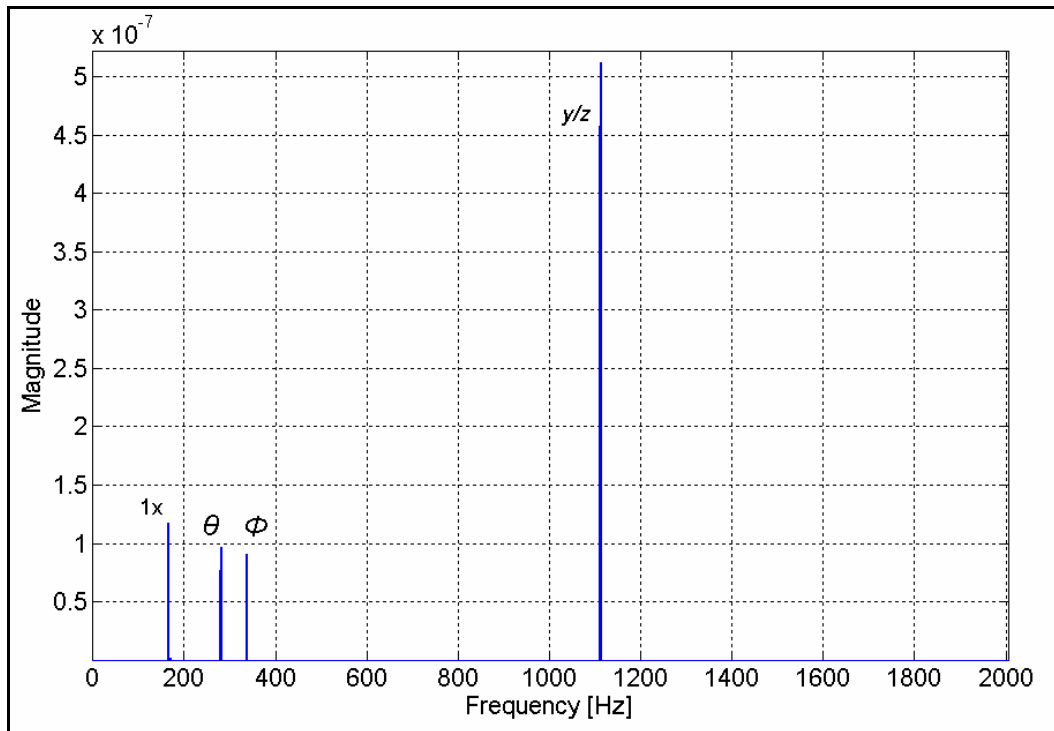


Figure 4.8: The FFT of the y response for Design A (10 000 rpm).

The frequencies of both the y and z translation modes occur at 1112.7 Hz being equal due to the rotor symmetry. The angular (tilt or transverse) modes for θ and ϕ are 281 Hz and 338 Hz respectively. The frequencies of the two angular modes are dependent on the rotor speed due to gyroscopic effects. They bifurcate after 0 rpm with ω_{ϕ} increasing and ω_{θ} decreasing as the rotor speed increases. This phenomenon is discussed further in Section 4.2.4. The 1x peak (167 Hz) due to the imbalance is also present.

The axial system mode cannot be seen in the y-response FFT (it is present but very small in magnitude) and is shown in the FFT of the x-response below (Figure 4.9). The highest peak at 706 Hz is the axial vibration mode. The y/z translation mode can also be seen, as can the two angular modes, θ and ϕ , and the imbalance.

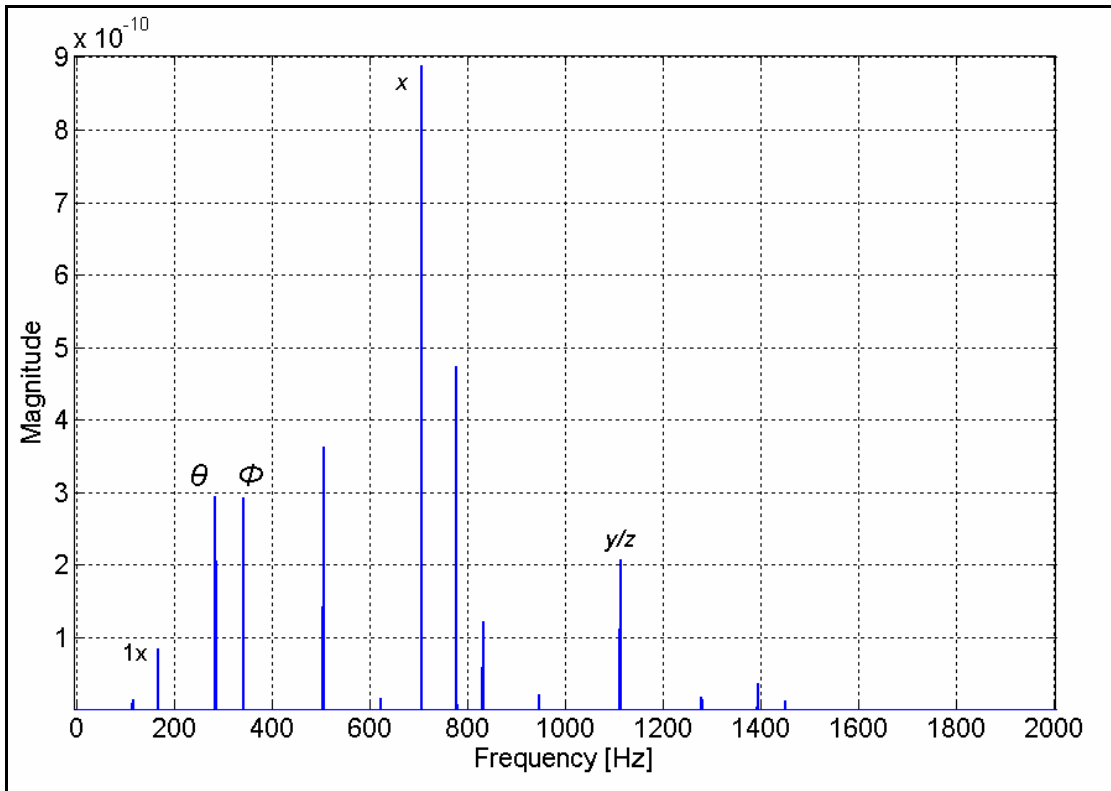


Figure 4.9: The FFT of the x response for Design A (10 000 rpm).

In addition to these are 10 peaks which are positioned on either side of the five rigid modes. This is a consequence of the imbalance term in Equation 4.1 and their positions are dependent on the frequencies of the rotor rotation and the \emptyset mode.

The FFT of the y response for Design B is shown in Figure 4.10. The frequency of the y and z translation modes has decreased to 938.5 Hz. Although the rotor mass has increased, a near-identical increase in the load capacity had negated this – the reduction in the frequency is in fact due mainly to the increase in the journal clearance. The angular modes have increased slightly to 315 Hz and 350.5 Hz due to the increase in angular bearing stiffness, mainly due to the increase in journal length. The axial mode (Figure 4.11) has been reduced to 449.5 Hz due to the increased rotor mass and reduced thrust face area. Again the additional peaks are present.

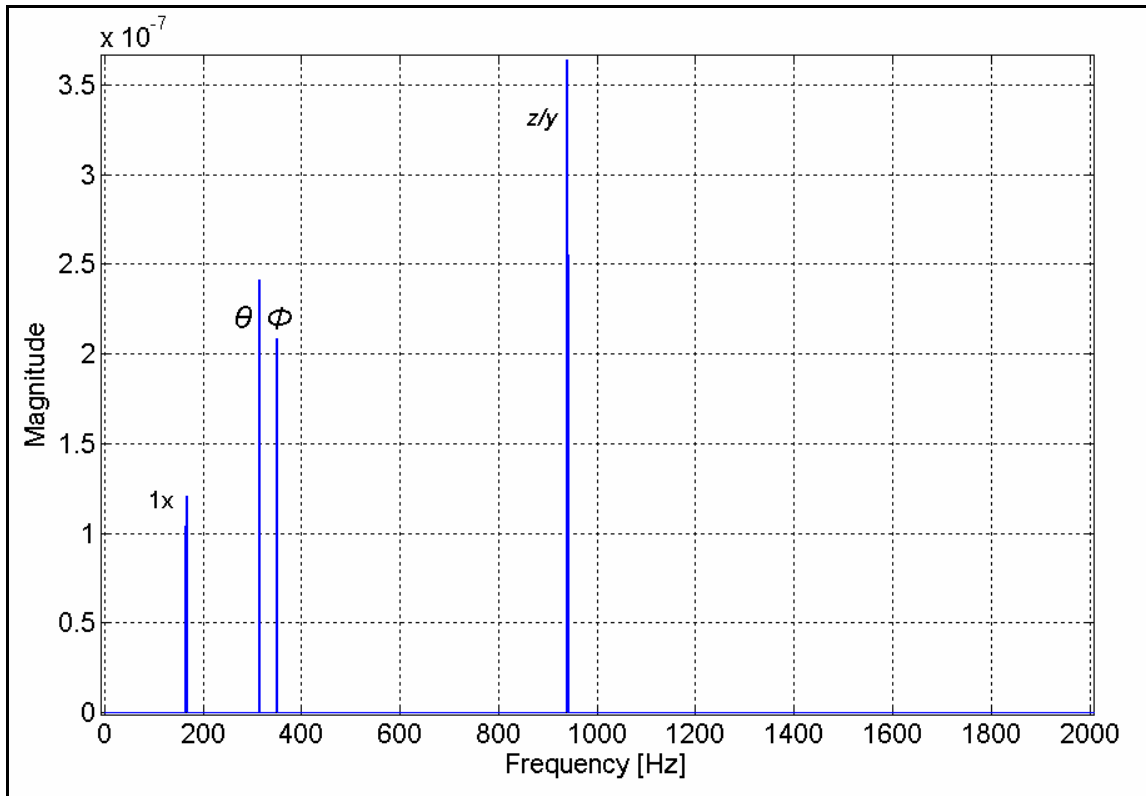


Figure 4.10: The FFT of the y response for Design B (10 000 rpm).

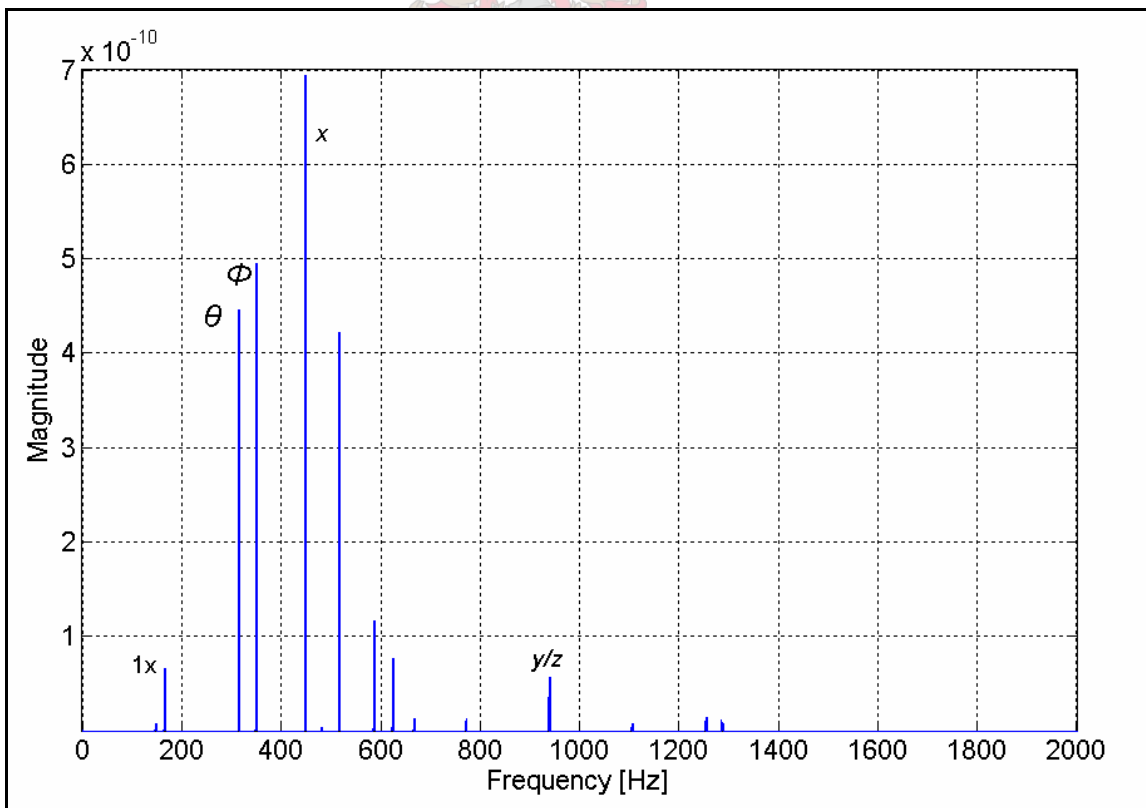


Figure 4.11: The FFT of the x response for Design B (10 000 rpm).

4.2.4. The effect of rotor speed on the system frequencies

The rotor speed has an effect on the angular modes (θ and ϕ) only. This is due to gyroscopic effects - the trend is shown in a Campbell diagram below.

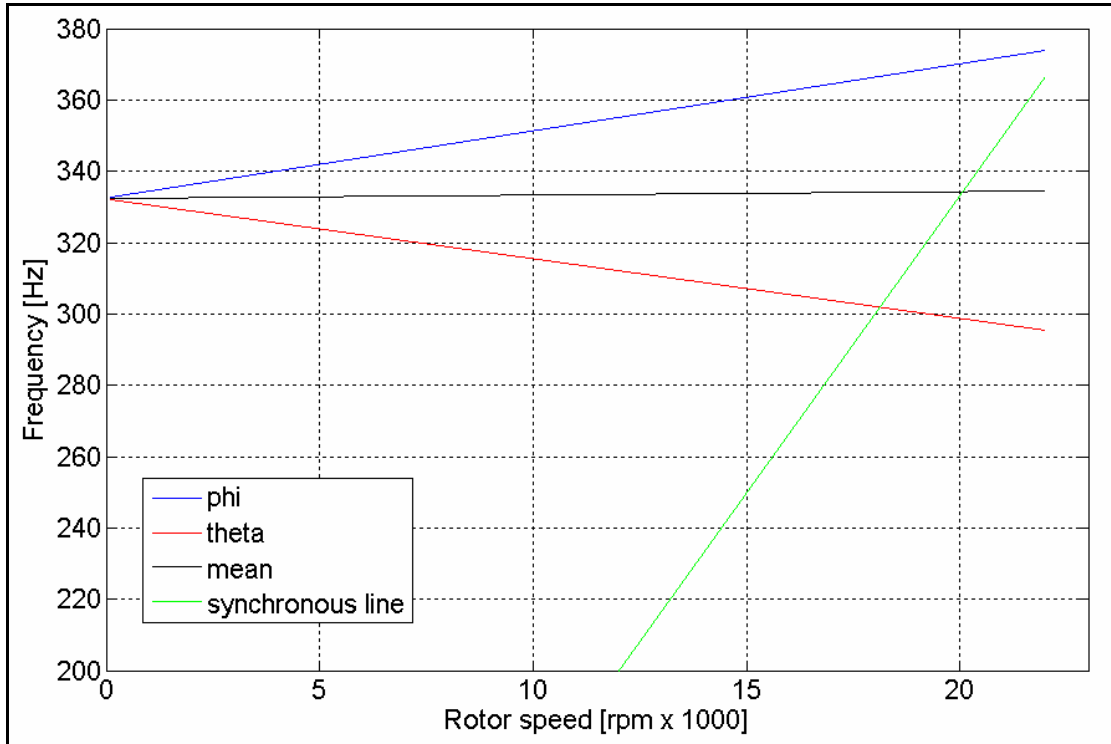


Figure 4.12: The variation in the frequency of the angular modes with rotor speed (Design B, no damping).

The variation of the frequency with rotor speed is linear and the reason for the occurrence is due to the gyroscopic terms in the rotational equations of motion (Equations 4.4 to 4.6) which includes the $\dot{\psi}$ term. This is not the case for any of the translational equations of motion. This phenomenon is analogous to the forward and backwards whirling of flexible shafts, a well-documented phenomenon which occurs in many high-speed shafts and flywheels. In this case it applies to the frequency of whirling of the rigid rotor as seen from the y and z directions respectively. The problem lies in the fact that the frequency of the 'backwards' whirling mode (theta) decreases as the rotor speed increases and a resonant condition is thus encountered at a lower rotor speed than expected. The model suggests that the mean of the two angular modes increases slightly with an increase in rotor speed. The product of the frequencies remains constant with rotor speed, similar to the study by Brown *et al.* (2006).

4.2.5. The effect of rotor mass, rotor inertia, bearing stiffness and the position of the centre of gravity on the system frequencies

The effect of rotor mass, rotor inertia and bearing stiffness on the system frequencies is similar to that of single degree of freedom (SDOF) vibration theory (Inman, 2001). The frequency of the axial vibration mode given by the Euler model is exactly as that given by SDOF theory and is independent on the position of the CG. That is, the frequency of the axial mode can be calculated by the equation:

$$\omega_x = \frac{\sqrt{\frac{K_{ax}}{M}}}{2\pi} \quad (\text{Hz}) \quad (4.7)$$

The y and z transverse vibration frequency is slightly higher than that given by SDOF theory, due to the non-symmetric position of the CG. This variation is very small – less than 1% change in frequency for a 15% change in the distance of gravity position from the journal end. If the CG is positioned in the geometric centre of the journal, the Euler model and SDOF theory give the same frequencies and thus can be defined by the equation:

$$\omega_{y,z} = \frac{\sqrt{\frac{K_{rad}}{M}}}{2\pi} \quad (\text{Hz}) \quad (4.8)$$



Considering the fact that the frequencies of the angular modes change with the rotor speed, it is necessary to compare the mean frequency of the two modes with the single frequency calculated from SDOF theory. This mean value also increases slightly with rotor speed, as seen in Figure 4.12. When the CG of the rotor and the geometric centre of the journal coincide, the SDOF theory and Euler model give the same results at 0 rpm – that is, the frequency defined by the following equation:

$$\omega_{\theta,\phi} = \frac{\sqrt{\frac{K_{ang}}{I_{zz}}}}{2\pi} \quad (\text{Hz}) \quad (4.9)$$

4.2.6. The effect of imbalance on rotor motion amplitudes.

The whirl amplitude of the journal end for Design B was predicted as a function of the following parameters: the residual imbalance (g.mm), the axial position of the imbalance (a) and the rotor speed. This was only examined for the journal end as this is the point where rotor contact would initially occur.

4.2.6.1. The effect of residual imbalance (g.mm value) on motion amplitudes

Figure 4.13 below illustrates the whirl amplitude on the rotor end at specific rotor speeds from 6000 rpm to 25 000 rpm for specific values of the residual imbalance. No damping is assumed.

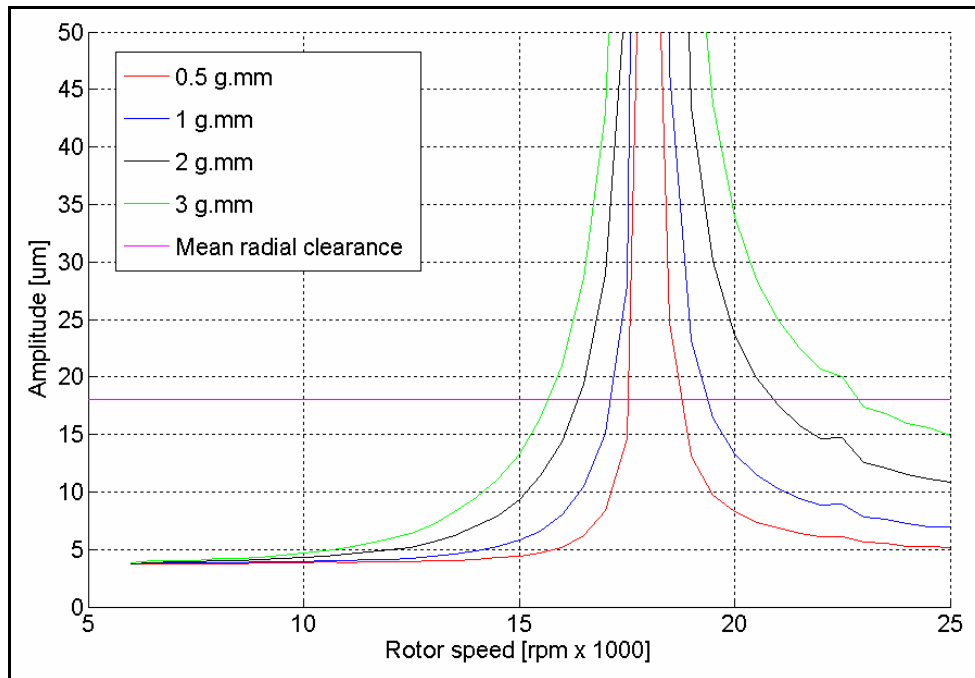


Figure 4.13: Whirl amplitude of the rotor end as a function of the residual imbalance and rotor speed – no damping assumed ($a = 20$ mm).

As seen in Figure 4.12 synchronous whirl occurs at approximately 302 Hz (18 120 rpm) - here the rotor frequency equals the frequency of the backwards whirl mode and the whirl amplitude increases significantly. In this case of zero damping, the amplitude would rise infinitely as the rotor passes through the frequency of the natural mode, but is limited by rotor contact. An increase in balancing precision is seen to produce the highest reduction in the rotor amplitude at speeds close to the resonant condition.

If one incorporates a damping coefficient of 150 Ns/m for the total axial damping and 1500 Ns/m for the total radial damping (as estimated from experimental testing, Chapter 5) the following results are obtained:

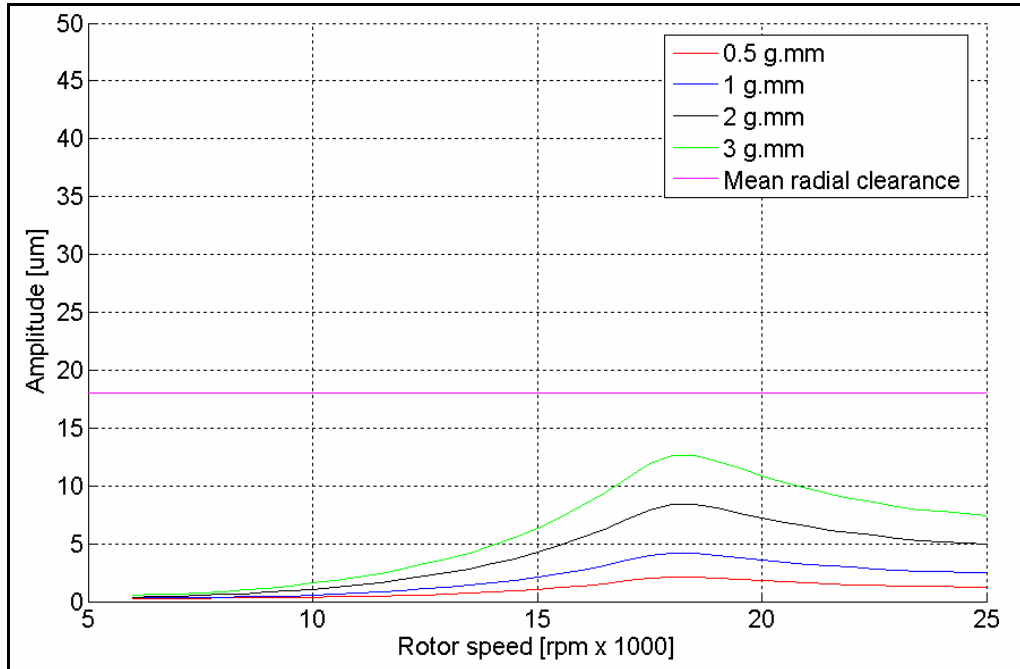


Figure 4.14: Whirl amplitude of the rotor end as a function of residual imbalance and rotor speed – damping (150 Ns/m axial, 1500 Ns/m radial) assumed ($a = 20$ mm).

This level of damping results in a marked reduction in rotor amplitude throughout the speed range, though specifically in the region of and after the whirl frequency. The amplitude of the motion is seen to increase in proportion to the residual imbalance. If this level of damping is indeed representative of the air film then a residual imbalance of 3 g·mm would seem to be sufficient to prevent rotor contact.

Of course, the equilibrium position and orientation of the rotor must also be taken into account as it would not coincide with the geometric centre of the bearing – thus the point of rotor contact would be less than indicated in the above sketches. The equilibrium position would typically be limited to $\frac{1}{5}$ of the MRC while ensuring the maximum amplitude does not exceed $\frac{1}{2}$ the MRC. Factors which affect the equilibrium position of the rotor are the rotor weight and static forces applied to the rotor.

4.2.6.2. The effect of axial imbalance position on motion amplitudes

The effect of the distance from the CG to the position of the imbalance (a) is now investigated. Results for damped and undamped cases are as follows:

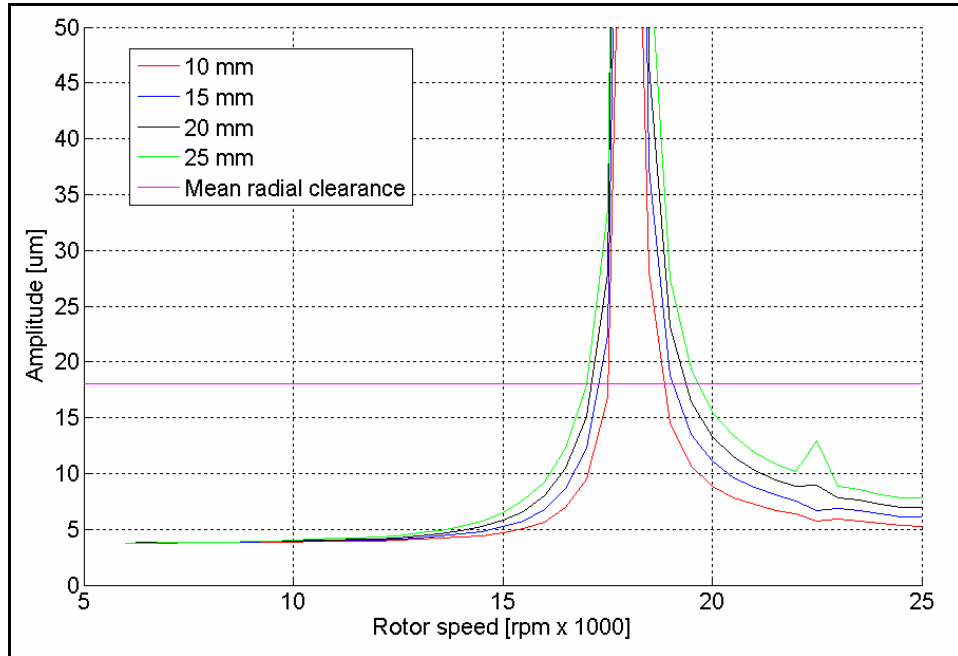


Figure 4.15: Whirl amplitude of the rotor end as a function of axial imbalance position and rotor speed – no damping assumed (residual imbalance = 1 g.mm).

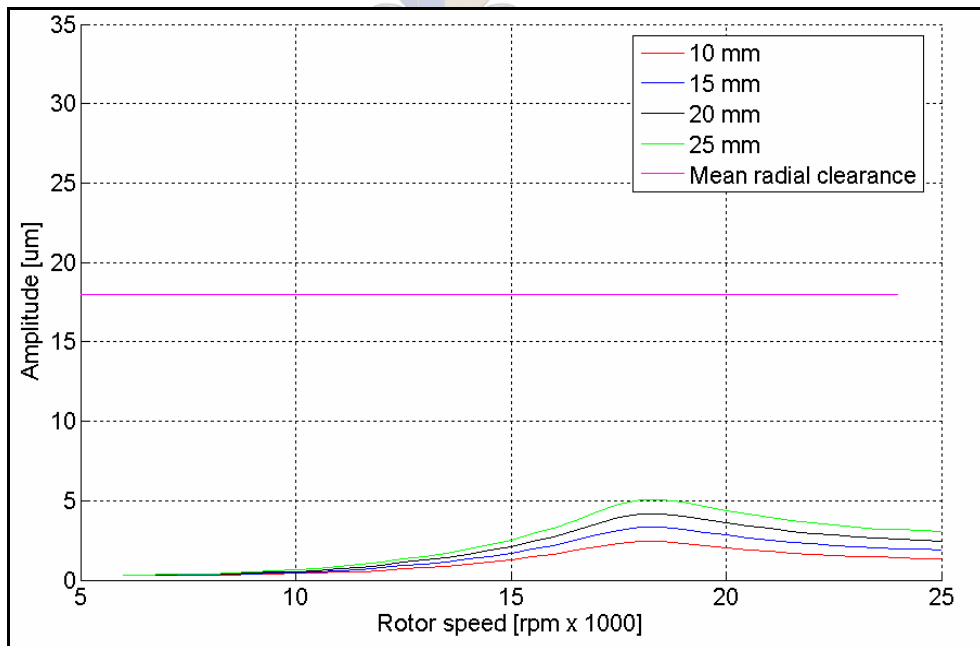


Figure 4.16: Whirl amplitude of the rotor end as a function of axial imbalance position and rotor speed – damping (150 Ns/m axial, 1500 Ns/m radial) assumed (residual imbalance = 1 g.mm).

The axial position of the imbalance does not have as large an effect on the amplitude as the residual imbalance does. Consequently the length of the journal can be increased (to increase the angular stiffness) without the distance from the thrust faces (position of the imbalance) to the CG of the rotor becoming a significant problem.

4.2.7. The angular stiffness

The angular stiffness is defined in the theory by the following equation:

$$K_{ang} = \frac{K_{rad} l_j^2}{H} \quad (\text{Nm/rad}) \quad (4.10)$$

In the Euler model a different method was used to calculate the angular stiffness. The stiffness of each individual spring is obtained from the radial stiffness and the number of springs; the angular stiffness is then calculated from the individual spring stiffness and the position of the springs relative to the CG. Due to this independent calculation some investigation was done into the factors which affect its magnitude and accuracy.

4.2.7.1. The effect of the number of springs on the angular stiffness

The number of springs used to model the air film affects only the accuracy of the angular stiffness, as the axial and radial stiffness values are given. Shown below is a plot of the angular stiffness against the number of springs used for the calculation.

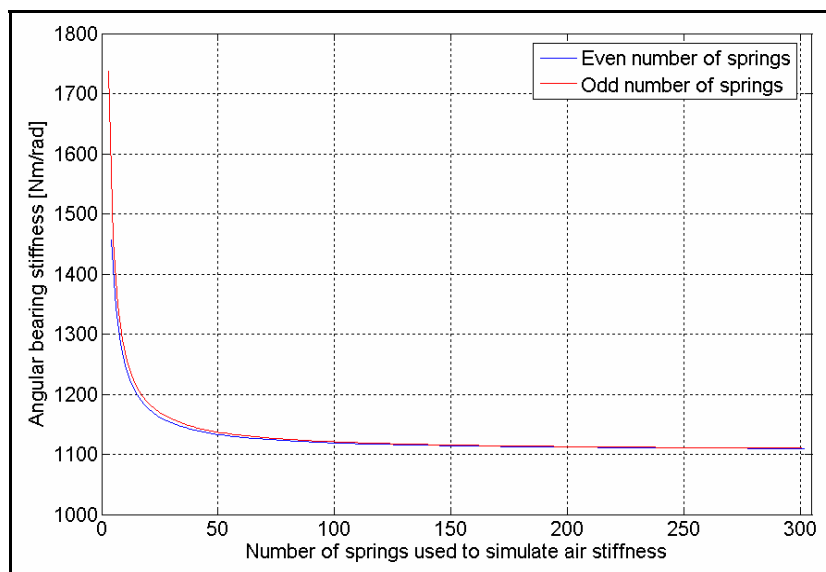


Figure 4.17: The angular bearing stiffness plotted against the number of springs used to represent the gas film stiffness ($K_{rad} = 13 \text{ MN/m}$, $l_j = 36 \text{ mm}$).

Table 4.2 shows the accuracy of the calculated stiffness values relative to the value calculated for 3000 springs (taken as 'exact'). In order to calculate the stiffness to within ~ 10 N·m/rad (which would ensure the natural frequency to within roughly 2 Hz) more than 135 springs would have to be used. For all the simulations, 200 springs were used to simulate the gas film stiffness as computation time was not a problem.

Table 4.2: The accuracy of the angular stiffness calculation as per the number of model springs.

Accuracy	Number of springs required
To within 1%	~ 135
To within 0.5%	~ 250
To within 0.1%	~ 940
To within 0.01%	~ 2470

4.2.7.2. Effect of radial stiffness on the angular stiffness for various centre of gravity positions

Aerostatic bearing theory suggests a linear relationship between the radial and angular stiffness (Equation 4.10) which the Euler model confirms (Figure 4.18 below).

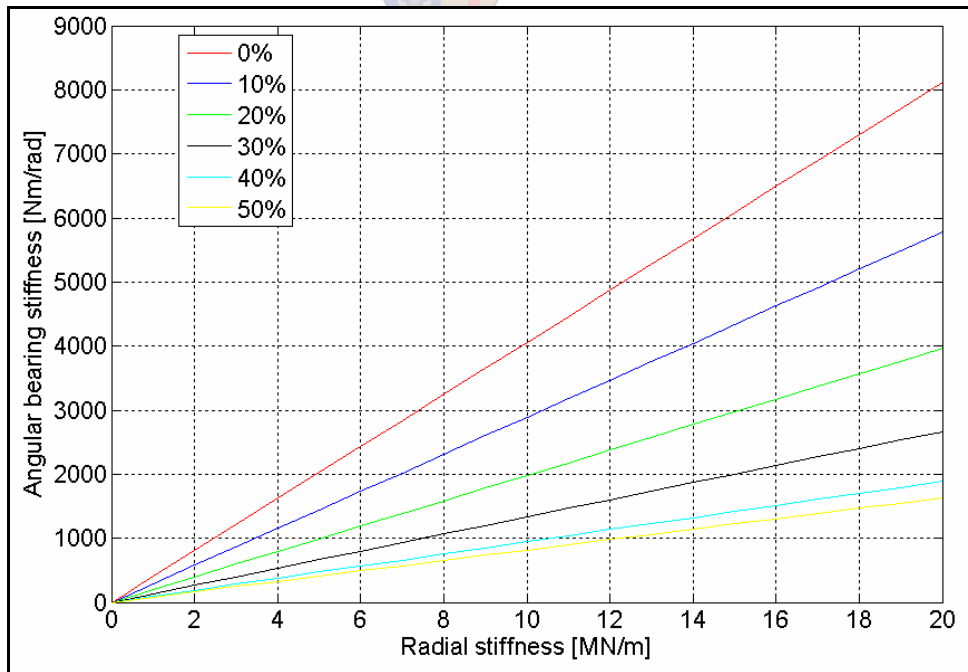


Figure 4.18: The effect of the radial stiffness and the centre of gravity position (expressed as a percentage of the journal length away from the journal end) on the angular stiffness ($Q = 3$).

The model was also able to show that if the CG of the journal coincides with the journal geometric centre (50% from one end), the angular stiffness of the bearing would be at a minimum and would increase as the CG was shifted towards the end of the journal. This can be explained by the fact that the angular stiffness is proportional to the square of the journal length. If the CG coincides with a particular end of the journal, the springs at the other end would theoretically contribute four times the restoring moment about the CG than if the CG was in the middle of the journal. However, due to the variation of the spring stiffness along the journal length the increase in angular stiffness doesn't increase in proportion to the movement of the CG along the journal. For $Q = 1$, the angular stiffness is increased almost four times when the CG position is moved from the middle to the end of the rotor. If $Q = 5$, the stiffness is increased five and a half times. This is shown more clearly in Figure 4.19 below.

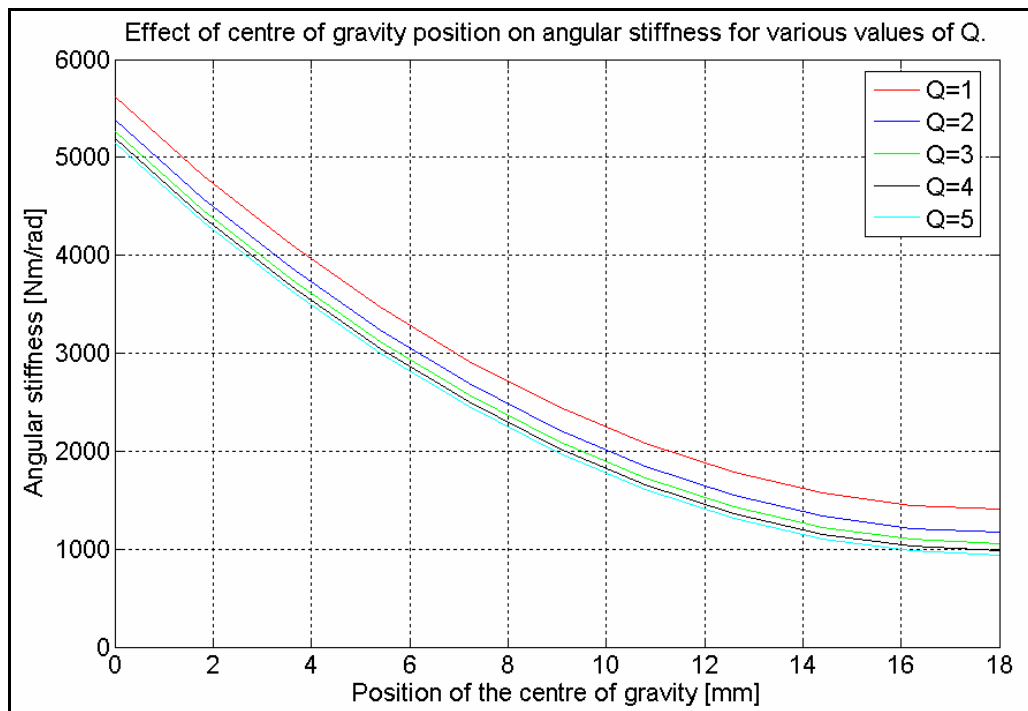


Figure 4.19: The effect of the position of the rotor's centre of gravity (expressed in millimetres from the journal end) on the angular stiffness for different spring stiffness ratios ($K_{rad} = 13 \text{ MN/m}$, $l_j = 36 \text{ mm}$).

4.2.7.3. Effect of bearing length on the angular stiffness for various CG positions

The model shows that the angular stiffness of the bearing is proportional to the square of the bearing length, which is what the theory states (Equation 4.10). This is shown in Figure 4.20 below. Again the effect of the CG position that was discussed above is observed. It can therefore be deduced that the most effective way of increasing the angular stiffness of a bearing would be to increase the length of the journal section, bearing in mind that the increased distance of the thrust faces from the centre of gravity would not be a significant problem in terms of imbalance.

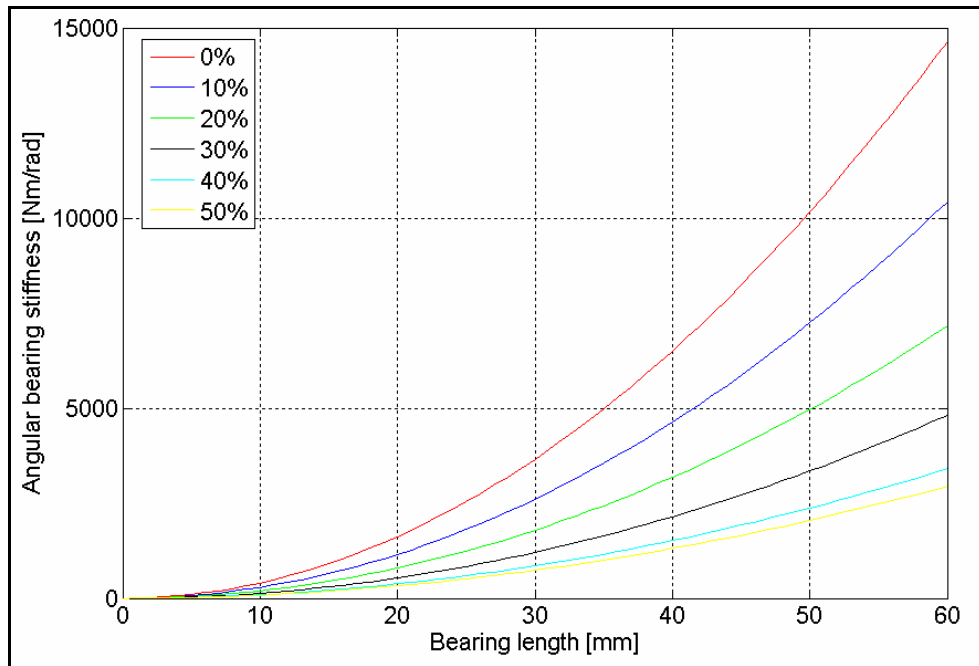


Figure 4.20: The effect of the bearing length and centre of gravity position (expressed as a percentage of the journal length away from the journal end) on the angular stiffness ($K_{rad} = 13MN/m$).

4.2.7.4. The angular stiffness constant, H , and its relation to spring stiffness ratio Q

The accepted value for the constant H in Equation 4.10 for a quarter-station bearing is 16 (Powell, 1970). For clarity the relationship is restated below:

$$H = \frac{K_{rad} l_j^2}{K_{ang}} \quad (4.11)$$

A half-station bearing would have a larger value for H in view of its lower angular stiffness. The constant H is plotted against the stiffness ratio Q in Figure 4.21 below.

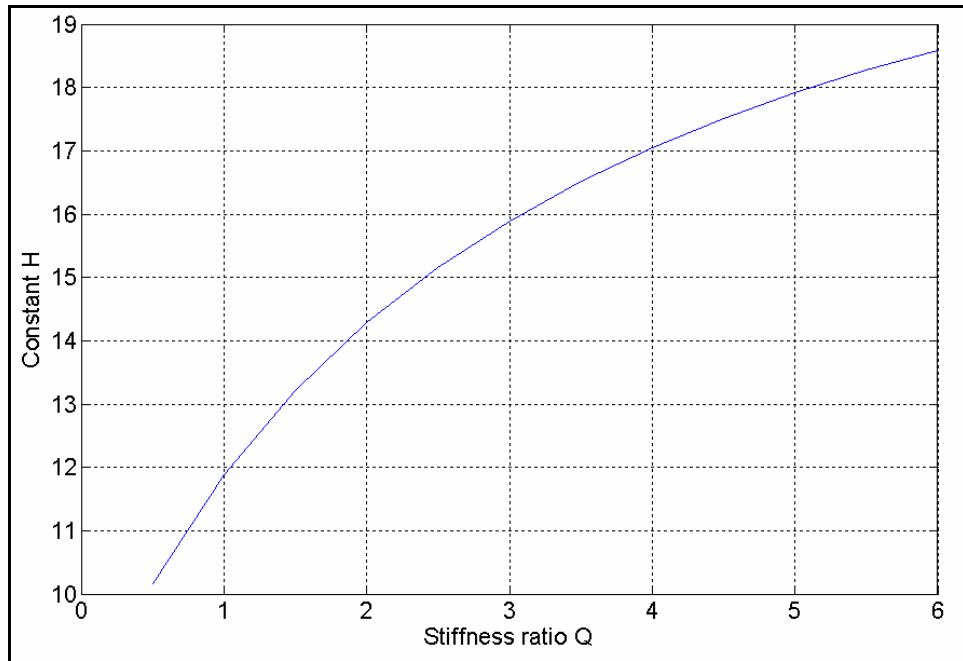


Figure 4.21: Variation of the constant H against the spring stiffness ratio Q .

In view of the accepted value of $H = 16$ for quarter-station bearings, the equivalent spring stiffness ratio Q would be in the region of 3. The effect of bearing length and the stiffness ratio on the angular stiffness of a bearing is plotted in Figure 4.22. It shows that increasing the angular stiffness by reducing the stiffness ratio is more effective as the journal length increases.

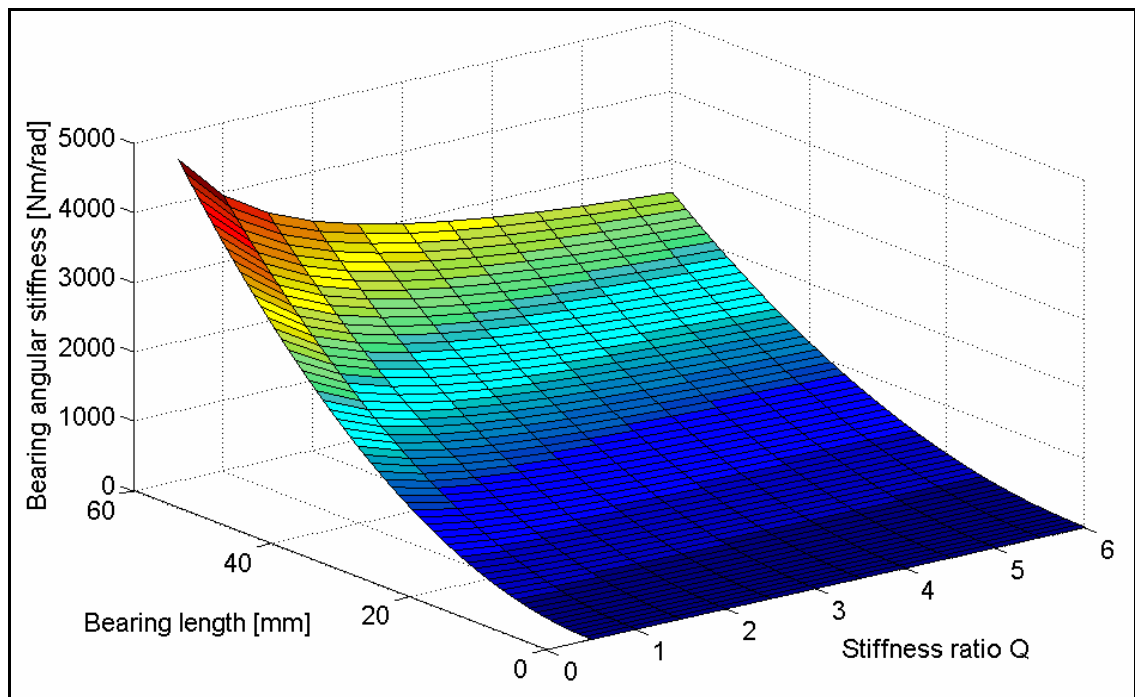


Figure 4.22: Effect of stiffness ratio and bearing length on angular stiffness ($K_{rad} = 13 \text{ MN/m}$).

Chapter 5: Experimental Modal Analysis and Results

In this chapter the experimental modal analysis (EMA) and the results obtained are discussed. EMA is essentially an extension of frequency-response-function (FRF) determination, where the structure's response to a certain input force is measured. The aim of the EMA would be twofold: Firstly it would confirm the frequencies of the rigid modes calculated by the Euler model as well as the flexible body modes obtained from the FEM analysis. Secondly it would produce reasonably accurate estimates of the damping of the modes. The Euler model would then be calibrated using the damping information to improve its accuracy in terms of the rotor displacement prediction.

5.1. Modal analysis experimental set up

The modal testing to determine the frequencies and damping of the rotor modes was done using both impulse excitation (using a modal hammer) and random excitation (using an electromagnetic shaker). Both methods achieved near identical results, although specific modes related to the shaft driver (termed the *stinger*) and the shaker were observed when using the random excitation. The frequencies and damping of the modes were investigated against the bearing supply pressure.

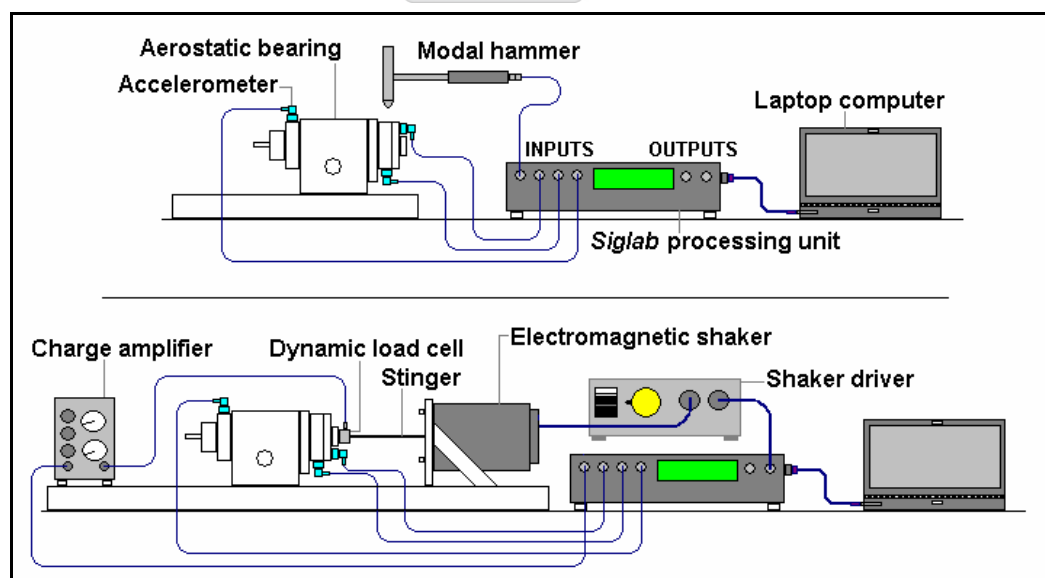


Figure 5.1: Diagram illustrating the test set up for the modal analysis using impulse (top) and random (bottom) excitation.

A Siglab signal analyser (www.spectraldynamics.com) was used to process the accelerometer signals before being fed to a laptop computer. The Matlab program on the laptop was used for post processing of the data as well as a function generator in the case of the random excitation. A dynamic load cell and suitable charge amplifier were also used to measure the load applied to the rotor during the random excitation. The modal hammer incorporates a load cell in its head. All tests were done over a frequency range of 0 - 2 kHz. For the impulse excitation 20 averages were taken per test. For the random excitation 60 averages were taken.

5.2. Investigation of the flexible body modes for Design A

Flexible body impulse tests were performed to confirm the results obtained by the FEM analysis. The assembled rotor was placed on a soft foam surface to simulate *free-free* conditions. Results for the radial impulse testing are shown below, illustrating the first two bending modes at ~3900 Hz and ~8200 Hz.

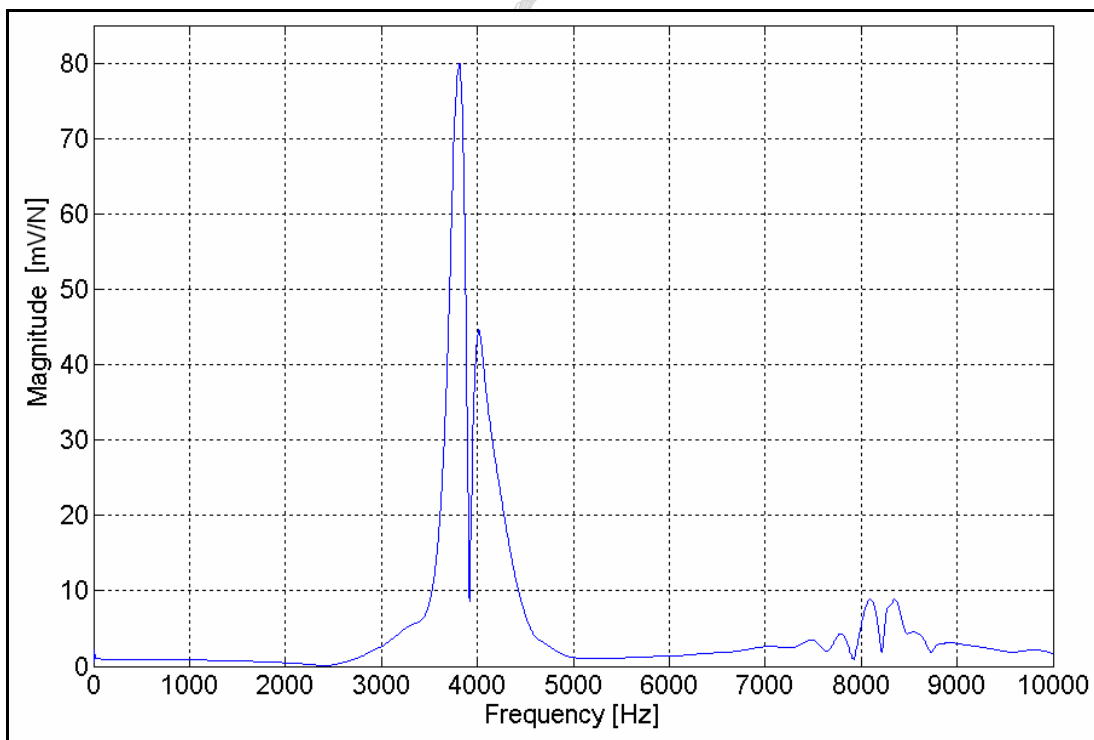


Figure 5.2: Transfer function showing the first two bending modes of the rotor.

The reason for the pairs of modes could be the real difference in geometry between the *xy* and *xz* planes of the rotor (for example the presence of the spanner flats resulting in asymmetry). The first bending mode is 6% higher than predicted by the FEM analysis (~3690 Hz). The second mode 3% higher than the FEM results

(~8000 Hz). The reason for this could be that the hard-anodised rotor is slightly stiffer than the pure aluminium rotor modelled in the FEM analysis.

The axial mode of vibration (Figure 5.3) was measured at approximately 8600 Hz. The frequency is roughly 8% higher than the FEM model and this again could be attributed to the stiffening affect of the hard-anodising.

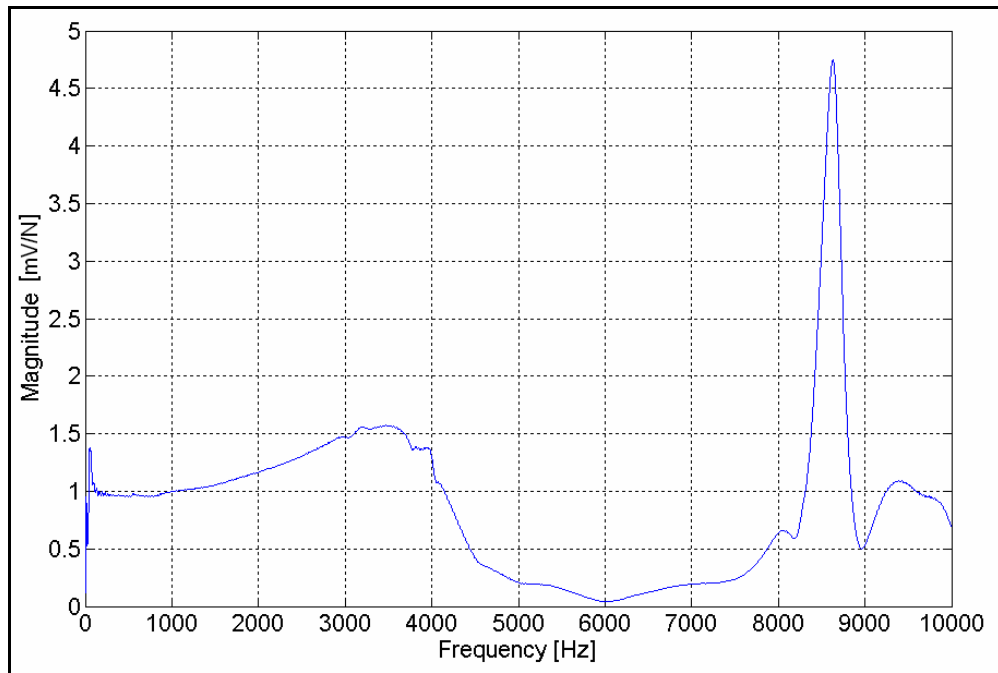


Figure 5.3: Transfer function showing the axial mode of the rotor.

Thus it was confirmed that the flexible body modes of the aluminium rotor were well above the 660 Hz limit required for the rigid body assumption to be valid. Tests with the rotor supported in the bearing showed very little difference to the above results.

5.3. Investigation of the frequencies of the rigid body modes

In order to confirm the results obtained from the Euler model, the following parameters were investigated:

1. The axial stiffness of the air film and the frequency of the axial mode.
2. The radial stiffness of the air film and the frequency of the angular mode.
3. The damping ratio of the air film for the axial and angular modes.

Only the x translation (axial) and the \varnothing/θ angular modes were investigated as these are the modes with the lowest natural frequencies and would be the most critical to

rotor stability (Darlow, 1989). All the tests were done with the rotor stationary as conventional tethered accelerometers were used. The FFT results given of the Euler model are included for comparison (equivalent to tests at 6 bar and 0 rpm).

5.3.1. The x translation (axial) mode

Investigation of the axial mode was done by attaching accelerometers to the thrust faces in the axial direction. The excitation was applied to the front of the rotor along its axis to ensure minimal excitation of the angular mode.

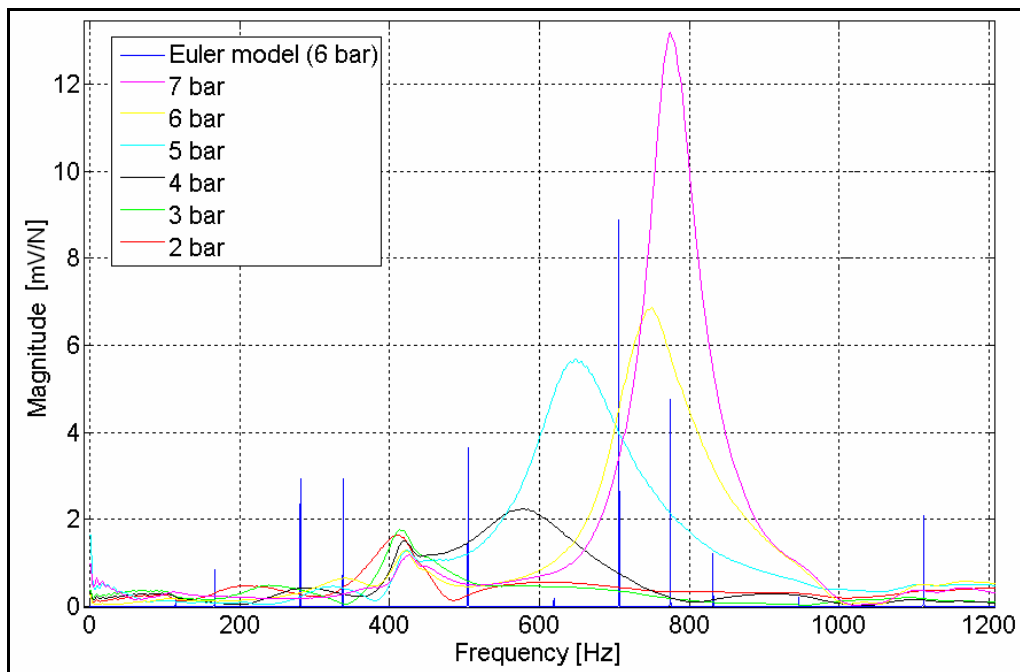


Figure 5.4: A transfer function for an axial impulse test on Design A.

The frequency of the axial mode increased with increasing supply pressure due to the increased pressure at the thrust face inlet and the corresponding higher thrust stiffness. At 6 bar the frequency of the axial vibration was 745 Hz, roughly 6% higher than predicted by the Euler model (706 Hz). The reason for this could be due to the journal clearance being greater than specified, resulting in a larger thrust inlet pressure than expected (due to a lower pressure loss along the journal). The thrust bearing stiffness is also dependent on the MAC. Reducing the clearance from 25 μm to 15 μm increased the frequencies of the axial modes by approximately 20%. For Design B the axial mode at 6 bar occurs at 467 Hz (Figure 5.5), roughly 4% higher than predicted by the Euler model (450 Hz). This could be due to the same reason as given for Design A.

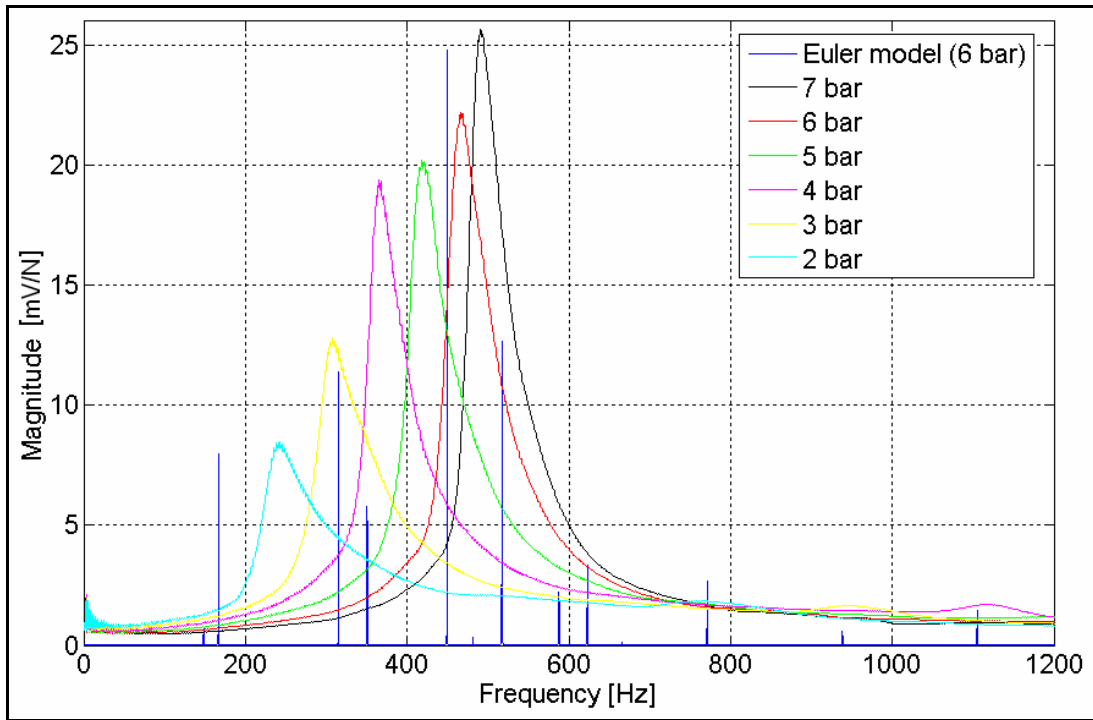


Figure 5.5: A transfer function for an axial impulse test on Design B.

5.3.2. The \varnothing and θ angular (transverse) modes

Investigation of the frequency of the angular modes was done by applying the excitation to the top of the front thrust face in the radial direction. The accelerometers were placed on the opposite side of the face in the same direction.

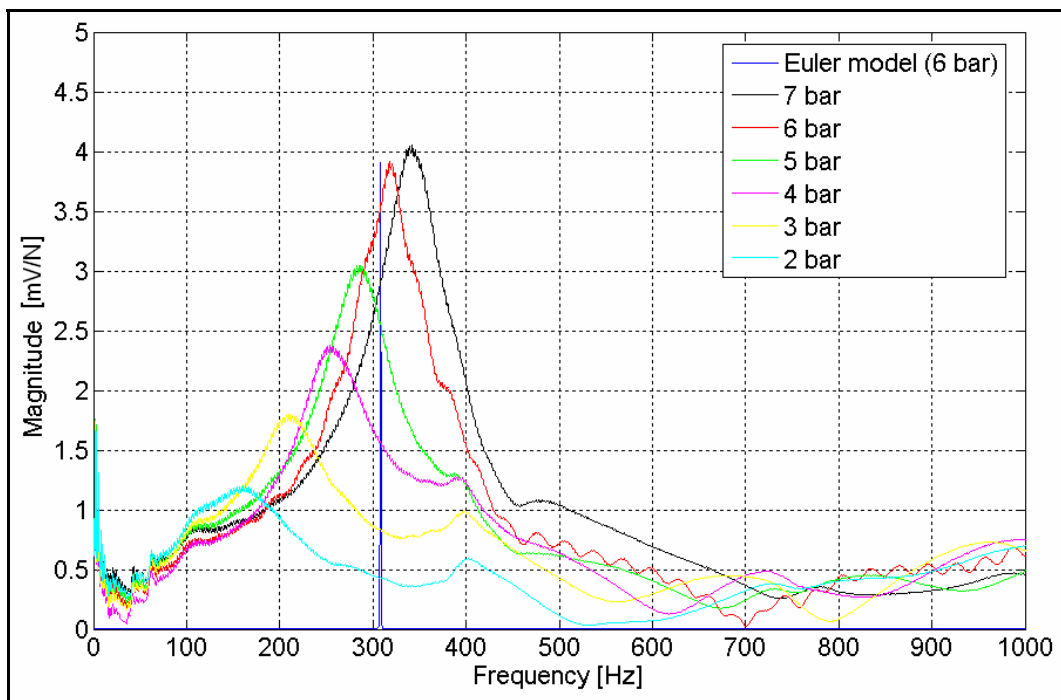


Figure 5.6: A transfer function for a radial impulse test on Design A.

Clearly discernable peaks were obtained at the higher supply pressures. Below 3 bar, the definition of the peaks suffered and it was difficult to accurately define the frequency of the mode. At 6 bar the frequency of the mode is approximately 317 Hz, 2.5% higher than calculated by the Euler model (309.5 Hz). This could be due to the transverse moment of inertia being less than calculated. Also, the thrust bearings do contribute to the angular stiffness, but this is not considered in the Euler model. As expected, an increase in supply pressure resulted in an increase in the frequency of the mode due to the increased angular stiffness. This trend is confirmed for Design B (Figure 5.7).

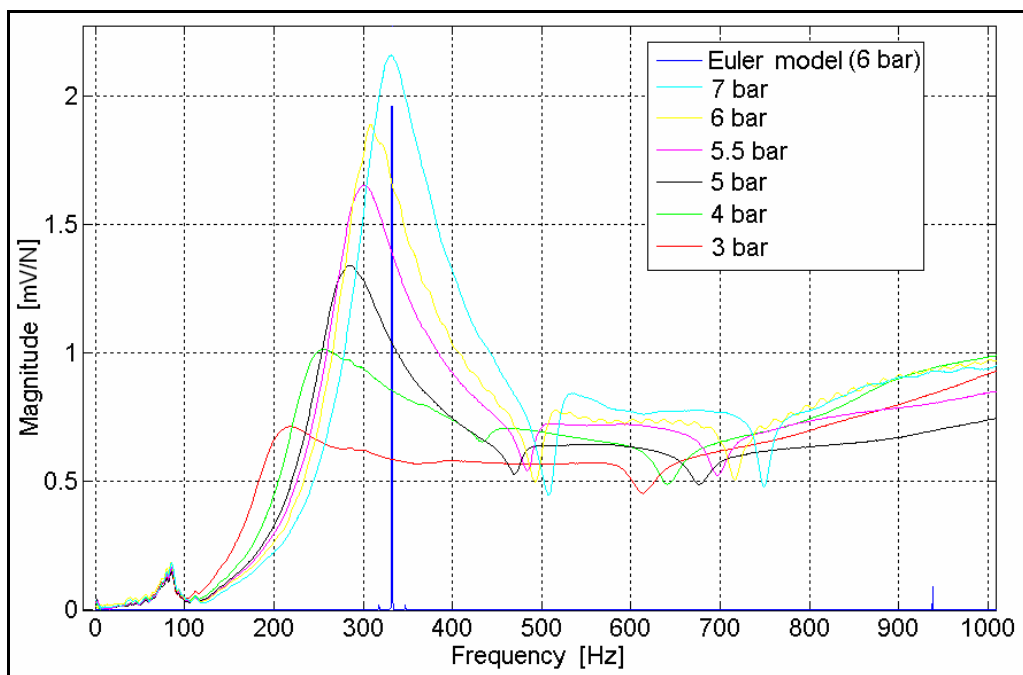


Figure 5.7: A transfer function for a radial impulse tests on Design B.

At 6 bar the frequency of the mode is approximately 312 Hz - the Euler model estimation of 332 Hz is therefore a reasonable one, albeit roughly 6% higher. This could be due to either transverse moment of inertia being higher than calculated or the angular stiffness being lower than calculated – the second reason of which would be more likely. Numerous factors could cause a decreased angular stiffness, such as a larger radial clearance, a larger pressure drop through the orifices, etc.

5.4. Investigation of the damping of the rigid body modes

Both the half-power point method (HPP) and logarithmic decrement (LD) method were used to estimate the damping ratio, ζ , of the air film, using the response to

excitation in the time and frequency domain respectively. An exponential function, $y(t) = Ae^{-\zeta\omega_n t}$ was fitted to the decay plot allowing an additional estimate of the damping ratio to be made. The LD method gave good damping estimates at high supply pressures, but at pressures below 4 bar the definition of the decay and the accuracy of the results suffered.

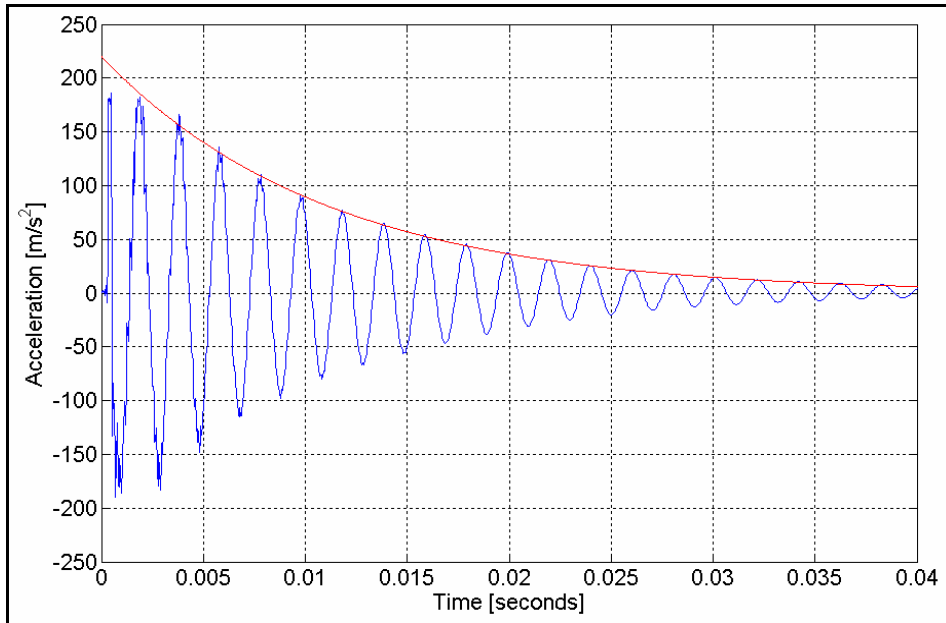


Figure 5.8: A characteristic response to an axial impulse in the time domain.

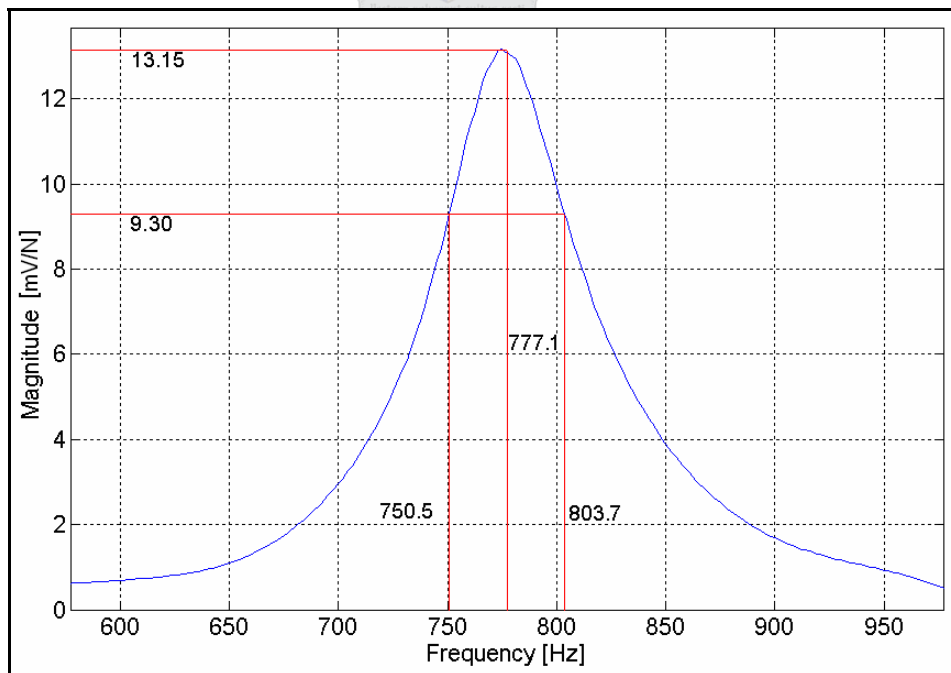


Figure 5.9: The half-power point method using a specific peak in the transfer function to estimate the damping of the mode.

The accuracy of the half-power point method also suffered at low supply pressures due to poor definition of the transfer function peaks. This was due to the presence of nearby modes and the damping would tend to be exaggerated as the tails of the peaks would not fall away naturally (Figure 5.10).

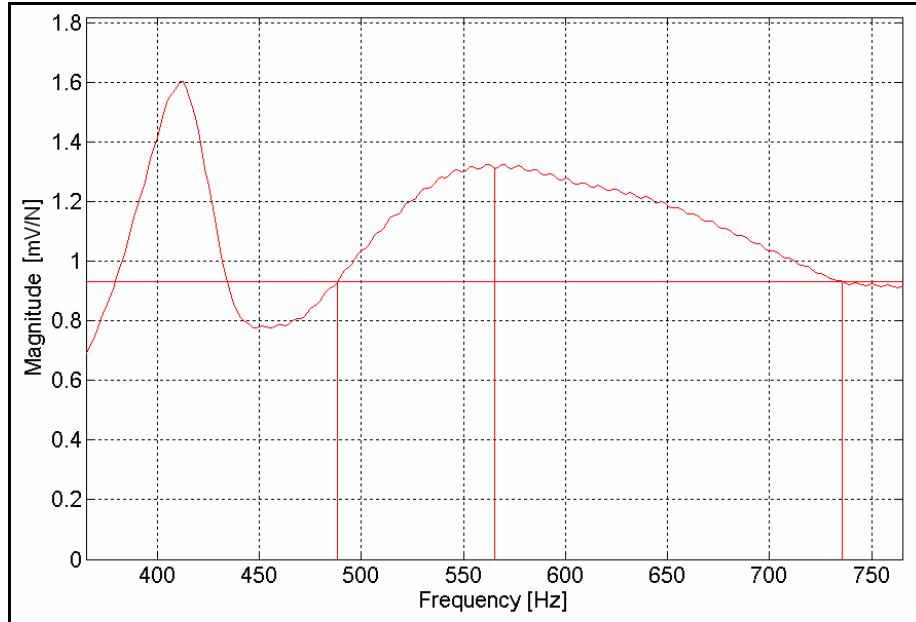


Figure 5.10: Distortion of an axial mode (565 Hz) by a nearby housing mode (412 Hz).

5.4.1. The x translation (axial) mode

Using the two methods mentioned above the damping ratio of the axial mode was determined for the rotors (Figure 5.11). For Design A both methods are in good agreement at the higher supply pressures. At lower supply pressures the coefficients deviate considerably which was due to the distortion of the plots – the half-power point tended to overestimate the damping as described above. The problem was so severe that results could not to be calculated for tests below 3 bar. Better results were obtained at the lower pressures for Design B, and the two methods gave similar damping coefficients. Design B exhibited lower damping due to its smaller thrust area and larger MAC. In general it appears that the damping ratios decrease with increased supply pressure.

The damping coefficient C can be calculated by multiplying the damping ratio with the critical damping coefficient C_{cri} :

$$\begin{aligned}
 C &= \xi C_{cri} \\
 C &= 2\zeta M \omega_n
 \end{aligned}
 \tag{5.1}$$

where M is the rotor mass and ω_n the natural frequency of the mode (rad/s). The damping coefficients are plotted as a function of supply pressure in Figure 5.12.

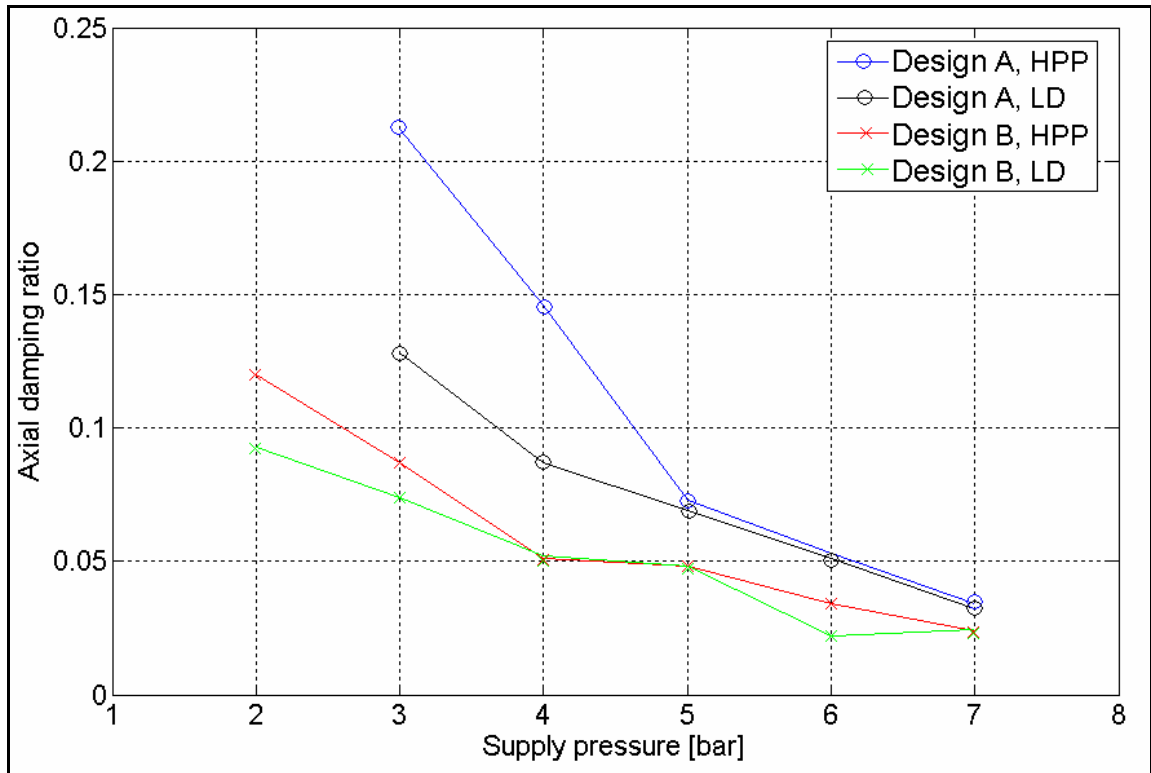


Figure 5.11: The axial damping ratios for the two rotors.

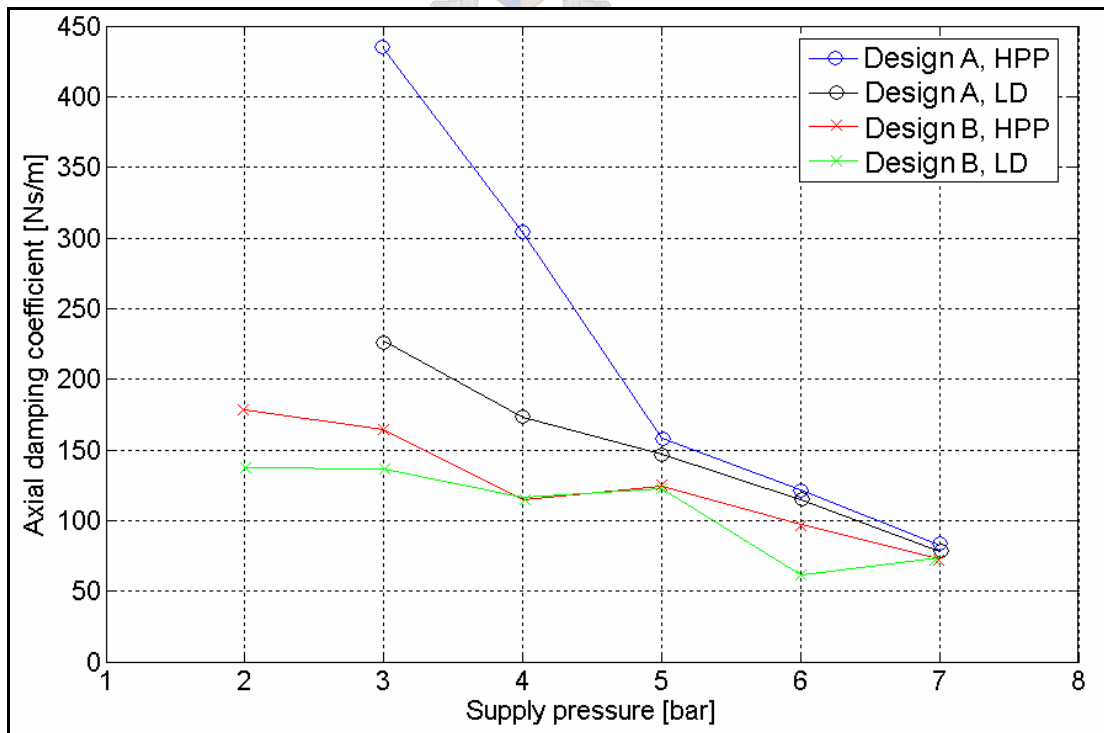


Figure 5.12: The axial damping coefficients for the two rotors.

Figure 5.12 suggests that the damping coefficients decrease slightly with increased supply pressure, although the dependency on supply pressure is not as great as for the damping ratio. A reasonably accurate estimation of the damping can be made (realizing the limitations at the low supply pressures) and these estimates can be used in the Euler rigid body model to predict the motion more accurately.

Powell (1970) stated that experiments available at the time indicated that damping was independent of the supply pressure and that it is more a function of clearance ratio (MRC/r_j) and bearing plan area. The small dependence of the damping coefficients on pressure was seen in Figure 5.12 as was the effect of area and clearance, although the latter was not specifically studied.

5.4.2. The ϕ and θ angular (transverse) modes

The damping was calculated in the same manner as for the axial mode and the results are presented below for the two rotor designs.

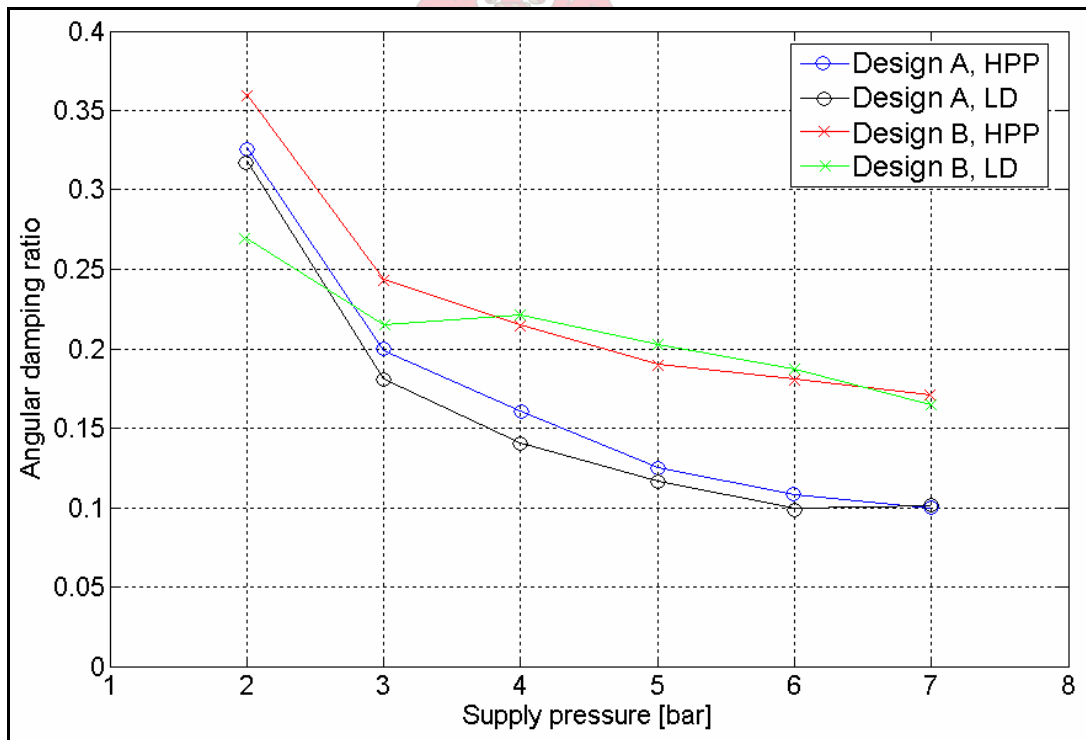


Figure 5.13: The angular damping ratios for the two rotors.

An increase in supply pressure is seen to reduce the damping ratio as with the axial mode. The damping of Design B is higher due to its larger plan bearing area. Again

the accuracy of the results for tests below 4 bar is compromised due to the same reasons stated before.

The angular damping coefficient of the angular mode can be determined in a manner similar to the axial mode. The applicable equation is:

$$C_{ang} = 2\zeta I \omega_n \quad (\text{N}\cdot\text{m}\cdot\text{s}/\text{rad}) \quad (5.2)$$

The results are shown in Figure 5.14 which suggests that the dependency of the damping coefficient on supply pressure is small.

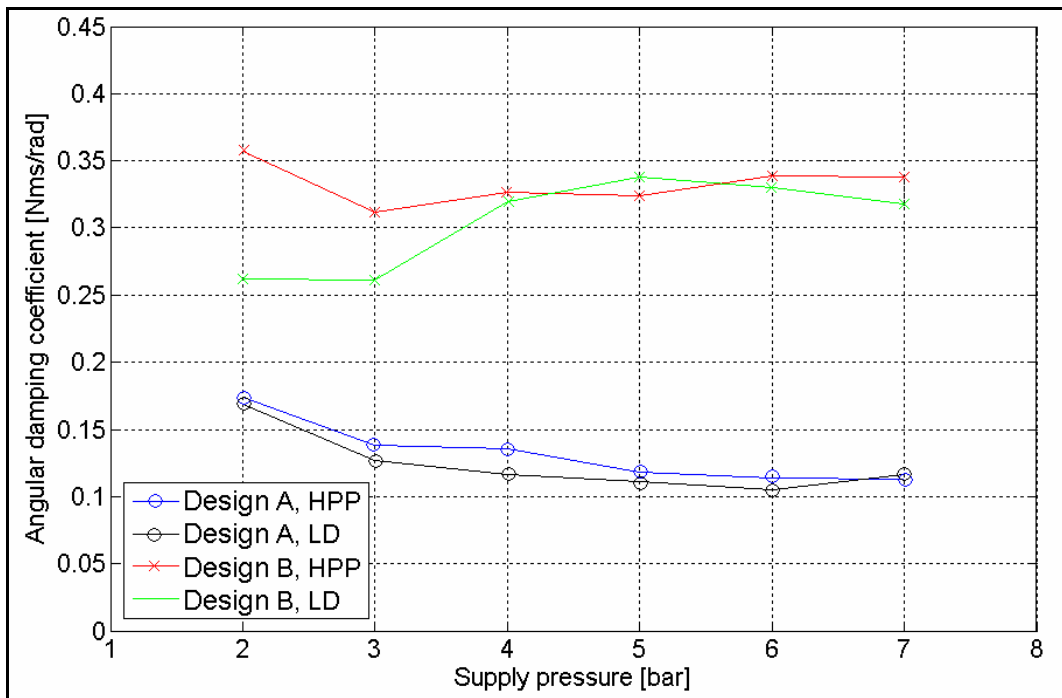


Figure 5.14: The angular damping coefficients for the two rotors.

5.4.3. The y and z translation (radial) mode

The above angular damping coefficients are not useful in that they cannot be used directly in the Euler model, because the angular damping is provided by a series of translational dampers. However it is possible to calculate the damping coefficients of these translational dampers by using the following equation which defines the moment due to damping (from the derivation in Appendix A):

$$\bar{T}_{damp\phi} = -\dot{y}C_{damp}\Sigma - \dot{\phi}C_{damp}\Sigma\Sigma \quad (\text{N}\cdot\text{m}) \quad (5.3)$$

Assuming the rotor is in pure rotation, i.e. $\dot{y}=0$, the angular damping coefficient is defined as:

$$C_{ang} = C_{damp} \Sigma \Sigma \quad (\text{N}\cdot\text{m}\cdot\text{s}/\text{rad}) \quad (5.4)$$

$$C_{ang} = \frac{C_{rad}}{s} \Sigma \Sigma \quad (\text{N}\cdot\text{m}\cdot\text{s}/\text{rad}) \quad (5.5)$$

The total radial damping coefficient of the bearing is thus:

$$C_{rad} = \frac{C_{ang}}{\Sigma \Sigma / s} \quad (\text{N}\cdot\text{s}/\text{m}) \quad (5.6)$$

$\Sigma \Sigma$ is a term defined in Appendix A as the following:

$$\Sigma \Sigma = \sum_{j=1}^s \left[(v-1) \frac{l_j}{s-1} - f \right]^2 \quad (\text{m}^2) \quad (5.7)$$

This term is dependent only on the length of the journal and the position of the CG.

The $\frac{\Sigma \Sigma}{s}$ term is shown below in Figure 5.15 plotted against the number of springs used in the model. The convergent values for the term are 1.09×10^{-4} and 1.80×10^{-4} for Designs A and B respectively. With these values substituted in Equation 5.6 the radial damping coefficients can be estimated (Figure 5.16).

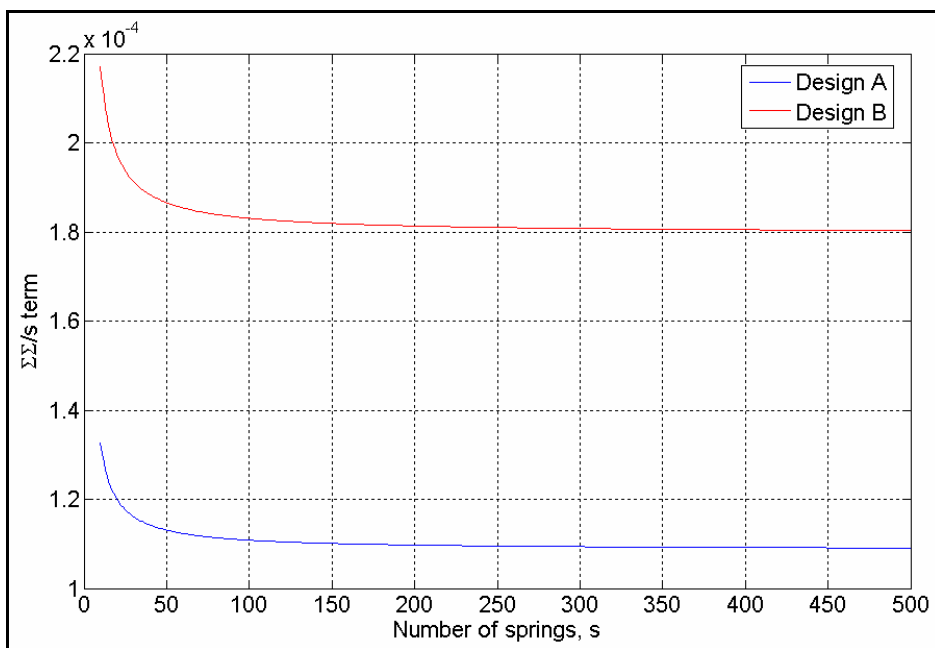


Figure 5.15: The $\Sigma \Sigma / s$ term plotted against the number of model springs.

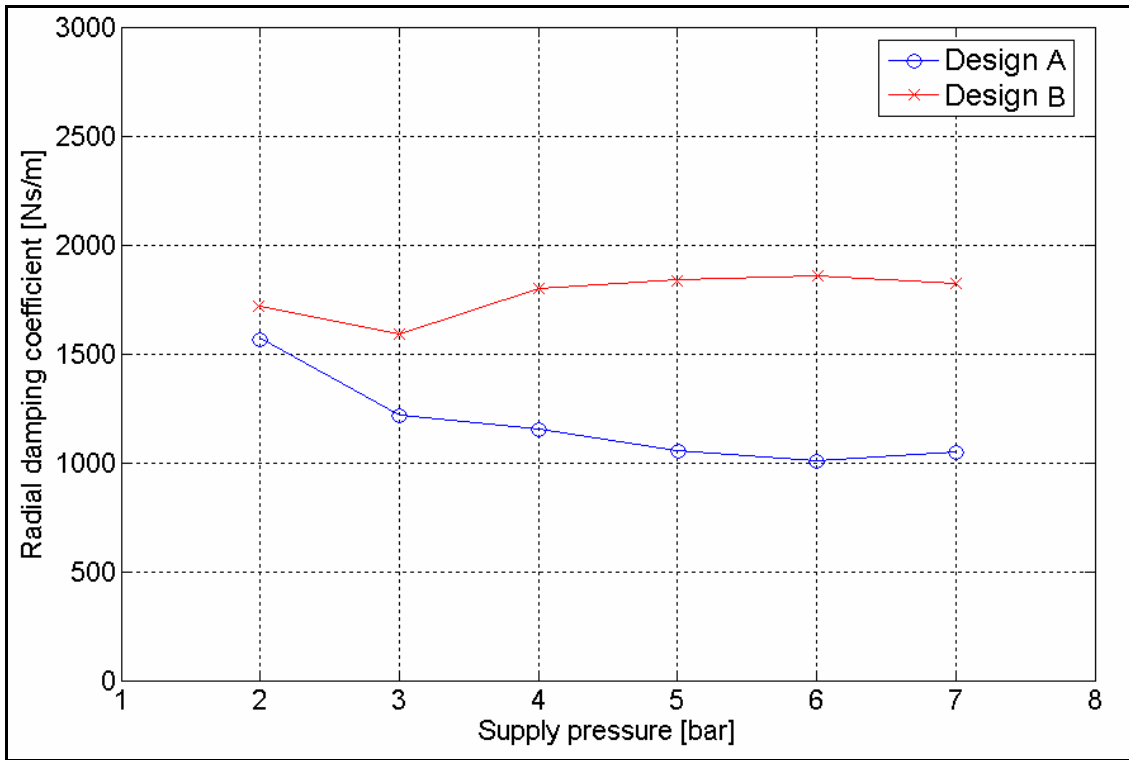


Figure 5.16: The radial damping coefficients for the two rotors.

The small dependency on supply pressure is displayed as per the other modes. In order to examine the damping ratio Equation 5.1 is rewritten as:

$$\xi = \frac{C}{2M\omega_n} \quad (5.8)$$

The damping ratio can thus be calculated as a function of the bearing pressure. However, before this can be done the frequencies of the modes need to be determined. Using estimates of 1113 Hz and 939 Hz for the frequencies of the translation modes for Design A and B respectively at 6 bar, the frequencies at the other supply pressures were estimated using the following equations:

$$f_A(P_o) = 1113 \sqrt{\frac{P_o}{6}} \quad (\text{Hz}) \quad (5.9)$$

$$f_B(P_o) = 939 \sqrt{\frac{P_o}{6}} \quad (\text{Hz}) \quad (5.10)$$

where P_o is the supply pressure (bar). The damping ratios can then be calculated using Equation 5.8 and are shown on the following page.

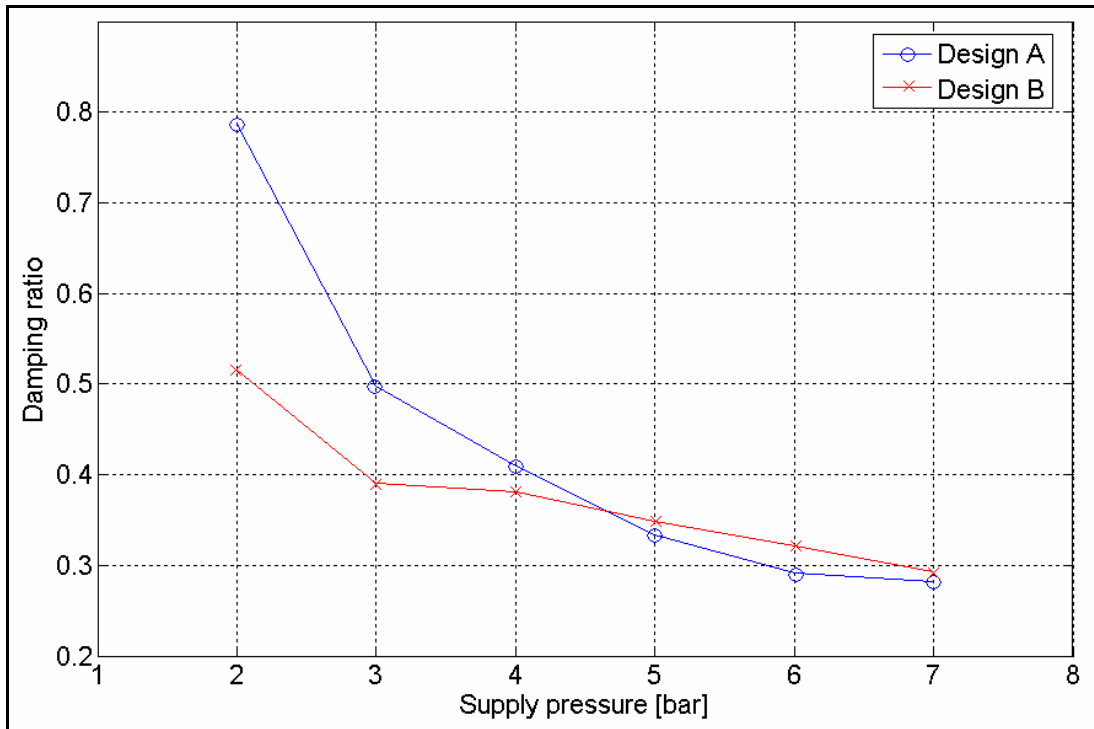


Figure 5.17: The radial damping ratios for the two rotors.

Very little literature could be found concerning the measurement of damping ratios of aerostatic bearings. In the book *Gas Lubricated Bearings* (Grassam and Powell, 1964) it is noted that the damping ratio is mostly dependent on the clearance ratio. A table from the book is presented below.



Table 5.1: Damping ratio estimates from the bearing clearance ratio (Grassam and Powell, 1964).

Researcher	Journal diameter, $2r_j$	Journal length, l_j	Clearance ratio (MRC/ r_j)	Damping ratio, ξ
Gross	25 mm	25 mm	0.0010	1.0
Allen <i>et al.</i>	50 mm	50 mm	0.0015	0.50 → 0.90
Powell	25 mm	25 mm	0.0082	0.05 → 0.13

The theoretical clearance ratios for Design A and B are 0.0012 and 0.0014 respectively which suggests a radial damping ratio in the region of 0.3 to 0.5. This is in agreement with the estimates plotted in Figure 5.17. For all the modes it was generally seen that the damping coefficients showed little dependency on the supply pressure and it was the increased frequency of the modes that caused the damping ratios to decrease with the increased supply pressure.

5.5. Rotor amplitude investigation

The amplitude of the rotor's motion during operation was measured using a Polytec laser vibrometer. The velocity of the rotor at the blade flange was recorded, and a *Siglab* signal analyser was used to receive and process the signal. The velocity signal was digitally filtered using a 10 – 3000 Hz bandpass filter to reduce the accumulation error of the low frequency data which exaggerated the displacements. The signal was then integrated using a trapezoidal numerical integration technique to produce the displacement signal. Measurements were taken at discrete speeds from 5000 rpm to 12 000 rpm – the test at 10 200 rpm is shown in Figure 5.18.

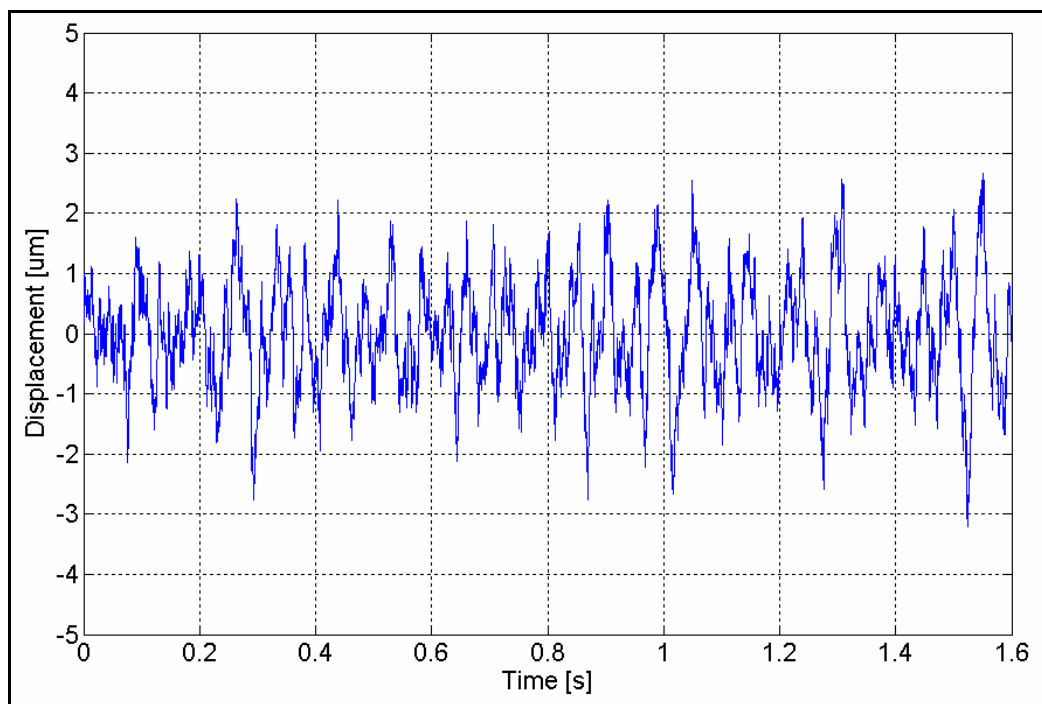


Figure 5.18: The blade flange displacement in the y direction (10 200 rpm).

The amplitudes measured during the tests are summarised in Figure 5.19. It can be seen that the amplitudes are larger than those predicted by the Euler model. This could be due to an over-estimation of the radial damping in the model. Also, the amplitudes do not seem to increase with the rotor speed as expected. The amplitudes are significantly less than the bearing MRC and, while this is an ideal condition, does not explain the rotor contact problems that were experienced. Contact would occur during acceleration of the rotor and it is most likely that the larger forces applied during acceleration (as apposed to steady running) would cause the motion amplitude to be notably larger than those shown in Figure 5.19.

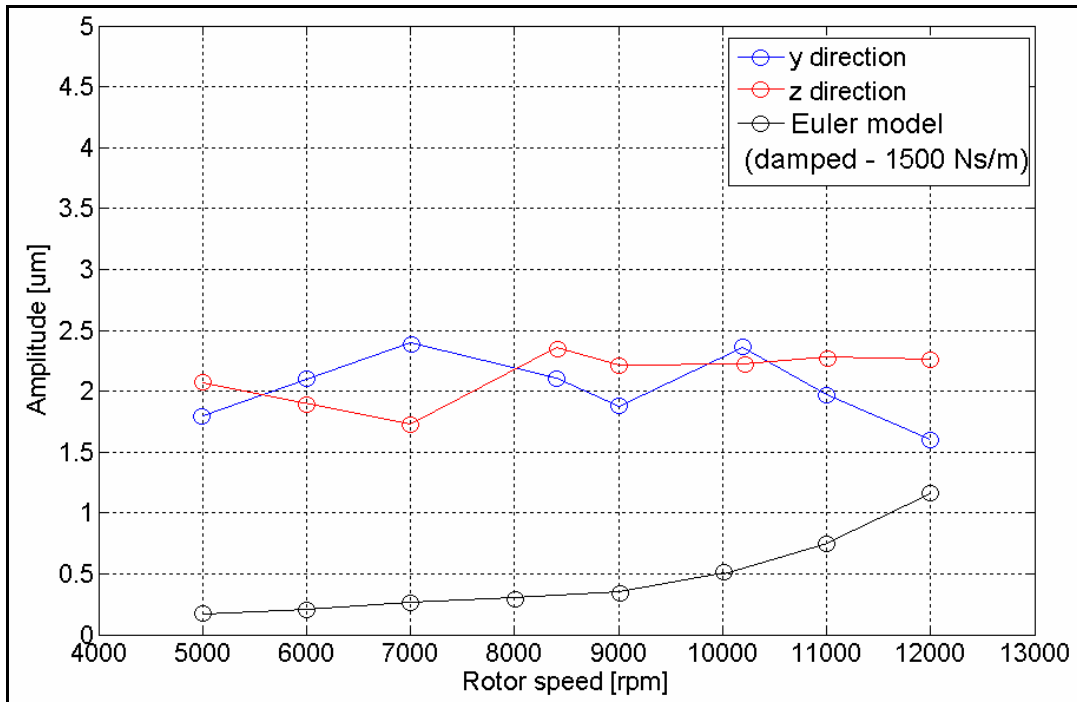


Figure 5.19: The amplitude of the blade flange motion plotted against rotor speed for the y and z directions.

5.6. Sawing tests – vibration levels for the conventional and aerostatic machines

A number of sawing tests were done with a conventional machine and the Design A aerostatic machine driven by the Terry turbine. Accelerometers were positioned on the diamond clamp and the machine base (or housing in the case of the aerostatic machine) for each test. The positions of the accelerometers on the two machines are shown in Figures 5.20 and 5.21. The vibration levels of each machine were compared using FFT plots (Figures 5.22 and 5.23).

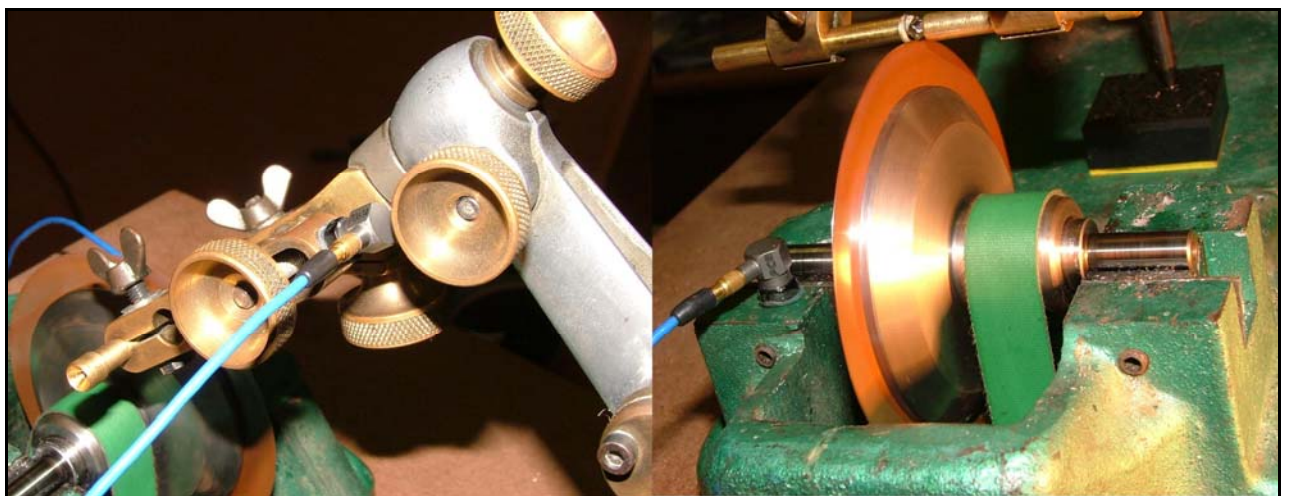


Figure 5.20: The accelerometer placement on the conventional machine.

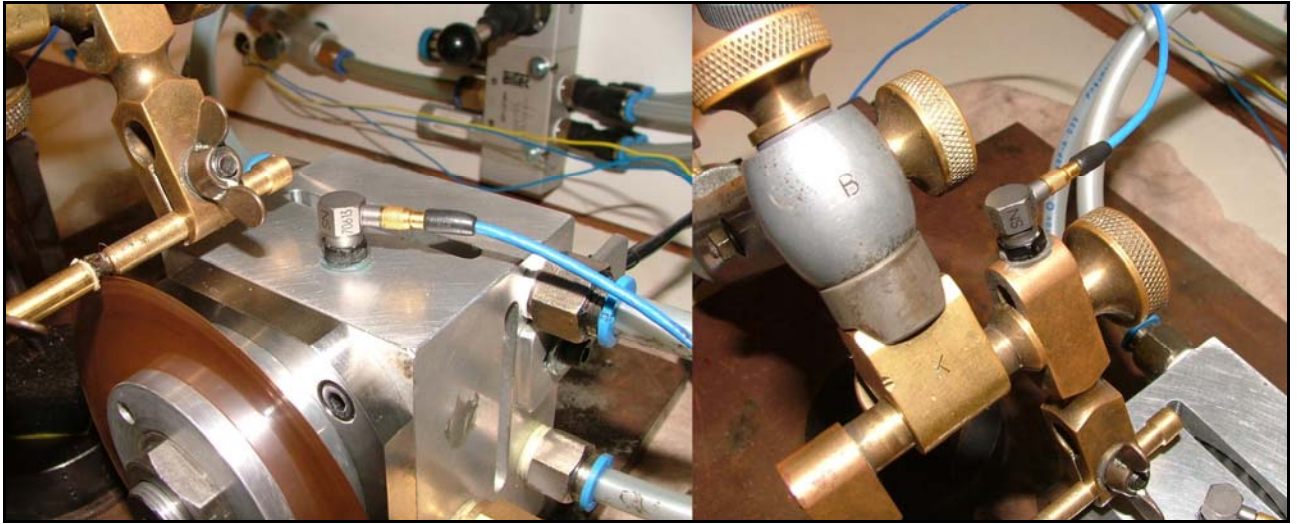


Figure 5.21: The accelerometer placement on the aerostatic machine.

The most significant reduction in vibration was seen in the housing of the aerostatic saw against the base of the conventional unit – the air film is thus superior to the graphite bearing in terms of vibration isolation. The average reduction is over 70%. In the case of the acceleration of the diamond clamp, the reduction is expected to be less, as the diamond is still in mechanical contact with the rotor and the drive. On average, the reduction in RMS acceleration is 50%.

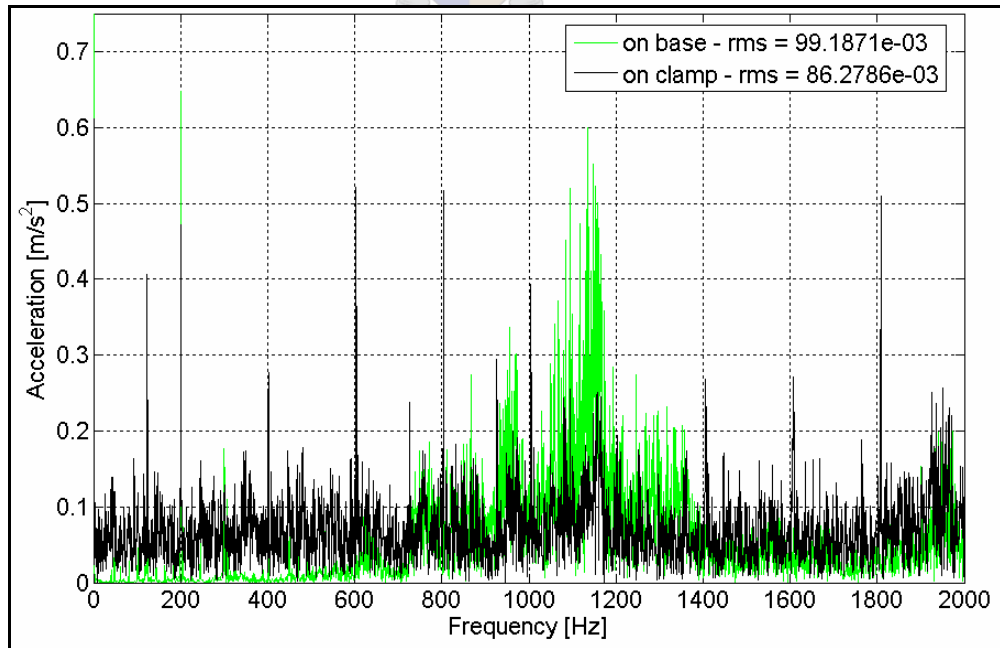


Figure 5.22: An FFT of the response for a sawing test on the conventional saw at 12 000 rpm.

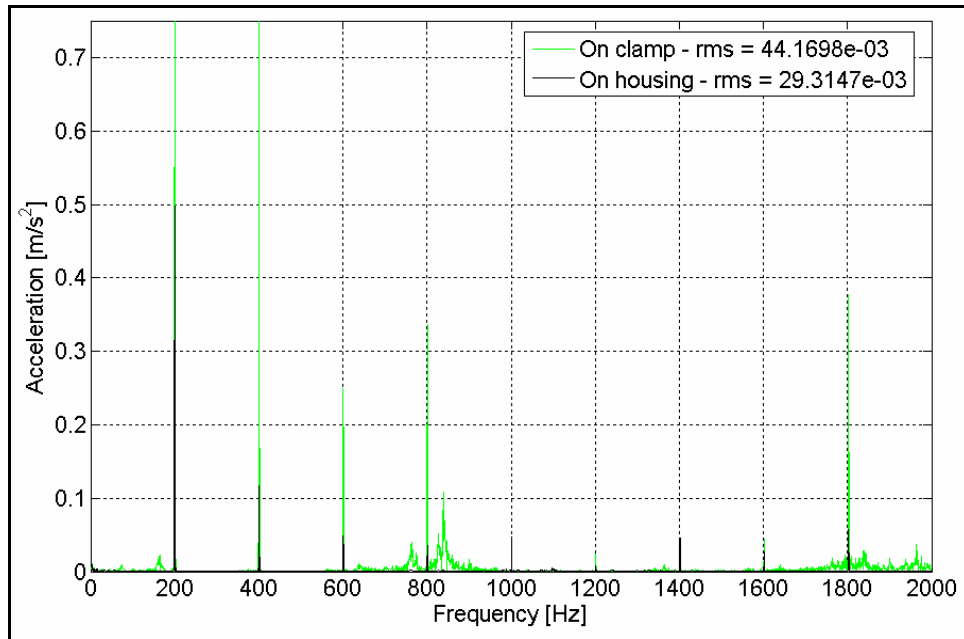


Figure 5.23: An FFT of the response for a sawing test on the aerostatic saw at 12 000 rpm.

Table 5.2: RMS vibration measurements taken during sawing tests (m/s^2)

Accelerometer position	Values for repeated tests	Machine	
		Conventional	Aerostatic, Design A
Clamp	Mean value	89.08×10^{-3}	44.55×10^{-3}
	Maximum value	164.79×10^{-3}	53.64×10^{-3}
	Minimum value	48.55×10^{-3}	36.99×10^{-3}
Housing/base	Mean value	101.53×10^{-3}	29.16×10^{-3}
	Maximum value	137.82×10^{-3}	30.87×10^{-3}
	Minimum value	85.57×10^{-3}	28.45×10^{-3}

The variation in RMS acceleration for the repeated tests with the aerostatic bearing is less compared to that of the conventional machine – maximum and minimum values were within 20% of the mean for the clamp and within 6% of the mean for the housing. In the case of the conventional machine, the variation around the mean was notably higher (50% for the clamp and 35% for the base). This is due to the fact that the v-blocks do not adequately support the spindle at high speeds and it tends to climb up the sides of the v-blocks. This results in a large variation in spindle position and vibration measurements, which are dependent on the normal sawing force. The aerostatic spindle with its superior rotor support and zero bearing contact eliminates these problems and the variation in vibration is much reduced.

5.7. Operational runs – housing vibration for motor and turbine drive

In order to make a comparison between the vibration levels of the Terry turbine and the DC motor, measurements were taken from the housing of Design B (y and z directions) during no-load operation for the two drives.

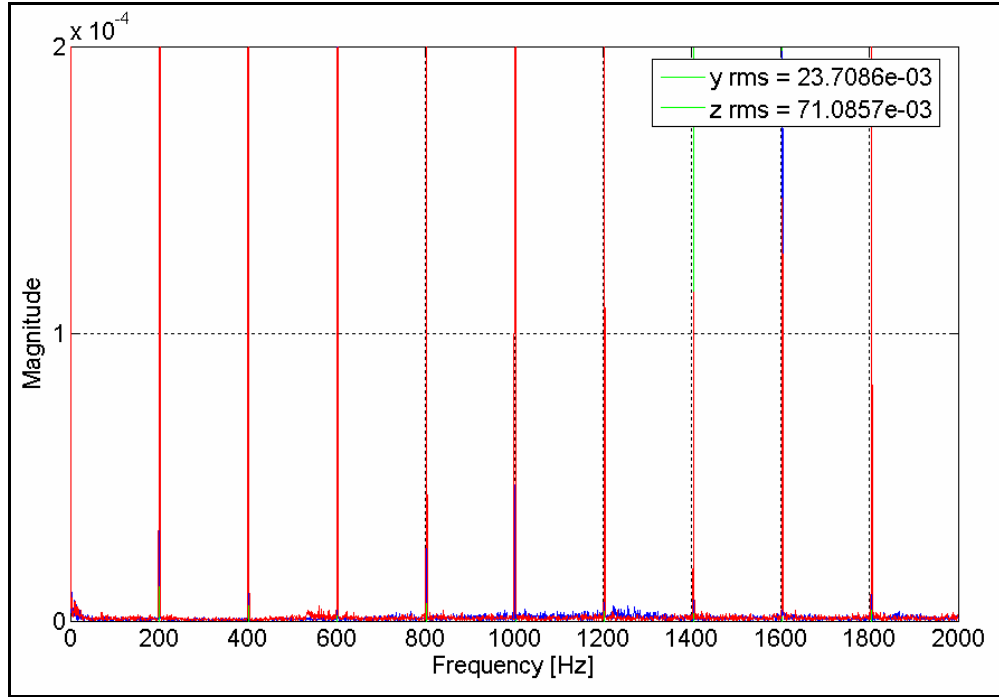


Figure 5.24: FFT taken on Design B housing at 12 000 rpm – turbine drive.

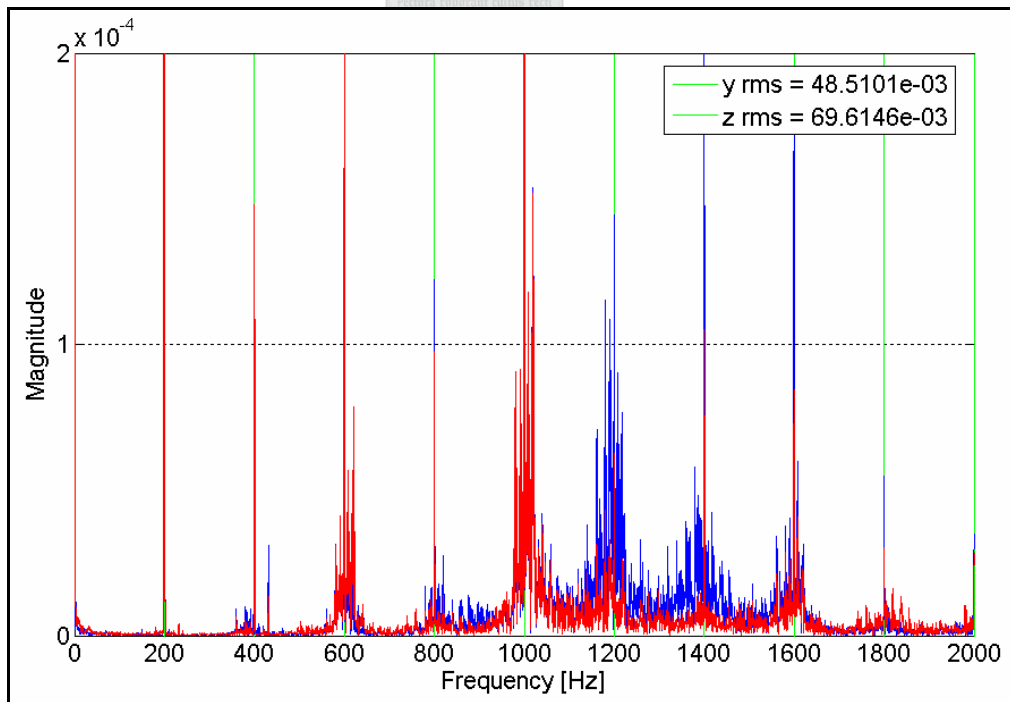


Figure 5.25: FFT taken on Design B housing at 12 000 rpm – motor drive.

There is no significant difference in the RMS acceleration values of the two drives, although from the plots the motor drive seems to introduce significantly higher vibration levels. Due to the direction of the turbine nozzles in the z direction, the vibration in that direction was always larger than that in the y direction. This is advantageous as the current orientation of the sawing arm makes the diamond more susceptible to vibration in the y direction. In addition the FFT with the turbine shows the synchronous peaks to be extremely dominant, but between these peaks the vibration is insignificant. Although the 1x peak is the largest, the following peaks could cause problems, as the risk of a natural system mode resonance is increased. (In order to present Figures 5.24 and 5.25 at the same scale, the initial peaks of the two figures could not be shown).

The results from the DC motor drive also show these synchronous peaks, but they do not dominate the plots as with the turbine. Rather there is increased activity in the region of 800 to 1600 Hz. Also modes seem to be present at 400 and 600 Hz (the latter of which can be seen with the turbine drive as well). The peak at approximately 432 Hz could be the axial mode. The fact that the vibration in the z direction is larger than the y was due to increased misalignment of the magnetic coupling in the z direction. While the motor plot seems to be the more severe of the two, the RMS values of the two drives are comparable – the turbine RMS value would be much reduced if not for the large synchronous peaks.

The Turbine was not powerful enough for operation of Design B at speeds exceeding 12 000 rpm – after this speed, acceleration was extremely slow (speeds approaching 18 500 rpm had been attained with the lighter Design A rotor). In this regard the more powerful DC motor had no trouble accelerating strongly past 14 000 rpm.

Chapter 6: Conclusions and Recommendations

The implementation of an aerostatic bearing in the diamond sawing machine was successful in reducing vibration at both the housing (by 70%) and the diamond clamp (by 50%), while at the same time making significantly higher spindle speeds possible – 18 500 rpm was achieved by Design A. In terms of the reduced vibration *and* increased speed requirements it was the most appropriate bearing type for the application. This chapter includes the concluded remarks on the project and provides further recommendations.

6.1. The FEM analysis, Euler rigid body model and EMA

FEM analysis was used to verify the validity of assuming the rotor to be rigid. EMA confirmed the theoretical results to within 6%. A rigid body model was developed using the modified Euler equations of motion in order to predict the natural frequencies of the rotor system as well as the amplitude of the rotor motion. The natural frequencies of the rotor's vibration modes can be calculated with sufficient accuracy by using SDOF vibration theory. This excludes the two angular vibration modes which, due to gyroscopic forces, are dependent on the rotor speed. This bifurcation is similar to that observed with the forwards and backwards whirling of flexible shafts. The EMA was successful in determining the experimental frequencies and damping of the rigid body modes. The frequencies of the natural modes were predicted reasonably accurately by the Euler model with the maximum error of 6%. The bearing stiffness (and thus mode frequency) was seen to be strongly dependent on the clearance. There was not sufficient theory available to gauge the accuracy of the damping results obtained. The results indicated that the damping coefficients were not strongly dependent on supply pressure, but because the frequency of the modes increased with pressure the damping ratios tended to decrease with increased pressure. The bearing clearance was seen to have a larger effect although this was not specifically studied.

The accuracy of the amplitude prediction was not as good as that of the frequencies. This was mainly due to the uncertainty in the radial damping of the bearing. The laser vibrometer test results indicated that the amplitude of the rotor motion was well within the clearance of the bearing, yet rotor contact was a serious,

persistent problem during test sessions. The maximum speed obtained by Design A was 18 500 rpm and 15 000 rpm for Design B. This is less than the desired speed of the machine and thus this aspect of the design requires further attention. No specific rotor modes were observed during vibration measurement of a running rotor, neither on the housing nor on the rotors, which is highly desirable in terms of reduced vibration. This could be due to the fact that the rotor could not be run at speeds that could excite these modes sufficiently.

6.2. An improved bearing and rotor design – Design C

Based on the comparison with the experimental results and the Euler model, an improved design, Design C, was completed - it is described in this section.

The use of a single, central journal bearing with two exhaust-fed thrust bearings on either end was a suitable design choice. It simplified manufacture and minimised air consumption while providing sufficient axial support of the rotor. It can be added that if a magnetic coupling is used, only a single thrust face would be required as the tension of the coupling would support the rotor axially. This would eliminate the extra components and extra set-up time concerned with an additional thrust face.

Design C would utilise a quarter-station design in order to increase the angular stiffness. For the same reason simple jets will be used, with the added advantage that they can be replaced if they become blocked. In order to solve the contact problems the angular stiffness of the new bearing has been increased by over 100%, mainly due to an increase in the journal dimensions and a reduction in the MRC. These specifications were achieved in spite of a reduced design pressure of 4 bar. The decrease in clearance was motivated by the following bearing design characteristics (Slocum, 1994; Wilcock, 1957; Stansfield, 1970):

$$Stiffness \propto \frac{1}{MRC}, \quad Damping \propto \frac{1}{MRC^3}, \quad Air\ consumption \propto MRC^3$$

Thus the MRC should be made as small as practically possible, while ensuring that the machinist responsible for the manufacture is able to finish the components to within the correct tolerance reliably. The frequency of angular vibration had to be at least 20% higher than the highest conceivable operating speed, which for Design C

has been set at 25 000 rpm (417 Hz). Thus the frequency of the angular mode needed to be more than 500 Hz. These stiffness specifications were designed at 4 bar to reduce air consumption, take advantage of the increased damping at the lower pressure and allow a margin of safety (i.e. an increase in supply pressure) in case the stiffness needs to be increased.

The best solution regarding material selection for the shaft is to use a hard-anodised aluminium rotor and to incorporate a safety control system which brings the rotor to rest if the supply pressure falls below a certain value. The reason for this is that a hardened steel shaft was not seen to be significantly better than the hard-anodised aluminium in terms of resistance to contact, and it was clearly inferior in terms of rotor mass which needs to be minimised. This route would result in the smallest and lightest rotor, which in turn would reduce manufacturing costs.

The use of stainless-steel and brass for the bearing-bush and feed jets respectively will be retained. The thrust faces will be hard-anodised aluminium to reduce weight. One thrust face will be integral with the shaft to eliminate the set up effort during assembly. Contrary to Design A, the integral face will be on the blade flange side, rather on the drive side, to improve the support of the blade and ensure its perpendicular requirement is as accurate as possible. The other thrust face needs to be secured to the shaft in such a way that it is not pulled skew from the axis when tightened. Using a threaded connection is not acceptable and a ball-and-socket or similar concept would be far better. The MAC has been increased to ease assembly. The reduction in axial stiffness will have no adverse effect on the rotor in the application but its effect on the axial vibration frequency was taken into account.

The specifications of the new bearing at 4 bar are as follows:

- Journal diameter, 30 mm
- Journal length, 60 mm
- Thrust bearing diameter, 60 mm
- Mean radial clearance, 15 μm
- Mean axial clearance, 30 μm
- Rotor mass, 350 g
- Polar moment of inertia, 100 $\text{kg}\cdot\text{m}^2$

- Transverse moment of inertia, 370 kg·m²
- Radial stiffness, 20 MN/m
- Angular stiffness, 4555 N·m/rad

The theoretical frequencies of the system modes estimated by the Euler model at 25 000 rpm are:

- Axial mode, 535 Hz
- Phi angular mode, 505 Hz
- Theta angular mode, 617.5 Hz
- Radial translation, 1207 Hz

With the vibration of the two drives being comparable, the decision of which one to use becomes more economical in nature. The current Terry turbine is not powerful enough for operation at the desired speeds and so the economic factors of a more powerful turbine versus the DC motor must be weighed up. It can be added that a radial inflow turbine of the required power output might be superior to the Terry turbine. The many synchronous peaks observed in the vibration data could be eliminated by the absence of the pockets in the radial turbine. If so, this turbine would achieve lower vibration than the DC motor and would be a better choice. However, the air consumption of the turbine would have to be compared with the cost of the DC motor controller and power supply before a decision can be made. The air consumption of the Terry-type turbine was in the region of 100 l/m at 14 000 rpm with zero load on the blade (driving the Design A rotor).

In order to increase the stability of the rotor at speed, two additional design routes may be visited. One would be the investigation of a porous compensated bush in place of the jet compensation. It is stated in the literature (New Way Precision, 2003) that porous compensation creates a more uniform pressure distribution along the journal length as well as increases the damping of the system. It is also more resistant to rotor contact (especially if a self-lubricating material such as sintered carbon is used) and has a lower Q value to improve the angular stiffness. If this route is investigated, a study of the permeability of the bushes would be required in order to achieve the correct compensation for the bearing.

The other design modifications which could be considered are aerodynamic aides as used in aerodynamic bearings. These normally take the form of grooves along each end of the journal and have been successfully applied to aerostatic bearings to improve their stability at high speeds. This type of modification would require thorough research in the field of fluid mechanics.

6.3. The design of the surrounding components

As the rotor was the main component in direct contact with the diamond, this project focussed specifically on the frequency of the rotor's vibration. The housing is isolated from the diamond by the air film and so would theoretically not be considered a problem. However, the diamond clamp is in contact with the housing via the sawing arm and the common base. Thus the following has to be considered:

- The frequencies of the housing modes were seen to be lower than the operating speed (Figure 6.1) and thus either the housing should be designed so that the frequencies are increased or an effective isolation technique has to be used to ensure that the diamond clamp is not affected by the housing vibration. As the housing vibration has been seen to transmit effectively through the air film, both solutions should be considered.
- The vibration modes of the sawing arm should be investigated and it is imperative that the arm is designed such that the frequency of the modes (the first bending mode especially) are higher than the operating speed.

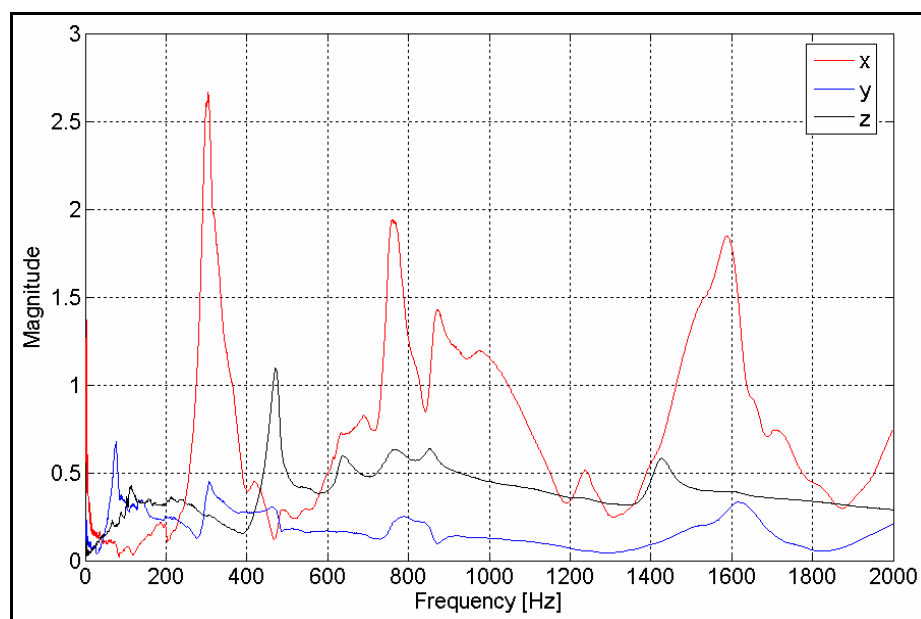


Figure 6.1: A transfer function for an impulse test on the bare housing of Design A.

6.4. The diamond sawing process

The current method of periodically lowering the diamond into the blade results in a small percentage of the total sawing time being used for effective sawing. Most of the time the diamond is not completely in contact with the blade and the risk of the feed being too heavy is always present. The reason for the use of this arrangement is that, with the very small normal feed force required (0.1 N to 0.5 N), a bearing of very low friction is required at the saw arm pivot. Any stiction (stick-slip condition) present in the bearing is detrimental to the control of the feed force and results in erratic variation in the force. With this in mind, a new concept is proposed whereby the correct feed force is applied during the entire sawing time. This would consist of a sawing arm similar to the one used in the current machine, with a translating mass that can be slid along its length. No threaded feeding rod would be used and the feed force would be dependent only on the centre of gravity of the arm, which itself depends on the position of the translating mass. The pivot point of the arm would incorporate a bearing of very low friction (ideally an aerostatic unit) to ensure that only the mass affects the feed force. The diamond would be lowered onto the rotating blade and left until the cut is complete. Using an aerostatic unit would also provide a measure of isolation against housing vibration.

6.5. Possible further investigation – EMA on rotating components

Additional investigation which would be extremely useful to the success of the project involves EMA on the rotor while it is operation. This would allow the examination of the frequencies and damping of the system modes as a function of the rotor speed (Bucher and Ewins, 2001).

The bifurcation of the angular modes could potentially be the cause of resonance problems as the frequency of the 'backwards' whirling mode would be lower than expected. Thus an investigation to confirm this phenomenon would be advantageous to the stability of the rotor.

The theory indicates that the damping of fluid film bearings is dependent on the velocity of the bearing surface. Thus it is dependent on rotor speed, and greater knowledge of the dependency would greatly improve the accuracy of the Euler model and allow a more efficient design of the bearing system.

References

A.G. Abulrub, P.S. Keogh, M.N. Sahinkaya, C.R. Burrows, 2005, *Effective Model reduction for Magnetically Levitated Flexible Rotor including Contact Dynamics*, Proceedings of IDETC/CIE 2005 (DETC2005-84418), ASME 2005 International Design Engineering Technical Conferences, and Computers and Information in Engineering Conference (Long Beach, USA)

B.M. Antkowiak, F.C. Nelson, undated, *Rotordynamic Modeling of an Actively Controlled Magnetic Bearing Gas Turbine Engine*, Based on the paper published in the *Proceedings of the 1997 International Gas Turbine and Aeroengine Congress and Exposition*, ASME

H. Baruh, 1999, *Analytical Dynamics*, McGraw-Hill International Editions, Mechanical Engineering Series

G.V. Brown, A.F. Fascak, R.H. Jansen, T.P. Dever, K.P. Duffy, January 2006, *Stabilizing Gyroscopic Modes in Magnetic-Bearing-Supported Flywheels by using Cross-Axis Proportional Gains*, National Aeronautics and Space Administration Glenn Research Centre, Prepared for the Guidance, Navigation and Control Conference and Exhibit

I. Bucher, D.J. Ewins, 2001, *Modal Analysis and Testing of Rotating Structures*, The Royal Society London A (2001) 359, 61-96

C. T. Crowe, D. F. Elger, J. A. Roberson, 2001, *Engineering Fluid Mechanics*, 7th Edition, John Wiley & Sons, Inc

M. S. Darlow, 1989, *Balancing of High-Speed Machinery*, Mechanical Engineering Series, Springer-Verlag, New York

M.I. Friswell, J.E.T. Penny, S.D. Garvey, A.W. Lees, 2001, *Damping Ratio and Natural Frequency Bifurcations in Rotating Systems*, Journal of Sound and Vibration (2001) 245(5), 960-967

N.S. Grassam, J.W. Powell, 1964, *Gas Lubricated Bearings*, Butterworth & Co', London

R.K. Harker, 1983, *Generalized Methods of Vibration Analysis*, University of Wisconsin, Madison, John Wiley & Sons Inc., New York

J.P. Hartog, *Mechanical Vibrations*, Massachusetts Institute of Technology, McGraw-Hill, New York, 1956

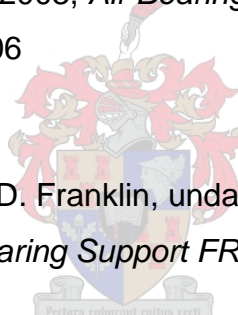
D. J. Inman, 2001, *Engineering Vibration*, 2nd Edition, Prentice Hall International

J.P. Khatait, W. Lin, W.J. Lin, 2005, *Design and Development of an Orifice-Type Aerostatic Thrust Bearing*, SIMTech technical reports, Volume 6, Number 1

New Way Precision Bearings, 2003, *Air Bearing Design and Application Guide*, Revision D, accessed July 2006

www.newwayairbearings.com

J.C. Nicholas, J.K. Whalen, S.D. Franklin, undated, *Improving Critical Speed Calculations using Flexible Bearing Support FRF Compliance Data*, Dresser-Rand Co.



J. Piers, D. Reynaerts, F. Verplaetsen, 2003, *A Micro-Turbine for Electric Power generation*, Journal of Sensors and Actuators A: Physical (Elsevier) 113 (2004) 86-93

J. Piers, D. Reynaerts, F. Verplaetsen, 2003, *Development of an axial microturbine for a portable gas turbine generator*, Journal of Micromechanics and Microengineering, 13 (2003) S190-S195

J. Piers, P. Vleugels, T. Waumans, M. Verlinden, D. Reynaerts, F. Verplaetsen, 2004, *Development of High-Speed Bearings for Micro Gas Turbines*, MicroMechanics Europe Workshop

E.S. Piekos, K.S. Breuer, 2000, *Manufacturing Effects in Microfabricated Gas Bearings: Axially Varying Clearance*, Journal of Tribology, Volume 124, October 2002

J.W. Powell, 1970, *Design of Aerostatic Bearings*, The Machinery Publishing Company Ltd., Brighton

N. Savoulides, K.S. Breuer, S.A. Jacobson, F.F. Ehrich, 2000, *Low Order Model for Very Short Hybrid Gas Bearings*, ASME, Tribology Division, Paper No. 2000-TRIB-12

A. H. Slocum, 1994, *Precision Machine Design, Topic 18: Externally Pressurised Bearings*

F.M. Stansfield, 1970, *Hydrostatic Bearings*, The Machinery Publishing Co' Ltd., Brighton

A. Surial, A. Kaushal, undated, *Dynamic Analysis of Flexible Turbo-Rotor Systems using Super-Elements*



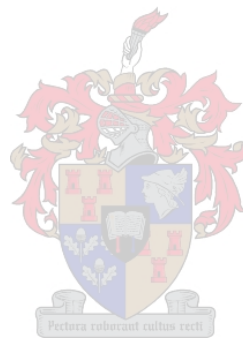
E. van Schalkwyk, 2006, *Design and Control of a High Speed Rotor of a Diamond Sawing Machine*, Faculty of Mechanical Engineering, Stellenbosch University

B. Watermeyer, 1982, *Diamond Cutting – 2nd Edition*, Centaur Publishers Johannesburg, South Africa

D.F. Wilcock, E.R. Booser, 1957, *Bearing Design and Application*, McGraw-Hill Series in Mechanical Engineering, New York

E. Wilks, J. Wilks, 1994, *Properties and Applications of Diamond* Butterworth-Heinemann Ltd., Oxford

C.W. Wong, X. Zhang, S.A. Jacobson, A.H. Epstein, 2002, *A Self-acting Thrust Bearing for High Speed Micro-rotors*, Journal of Microelectromechanical Systems
Volume 13, No. 2, April 2004



Bibliography

S. Zhou, J. Shi, 2001, *Active Balancing and Vibration Control of Rotating Machinery: A Survey*, The Shock and Vibration Digest, Volume 33, No. 4

A.D. Dimarogonas, S.A. Paipetis, 1983, *Analytical Methods in Rotor Dynamics*, Applied Science Publishers

Bently Pressurised Bearings, accessed June 2006
www.bentlypressurizedbearing.com

L. Meirovitch, 2001, *Fundamentals of Vibrations*, McGraw-Hill International Edition, Mechanical Engineering Series

R.J. Harker, 1983, *Generalized Methods of Vibration Analysis*, John Wiley & Sons Inc.

International Standard 20806, 2004, *Mechanical vibration – Criteria and safeguards for the in-situ balancing of medium and large rotors*, International Organization for Standardization (ISO)



V. Wowk, 1995, *Machinery Vibration: Balancing*, McGraw-Hill

P.P. Benham, R.J. Crawford, C.G. Armstrong, 1996, *Mechanics of Engineering Materials, 2nd Edition*, Prentice Hall

P.S. Heyns, 1998, *Mechanical Vibration – Measurement and Analysis*, University of Pretoria

H. Nakazawa, 1991, *Principles of Precision Engineering*, Oxford University Press

S. Zhou, J. Shi, undated, *Supervisory Adaptive Balancing of Rigid Rotors during Acceleration*, University of Michigan

M.F. Dimentberg, 2005, *Transverse Vibration of Rotating Shafts: Probability Density and First-Passage Time of Whirl Radius*, Journal of Non-linear Mechanics, 40 (2005) 1263-1267

O.E. Balje, 1981, *Turbomachines – A Guide to Design, Selection and Theory*, John Wiley & Sons Inc., New York

C.W. de Silva, 2005, *Vibration and Shock Handbook: Section I, Fundamentals and Analysis*, Chapter 3, *Modal Analysis*, Editor: C.W. de Silva, Taylor & Francis

C.W. de Silva, 2005, *Vibration and Shock Handbook: Section I, Fundamentals and Analysis*, Chapter 18, *Experimental Modal Analysis*, Editor: C.W. de Silva, Taylor & Francis

C.K. Mechefske, 2005, *Vibration and Shock Handbook: Section I, Fundamentals and Analysis*, Chapter 25, *Machine Condition Monitoring and Fault Diagnostics*, Editor: C.W. de Silver, Taylor & Francis

H.S. Samarasekera, 2005, *Vibration and Shock Handbook: Section VIII, Design and Applications*, Chapter 34, *Vibrations in Rotating Machinery*, Editor: C.W. de Silver, Taylor & Francis

M. Roseau, 1987, *Vibrations in Mechanical Systems – Analytical Methods and Applications*, University of Paris VI – Pierre et Marie Curie, Springer-Verlag Berlin Heidelberg

K. G. McConnell, 1995, *Vibration Testing – Theory and Practice*, Iowa State University of Science and Technology, John Wiley & Sons, Inc

Appendix A: Formula Derivation for the Rotor Modelling

A1. The model basis

The rotor is modelled as a cylinder rotating about its axis of symmetry with linear springs and dampers representing the air film. The springs and dampers exist on the centre journal section of the rotor as well as the two thrust faces. The motion of the rotor is defined using the following degrees of freedom (DOF):

- translation along the x axis (1st DOF)
- translation along the y axis (2nd DOF)
- translation along the z axis (3rd DOF)
- rotation about the x axis (free rigid body motion)
- rotation about the y axis (4th DOF)
- rotation about the z axis (5th DOF)

A 2-3-1 Euler transformation was chosen for this model, as the two rotation degrees of freedom occur around axis 2 and 3 (θ around y' and ϕ around z), with the free rigid-body rotation (at a spin velocity $\dot{\psi}$) occurring around axis 1, the x axis. This transformation sequence has a singularity at $\phi = 90^\circ$, which is acceptable, as the range of the angles ϕ and θ is much less than 90° . It is thus a superior transformation than a 3-1-3 and 3-2-3 sequence which have singularities at $\phi = 0^\circ$.

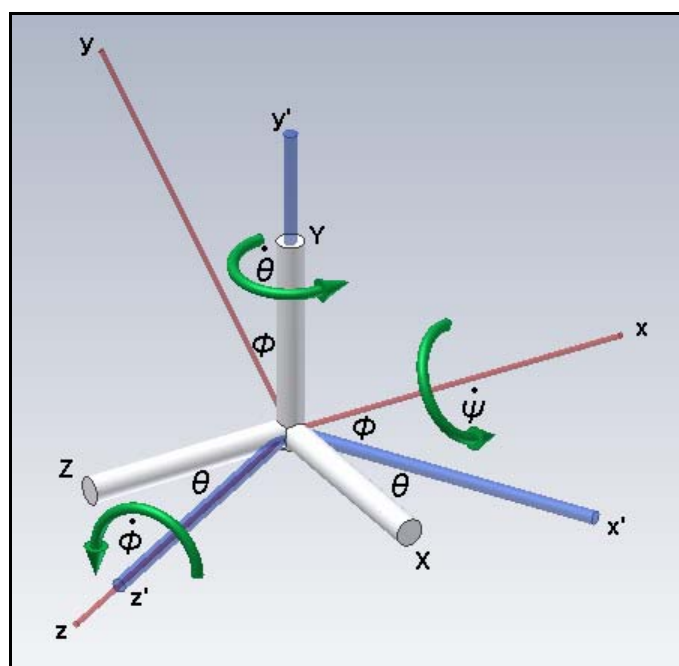


Figure A1: The Euler 2-3-1 transformation of the xyz axes.

The xyz axis system is termed the reference frame, and it is fixed to the rotor, undergoing the same displacements and rotations (except for the spin rotation) within the inertial frame XYZ – this is shown in Figure A2 below.

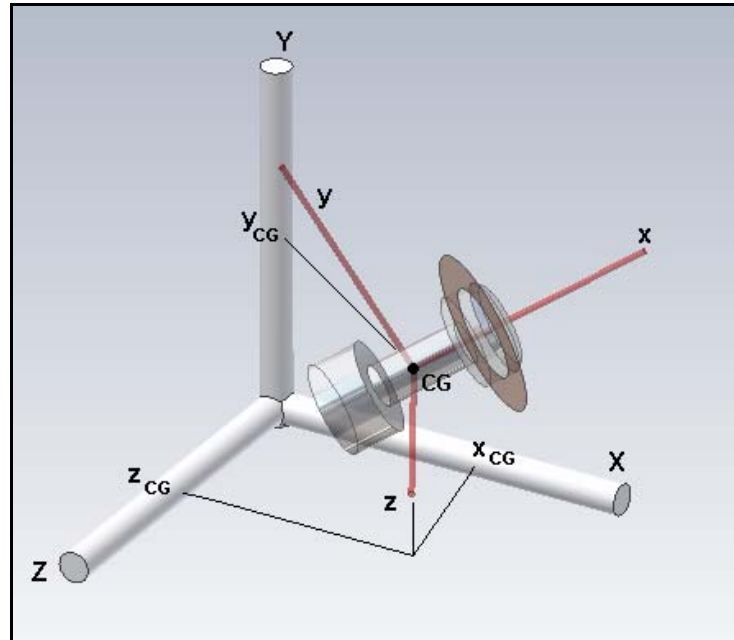


Figure A2: The rotor axis system xyz within the inertia axis system XYZ .

A2. The Euler modified equations of motion

Modified Euler equations of motion are used to define the rotor's motion as they are specifically suited to inertially symmetric (axisymmetric) bodies spinning around the symmetry axis with the external moments and forces independent of the spin angle.

A2.1. Transformation equations

Most of the forces are best described in the inertial system XYZ co-ordinates (I , J and K); however the modified Euler equations used to define the motion of the rotor are defined in terms of the reference frame co-ordinates (i , j and k). The forces therefore have to be transformed from the inertial to reference frame. In a similar manner, the translational and rotational velocities are calculated in terms of the reference frame co-ordinates and need to be transformed to the inertial frame so that the rotor displacement and orientation angles can be integrated successfully.

The transformation equations for the forces are:

$$\underline{I} = \cos \phi \cos \theta \underline{i} - \sin \phi \cos \theta \underline{j} + \sin \theta \underline{k} \quad (\text{A2.1a})$$

$$\underline{J} = \sin \phi \underline{i} + \cos \phi \underline{j} \quad (\text{A2.1b})$$

$$\underline{K} = -\sin \theta \cos \phi \underline{i} + \sin \theta \sin \phi \underline{j} + \cos \theta \underline{k} \quad (\text{A2.1c})$$

The transformation equations for the body velocities are:

$$\underline{i} = \cos \theta \cos \phi \underline{I} + \sin \phi \underline{J} - \sin \theta \cos \phi \underline{K} \quad (\text{A2.2a})$$

$$\underline{j} = -\cos \theta \sin \phi \underline{I} + \cos \phi \underline{J} + \sin \theta \sin \phi \underline{K} \quad (\text{A2.2b})$$

$$\underline{k} = \sin \theta \underline{I} + \cos \theta \underline{K} \quad (\text{A2.2c})$$

A2.2. The frame and body rotation velocities

The specific rotational velocities utilized in the Euler equations of motion are described as follows:

$$\text{Body spin rotational velocity, } {}^{F-B} \underline{\omega} = \dot{\psi} \underline{i} \quad (\text{A2.3})$$

$$\text{Frame rotational velocity, } {}^{A-F} \underline{\omega} = \dot{\phi} \underline{k} + \dot{\theta} \underline{j} \quad (\text{A2.4})$$

$$\text{Body rotational velocity, } {}^{A-B} \underline{\omega} = {}^{A-F} \underline{\omega} + {}^{F-B} \underline{\omega} \quad (\text{A2.5})$$

$${}^{A-B} \underline{\omega} = (\dot{\theta} \sin \phi + \dot{\psi}) \underline{i} + \dot{\theta} \cos \phi \underline{j} + \dot{\phi} \underline{k}$$

A2.3. Euler's modified rotational equations of motion

Euler's modified equation of rotational motion is defined as:

$$\{M_G\} = [I_G] \{\dot{\omega}\}_{rel} + [\tilde{\omega}_f] [I_G] \{\omega\} \quad (\text{A2.6})$$

$$\begin{Bmatrix} M_x \\ M_y \\ M_z \end{Bmatrix} = \begin{bmatrix} I_{xx} & 0 & 0 \\ 0 & I_{yy} & 0 \\ 0 & 0 & I_{zz} \end{bmatrix} \begin{Bmatrix} \dot{\omega}_1 \\ \dot{\omega}_2 \\ \dot{\omega}_3 \end{Bmatrix} + \begin{bmatrix} 0 & -\omega_{f3} & \omega_{f2} \\ \omega_{f3} & 0 & -\omega_{f1} \\ -\omega_{f2} & \omega_{f1} & 0 \end{bmatrix} \begin{bmatrix} I_{xx} & 0 & 0 \\ 0 & I_{yy} & 0 \\ 0 & 0 & I_{zz} \end{bmatrix} \begin{Bmatrix} \omega_1 \\ \omega_2 \\ \omega_3 \end{Bmatrix}$$

$$\begin{Bmatrix} M_x \\ M_y \\ M_z \end{Bmatrix} = \begin{Bmatrix} I_{xx} \dot{\omega}_1 - \omega_{f3} I_{yy} \omega_2 + \omega_{f2} I_{zz} \omega_3 \\ I_{yy} \dot{\omega}_2 + \omega_{f3} I_{xx} \omega_1 - \omega_{f1} I_{zz} \omega_3 \\ I_{zz} \dot{\omega}_3 - \omega_{f2} I_{xx} \omega_1 + \omega_{f1} I_{yy} \omega_2 \end{Bmatrix} \quad (\text{A2.7})$$

where the angular velocities for the reference frame and body are defined as

$$\text{Body 1: } \omega_1 = \dot{\theta} \sin \phi + \dot{\psi} \quad (\text{A2.8})$$

$$\text{Frame 1: } \omega_{f1} = \dot{\theta} \sin \phi = \omega_2 \tan \phi \quad (\text{A2.9})$$

$$\text{Body and frame 2: } \omega_2 = \omega_{f2} = \dot{\theta} \cos \phi \quad (\text{A2.10})$$

$$\text{Body and frame 3: } \omega_3 = \omega_{f3} = \dot{\phi} \quad (\text{A2.11})$$

Using Equations A2.9 to A2.11, Equation A2.7 can be rewritten in terms of the body angular velocities.

$$\begin{Bmatrix} M_x \\ M_y \\ M_z \end{Bmatrix} = \begin{Bmatrix} I_{xx} \dot{\omega}_1 - \omega_3 I_{yy} \omega_2 + \omega_2 I_{zz} \omega_3 \\ I_{yy} \dot{\omega}_2 + \omega_3 I_{xx} \omega_1 - \omega_2 \tan \phi I_{zz} \omega_3 \\ I_{zz} \dot{\omega}_3 - \omega_2 I_{xx} \omega_1 + \omega_2 \tan \phi I_{yy} \omega_2 \end{Bmatrix}$$

In this case $I_{yy} = I_{zz}$, so further simplifications is possible

$$\begin{Bmatrix} M_x \\ M_y \\ M_z \end{Bmatrix} = \begin{Bmatrix} I_{xx} \dot{\omega}_1 \\ I_{yy} \dot{\omega}_2 + \omega_3 (I_{xx} \omega_1 - \omega_2 \tan \phi I_{zz}) \\ I_{zz} \dot{\omega}_3 + \omega_2 (I_{yy} \omega_2 \tan \phi - I_{xx} \omega_1) \end{Bmatrix} \quad (\text{A2.12})$$

Substituting equations (A2.8) to (A2.11) into Equation A2.12 yields the equations of motion in terms of the Euler angles.

$$M_x = I_{xx} (\ddot{\psi} + \ddot{\theta} \sin \phi + \dot{\theta} \dot{\phi} \cos \phi) \quad (\text{A2.13})$$

$$M_y = I_{yy} (\ddot{\theta} \cos \phi - \dot{\theta} \dot{\phi} \sin \phi) + I_{xx} (\dot{\phi} \dot{\theta} \sin \phi + \dot{\phi} \dot{\psi}) - I_{zz} (\dot{\phi} \dot{\theta} \sin \phi) \quad (\text{A2.14})$$

$$M_z = I_{zz} (\ddot{\phi}) + I_{yy} (\dot{\theta}^2 \cos \phi \sin \phi) - I_{xx} (\dot{\theta}^2 \cos \phi \sin \phi + \dot{\theta} \dot{\psi} \cos \phi) \quad (\text{A2.15})$$

The range of the rotation angles θ and ϕ is required to ascertain whether further reduction of the above equations is possible. The maximum range of the two rotor angles is shown in Figure A3.

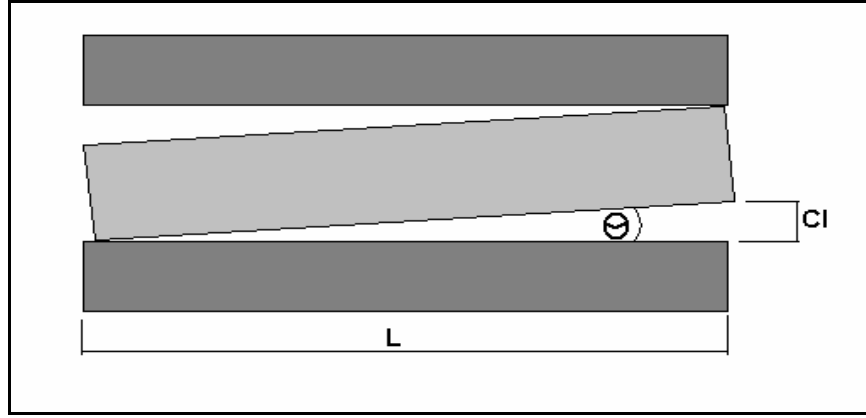


Figure A3: The maximum range of angles θ and Φ .

The maximum magnitude of the rotor angle is:

$$\theta_{\max} = \phi_{\max} = \tan^{-1}\left(\frac{cI}{L}\right)$$

$$\theta_{\max} = \phi_{\max} = \tan^{-1}\left(\frac{0.036}{45.00}\right)$$

$$\theta_{\max} = \phi_{\max} = 800.0 \times 10^{-6} \text{ radians}$$

$$\theta_{\max} = \phi_{\max} = 0.046^\circ$$

Due to the magnitude of the angles involved it is acceptable to use a small-angle assumption, that is:



$$\sin \theta \cong \theta$$

$$\cos \theta \cong 1$$

$$\tan \theta \cong \theta$$

(A2.16)

Thus the rotational equations of motion can be simplified to the following:

$$M_x = I_{xx} (\ddot{\psi} + \ddot{\theta}\phi + \dot{\theta}\dot{\phi}) \quad (\text{A2.17})$$

$$M_y = I_{yy} (\ddot{\theta} - \dot{\theta}\dot{\phi}) + I_{xx} (\dot{\phi}\dot{\theta}\phi + \dot{\phi}\dot{\psi}) - I_{zz} (\dot{\phi}\dot{\theta}\phi) \quad (\text{A2.18})$$

$$M_z = I_{zz} (\ddot{\phi}) + I_{yy} (\dot{\theta}^2\phi) - I_{xx} (\dot{\theta}^2\phi + \dot{\theta}\dot{\psi}) \quad (\text{A2.19})$$

A2.4. Euler's modified translational equations of motion

Euler's modified equation of translational motion is defined as:

$$\{F\} = \frac{d}{dt} \{Mv_G\} + [\tilde{\omega}_f] \{Mv_G\} \quad (\text{A2.20})$$

$$\begin{Bmatrix} F_x \\ F_y \\ F_z \end{Bmatrix} = \frac{d}{dt} \begin{Bmatrix} Mv_x \\ Mv_y \\ Mv_z \end{Bmatrix} + \begin{bmatrix} 0 & -\omega_{f3} & \omega_{f2} \\ \omega_{f3} & 0 & -\omega_{f1} \\ -\omega_{f2} & \omega_{f1} & 0 \end{bmatrix} \begin{Bmatrix} Mv_x \\ Mv_y \\ Mv_z \end{Bmatrix}$$

$$\begin{Bmatrix} F_x \\ F_y \\ F_z \end{Bmatrix} = \begin{Bmatrix} M\dot{v}_x - \omega_3 Mv_y + \omega_2 Mv_z \\ M\dot{v}_y + \omega_3 Mv_x - \omega_2 \tan \phi Mv_z \\ M\dot{v}_z - \omega_2 Mv_x + \omega_2 \tan \phi Mv_y \end{Bmatrix}$$

$$\begin{Bmatrix} F_x \\ F_y \\ F_z \end{Bmatrix} = \begin{Bmatrix} M\dot{v}_x - \dot{\phi} Mv_y + \dot{\theta} \cos \phi Mv_z \\ M\dot{v}_y + \dot{\phi} Mv_x - \dot{\theta} \sin \phi Mv_z \\ M\dot{v}_z - \dot{\theta} \cos \phi Mv_x + \dot{\theta} \sin \phi Mv_y \end{Bmatrix} \quad (\text{A2.21})$$

We now note that the translation equations will apply to the rotor mass less the imbalance mass, i.e. M is replaced by $M-m$, as the imbalance mass m is considered a separate body (Figure A4). Using the small angle assumption discussed above (Equation A2.16), the translation equations are further simplified:

$$F_x = (M - m) [\dot{v}_x - \dot{\phi} v_y + \dot{\theta} v_z] \quad (\text{A2.22})$$

$$F_y = (M - m) [\dot{v}_y + \dot{\phi} v_x - \dot{\theta} v_z] \quad (\text{A2.23})$$

$$F_z = (M - m) [\dot{v}_z - \dot{\theta} v_x + \dot{\theta} v_y] \quad (\text{A2.24})$$

The translation velocities, v_x , v_y and v_z denote the velocity of the centre of gravity of the rotor in terms of the reference frame co-ordinates, i , j and k .

A3. The forces applied to the rotor

The forces which are applied to the rotor are shown in Figure A4 below.

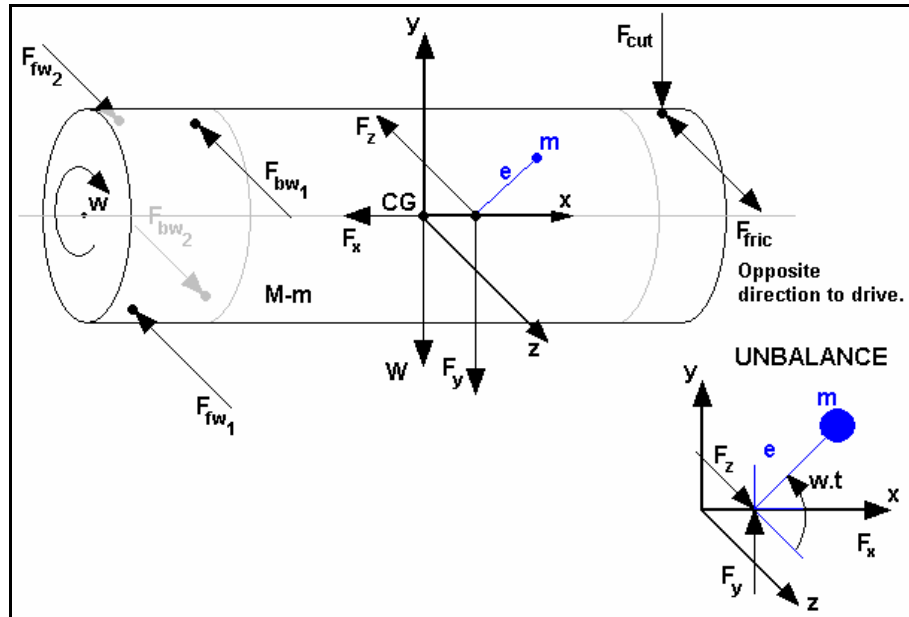


Figure A4: Forces applied to the rotor.

The forces applied to the rotor are as follows:

- Forces from the two turbine nozzles, F_{fw1} and F_{fw2} for clockwise rotor rotation (positive i) or F_{bw1} and F_{bw2} for counter clockwise rotation (negative i).
- Forces due to an imbalance present in the rotor, F_x , F_y and F_z .
- A normal cutting force on the blade, F_{cut} .
- A corresponding friction force, F_{fric} .
- The weight of the rotor, W .

A3.1. The turbine-drive forces

The force of the airflow on the turbine pockets from a single nozzle is defined as:

$$F_{turb} = E + B \sin(n \psi t) \quad (\text{N}) \quad (\text{A3.1})$$

It consists of a mean force E over which a small oscillation occurs with magnitude B . The oscillation is due to the presence of a finite number of turbine pockets, and its frequency is equal to the product of the number of pockets n (which is 30 in this particular case) and the rotor speed ψ . Because there are two nozzles present for each drive direction the nozzle forces should, in theory, be completely in balance. The resultant turbine force responsible for rotor translation should thus be zero.

However, in practice a small phase difference will be present between the two nozzles due to imperfect manufacture. The two turbine forces have been defined slightly out of phase (by angle α) with each other, while still oscillating at the same frequency.

$$\begin{aligned}\bar{F}_{fw1} &= -[E + B \sin(n\psi t)]\underline{K} \\ \bar{F}_{fw2} &= [E + B \sin(n\psi t + \alpha)]\underline{K}\end{aligned}\quad (\text{N}) \quad (\text{A3.2})$$

These two forces are illustrated below for arbitrary values of $E = 5$ and $B = 0.2$ N.

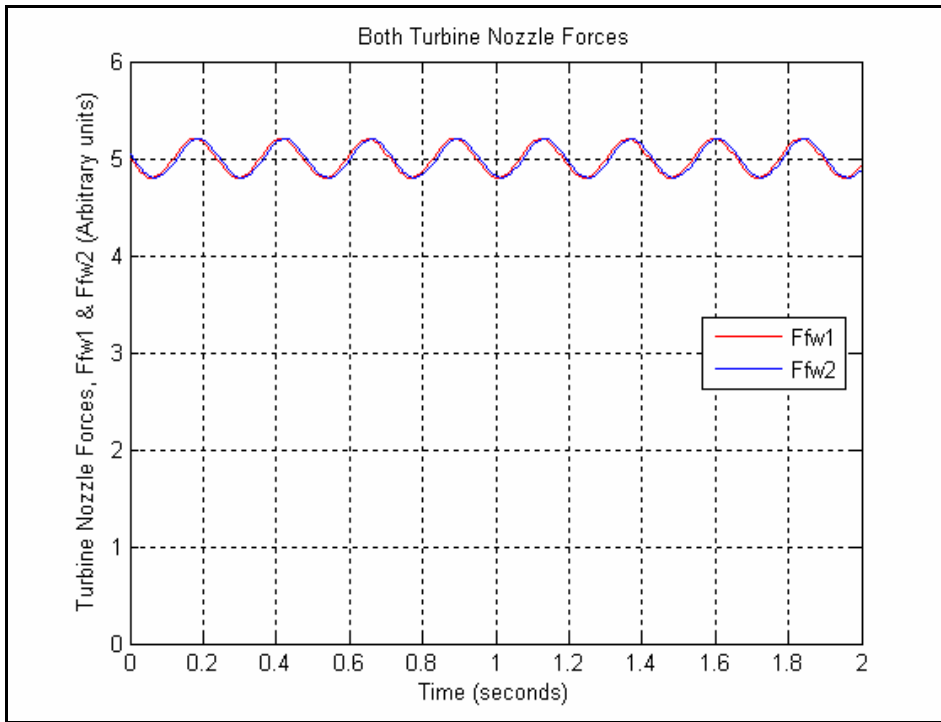


Figure A5: The two turbine nozzle forces and the phase difference between them.

The two forwards/clockwise nozzle forces are:

$$\begin{aligned}\bar{F}_{fw1} &= -[E + B \sin(n\psi t)]\underline{K} \\ \bar{F}_{fw1} &= [E + B \sin(n\psi t)]\left[\sin \theta \cos \phi_{\underline{i}} - \sin \theta \sin \phi_{\underline{j}} - \cos \theta \underline{k}\right]\end{aligned}$$

and

$$\begin{aligned}\bar{F}_{fw2} &= [E + B \sin(n\psi t + \alpha)]\underline{K} \\ \bar{F}_{fw2} &= -[E + B \sin(n\psi t + \alpha)]\left[\sin \theta \cos \phi_{\underline{i}} - \sin \theta \sin \phi_{\underline{j}} - \cos \theta \underline{k}\right]\end{aligned}$$

The resultant forward turbine nozzle force is thus:

$$\begin{aligned}\bar{F}_{fw} &= \bar{F}_{fw1} + \bar{F}_{fw2} \\ \bar{F}_{fw} &= B[\sin(n\psi t) - \sin(n\psi t + \alpha)] [\sin\theta \cos\phi_{\underline{i}} - \sin\theta \sin\phi_{\underline{j}} - \cos\theta \underline{k}]\end{aligned}\quad (\text{N}) \quad (\text{A3.3})$$

Thus as expected, the only effect on translational loading is due to the slight phase difference between the nozzles – this is shown in a sketch below.

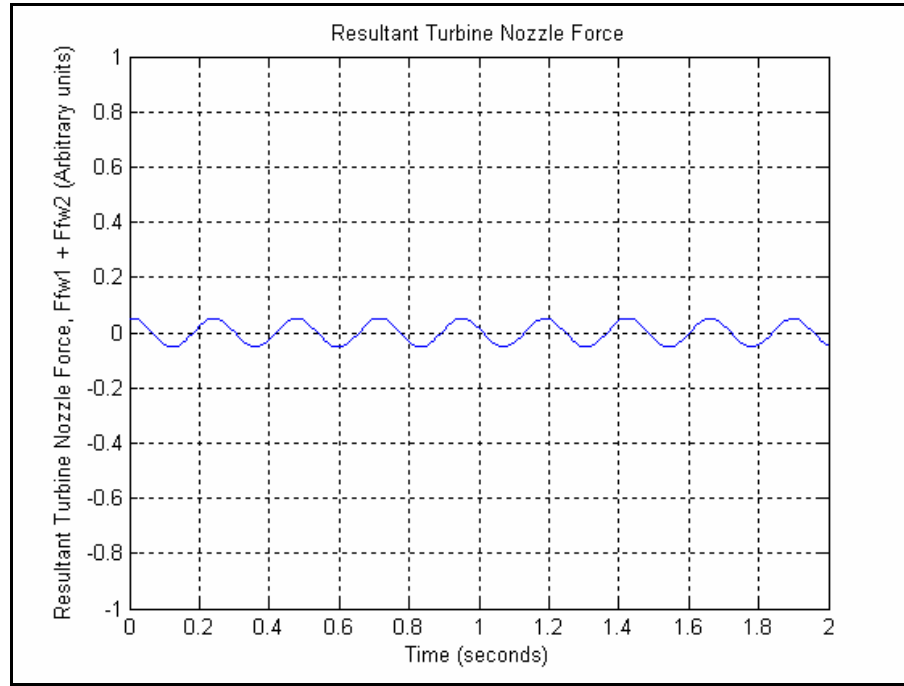


Figure A6: The resultant turbine nozzle force on the rotor.

A3.2. The normal cutting force on the blade

$$\begin{aligned}\bar{F}_{cut} &= -F_{cut} \underline{J} \\ \bar{F}_{cut} &= F_{cut} (-\sin\phi_{\underline{i}} - \cos\phi_{\underline{j}})\end{aligned}\quad (\text{N}) \quad (\text{A3.4})$$

A3.3. The friction force due to cutting

$$\begin{aligned}\bar{F}_{fric} &= -F_{fric} \underline{K} \\ \bar{F}_{fric} &= -F_{fric} [-\sin\theta \cos\phi_{\underline{i}} + \sin\theta \sin\phi_{\underline{j}} + \cos\theta \underline{k}]\end{aligned}\quad (\text{N}) \quad (\text{A3.5})$$

A3.4. The force components of the imbalance in the rotor

The imbalance forces applied to the imbalance mass m is calculated by calculating the acceleration of the imbalance mass.

$$\begin{aligned} \bar{F}_{unb} &= F_x \underline{i} + F_y \underline{j} + F_z \underline{k} \\ \bar{F}_{unb} &= m \bar{a}_{unb} \end{aligned} \quad (\text{N}) \quad (\text{A3.6})$$

where

$$\bar{a}_{unb} = \bar{a}_{xyz} + \bar{\alpha}_{xyz} \times \bar{r}_{unb} + \bar{\omega}_{xyz} \times (\bar{\omega}_{xyz} \times \bar{r}_{unb}) + 2\bar{\omega}_{xyz} \times \bar{\dot{r}}_{unb} + \bar{\ddot{r}}_{unb} \quad (\text{A3.7})$$

After elimination of negligible terms the imbalance force components are defined as

$$F_x = m(\dot{v}_x + \ddot{\theta}e \cos \psi t - \ddot{\phi}e \sin \psi t - 2\dot{\theta}\dot{\psi}e \sin \psi t - 2\dot{\phi}\dot{\psi}e \cos \psi t) \quad (\text{N}) \quad (\text{A3.8a})$$

$$F_y = m(\dot{v}_y + \ddot{\phi}a - e\dot{\psi}^2 \sin \psi t) \quad (\text{N}) \quad (\text{A3.8b})$$

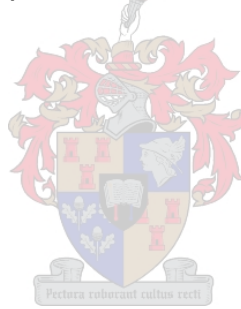
$$F_z = m(\dot{v}_z + \ddot{\theta}a - e\dot{\psi}^2 \cos \psi t) \quad (\text{N}) \quad (\text{A3.8c})$$

The forces due to imbalance applied to the rotor are defined as

$$\bar{F}_{unb} = -F_x \underline{i} - F_y \underline{j} - F_z \underline{k} \quad (\text{N}) \quad (\text{A3.9})$$

A3.5. The weight of the rotor

$$\begin{aligned} \bar{F}_w &= -W \underline{j} \\ \bar{F}_w &= -W \sin \phi \underline{i} - W \cos \phi \underline{j} \end{aligned} \quad (\text{N}) \quad (\text{A3.10})$$



A3.6. The forces due to the air stiffness

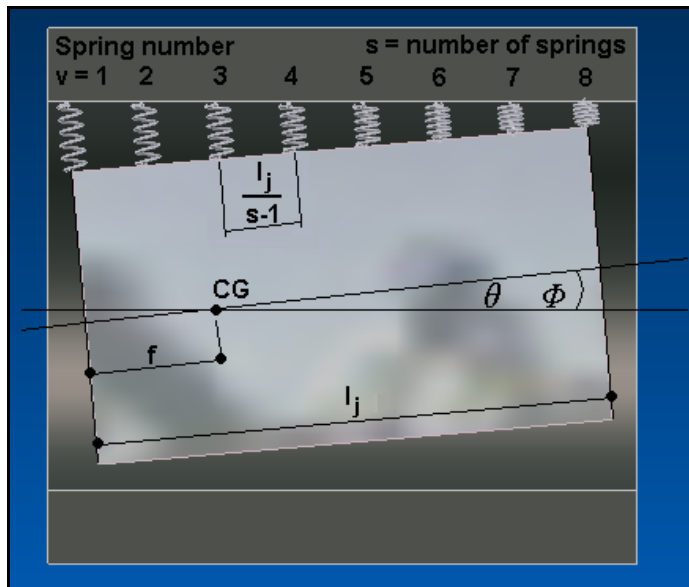


Figure A7: Sketch of representation of air stiffness using linear coil springs.

A3.6.1. Derivation of the spring stiffness distribution

The elongation of the v^{th} spring due to rotation θ or ϕ about the centre of gravity (CG) is:

$$\Delta = -\left[(v-1)\frac{l_j}{s-1} - f \right] \theta \quad (m) \quad (A3.11)$$

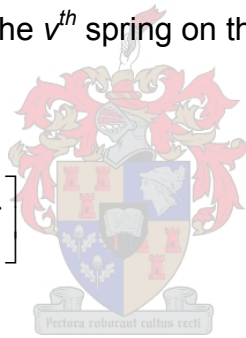
where

- s is the total number of springs representing the air stiffness.
- v is the number denoting a specific spring (i.e. $v = [1:s]$)
- l_j is the journal length
- f is the distance from the journal edge to the rotor's centre of gravity.
- The distance between springs is thus $l_j/(s-1)$.

Thus the springs on the left of the CG elongate (+ Δ) and the springs on the right of the CG shorten (- Δ) in response to a positive (counter clockwise) rotation of the rotor (ϕ or θ). The force applied by the v^{th} spring on the rotor due to rotation θ is:

$$F_v = K_v \Delta_v$$

$$F_v = -K_v \theta \left[(v-1)\frac{l_j}{s-1} - f \right] \quad (N) \quad (A3.12)$$



K_v is the stiffness of the v^{th} spring. The air film has been modelled in such a way that the spring stiffness constants decrease linearly from the centre of the bearing towards each end as a result of the pressure distribution in the bearing. This is shown in Figure A8 below. K_v is defined in Sections A3.6.2 and A3.6.3.

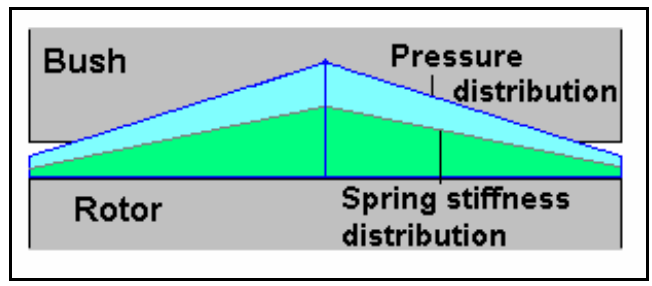


Figure A8: The pressure and spring stiffness distribution of the bearing model (New Way Precision Bearings).

A3.6.2. Even number of springs used for the model

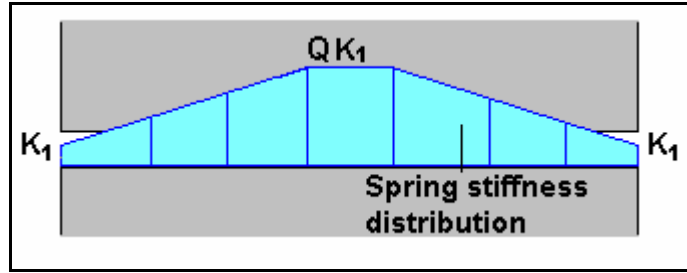



Figure A9: Pressure distribution in bearing model using an even number of springs.

The stiffness of the v^{th} spring is:

$$K_v = -\frac{K_1(Q-1)}{\frac{s}{2}-1} \left| v - \frac{s+1}{2} \right| + QK_1 + \frac{1}{2} K_1(Q-1) \quad (\text{N/m}) \quad (\text{A3.13})$$

where K_1 is the stiffness of the end springs and is defined as:

$$K_1 = \frac{\frac{1}{2} K_{rad}}{\sum_{v=1}^{\frac{s}{2}} \left[\frac{(v-1)(Q-1)}{\frac{s}{2}-1} + 1 \right]} \quad (\text{N/m}) \quad (\text{A3.14})$$


A3.6.3. Odd number of springs used for the model

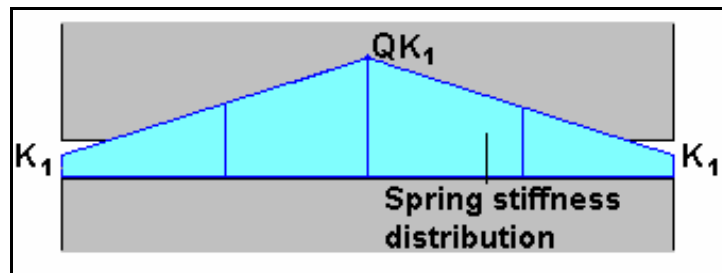


Figure A10: Pressure distribution in bearing model using an odd number of springs.

The stiffness of the v^{th} spring is:

$$K_v = -\frac{K_1(Q-1)}{\frac{s+1}{2}-1} \left| v - \frac{s+1}{2} \right| + QK_1 \quad (\text{N/m}) \quad (\text{A3.15})$$

where K_1 is defined as:

$$K_1 = \frac{K_{rad}}{2 \sum_{v=1}^{\frac{s+1}{2}-1} \left[\frac{(v-1)(Q-1)}{\frac{s+1}{2}-1} + 1 \right] + Q} \quad (\text{N/m}) \quad (\text{A3.16})$$

K_{rad} is the total radial stiffness of the bearing (i.e. $K_{rad} = \sum_{v=1}^s K_v$), and is estimated from the theory. Q is the ratio of the middle spring stiffness to that of the end spring.

A3.6.4. Spring forces due to translation y and rotation ϕ

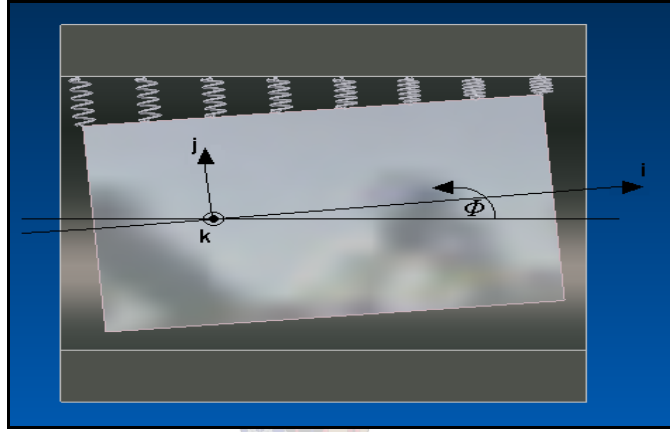


Figure A11: Spring deflections caused by translation y and rotation ϕ .

The spring force of v^{th} spring is:

$$\bar{F}_{v\phi} = -yK_v \underline{j} - \left[(v-1) \frac{l_j}{s-1} - f \right] \phi K_v \underline{j} \quad (\text{N}) \quad (\text{A3.17})$$

The total spring force as a result of all the springs is:

$$\begin{aligned} \bar{F}_{spr\phi} &= \sum_{v=1}^s \left\{ -K_v \left[y + \left((v-1) \frac{l_j}{s-1} - f \right) \phi \right] \right\} \underline{j} \\ \bar{F}_{spr\phi} &= -\sum_{v=1}^s K_v y \underline{j} - \sum_{v=1}^s K_v \left[(v-1) \frac{l_j}{s-1} - f \right] \phi \underline{j} \quad (\text{N}) \quad (\text{A3.18}) \\ \bar{F}_{spr\phi} &= \left\{ -y \sum_{v=1}^s K_v - \phi \sum_{v=1}^s K_v \left[(v-1) \frac{l_j}{s-1} - f \right] \right\} \underline{j} \\ \bar{F}_{spr\phi} &= \left\{ -yK_{rad} - \phi \Gamma \right\} \underline{j} \end{aligned}$$

where Γ is a term defined as:

$$\Gamma = \sum_{v=1}^s K_v \left[(v-1) \frac{l_j}{s-1} - f \right] \quad (\text{N/rad}) \quad (\text{A3.19})$$

This term defines the spring force per radian of rotation of the rotor. If the CG of the rotor lies precisely in the middle, rotation of the rotor causes no net spring force and this term is zero. For an even number of modelling springs, it is equal to:

$$\Gamma = \sum_{v=1}^s \left[-\frac{K_1(Q-1)}{\frac{s}{2}-1} \left| v - \frac{s+1}{2} \right| + QK_1 + \frac{\frac{1}{2}K_1(Q-1)}{\frac{s}{2}-1} \right] \left[(v-1) \frac{l_j}{s-1} - f \right] (\text{N}) \quad (\text{A3.20})$$

and for an odd number of springs, is equal to:

$$\Gamma = \sum_{v=1}^s \left[-\frac{K_1(Q-1)}{\frac{s+1}{2}-1} \left| v - \frac{s+1}{2} \right| + QK_1 \right] \left[(v-1) \frac{l_j}{s-1} - f \right] (\text{N}) \quad (\text{A3.21})$$

with K_1 defined in either Equation A3.14 or A3.16.

A3.6.5. Spring forces due to translation z and rotation θ

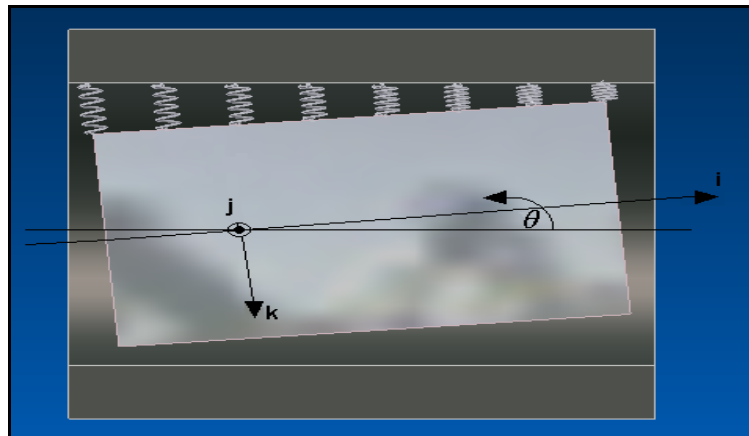


Figure A12: Spring deflections caused by translation z and rotation θ .

A rotation of θ around \underline{j} results in a rotation of $\theta \cdot \cos\Phi$ around \underline{j} . The individual spring force is defined as:

$$\bar{F}_{v\theta} = -zK_v \underline{k} + \left[(v-1) \frac{l_j}{s-1} - f \right] \theta \cdot \cos\phi K_v \underline{k} \quad (\text{N}) \quad (\text{A3.22})$$

The total spring force as a result of all the springs:

$$\begin{aligned}\bar{F}_{spr\theta} &= \sum_{v=1}^s \left\{ -K_v z + \left[\left((v-1) \frac{l_j}{s-1} - f \right) \theta \cdot \cos \phi \cdot K_v \right] \right\} k \\ \bar{F}_{spr\theta} &= -\sum_{v=1}^s K_v z k + \sum_{v=1}^s \left[(v-1) \frac{l_j}{s-1} - f \right] \theta \cdot \cos \phi \cdot K_v k \quad (\text{N}) \quad (\text{A3.23}) \\ \bar{F}_{spr\theta} &= \left\{ -z \sum_{v=1}^s K_v + \theta \cdot \cos \phi \cdot \sum_{v=1}^s K_v \left[(v-1) \frac{l_j}{s-1} - f \right] \right\} k \\ \bar{F}_{spr\theta} &= \left\{ -z K_{rad} + \theta \cdot \cos \phi \Gamma \right\} k\end{aligned}$$

A3.7. Spring stiffness - axial

The total axial spring force is:

$$\bar{F}_{ax} = -K_{ax} x i \quad (\text{N}) \quad (\text{A3.24})$$

A3.8. Damping forces

Unlike the spring stiffness, the damping coefficients used to model the damping of the air film is assumed to be constant along the journal length.

A3.8.1. Damping forces due to translational velocity \dot{y} and angular velocity $\dot{\phi}$

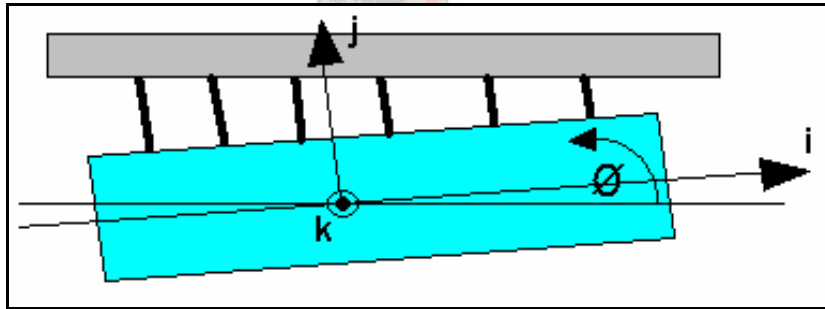


Figure A13: Forces due to translational velocity \dot{y} and angular velocity $\dot{\phi}$

The individual damping force is defined as:

$$\bar{F}_{d\phi} = -\dot{y} C_{damp} j - \left[(v-1) \frac{l_j}{s-1} - f \right] \dot{\phi} C_{damp} j \quad (\text{N}) \quad (\text{A3.25})$$

The total damping force as a result of all the dampers:

$$\begin{aligned}\bar{F}_{damp\phi} &= \sum_{v=1}^s \left\{ -C_{damp} \left[\dot{y} + \left((v-1) \frac{l_j}{s-1} - f \right) \dot{\phi} \right] \right\} \underline{j} \\ \bar{F}_{damp\phi} &= -\sum_{v=1}^s C_{damp} \dot{y} \underline{j} - \sum_{v=1}^s C_{damp} \left[(v-1) \frac{l_j}{s-1} - f \right] \dot{\phi} \underline{j} \quad (\text{N}) \quad (\text{A3.26}) \\ \bar{F}_{damp\phi} &= \left\{ -C_{rad} \dot{y} - C_{damp} \dot{\phi} \sum_{v=1}^s \left[(v-1) \frac{l_j}{s-1} - f \right] \right\} \underline{j} \\ \bar{F}_{damp\phi} &= \left\{ -C_{rad} \dot{y} - C_{damp} \dot{\phi} \Sigma \right\} \underline{j}\end{aligned}$$

where

$$C_{rad} = C_{damp} \times s \quad (\text{Ns/m}) \quad (\text{A3.27})$$

and Σ is a term defined as:

$$\Sigma = \sum_{v=1}^s \left[(v-1) \frac{l_j}{s-1} - f \right] \quad (\text{m}) \quad (\text{A3.28})$$

This term defines the component of the radial damping force due to rotation of the rotor.

A3.8.2. Damping forces due to translational velocity \dot{z} and angular velocity $\dot{\theta}$

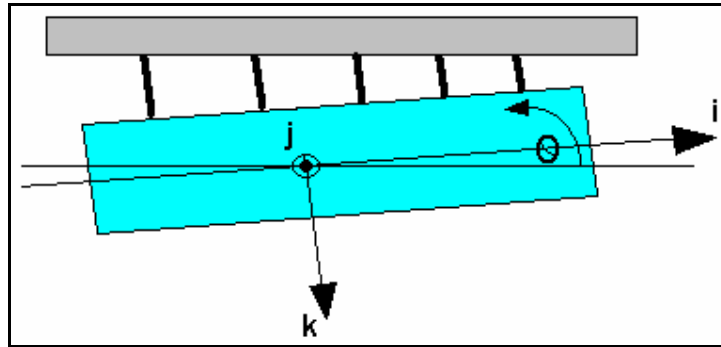


Figure A14: Forces due to translational velocity \dot{z} and angular velocity $\dot{\theta}$

A rotation of θ around \underline{j} results in a rotation of $\theta \cdot \cos\phi$ around \underline{i} . The individual damping force is defined as:

$$\bar{F}_{d\theta} = -\dot{z} C_{damp} \underline{k} + \left[(v-1) \frac{l_j}{s-1} - f \right] (\dot{\theta} \cos\phi - \dot{\phi} \theta \sin\phi) C_{damp} \underline{k} \quad (\text{N}) \quad (\text{A3.29})$$

The total damper force as a result of all the dampers is:

$$\begin{aligned}\bar{F}_{damp\theta} &= \sum_{v=1}^s \left\{ -C_{damp} \dot{z} + \left[\left((v-1) \frac{l_j}{s-1} - f \right) (\dot{\theta} \cos \phi - \dot{\phi} \theta \sin \phi) C_{damp} \right] \right\} \underline{k} \\ \bar{F}_{damp\theta} &= -\sum_{v=1}^s C_{damp} \dot{z} \underline{k} + \sum_{v=1}^s \left[(v-1) \frac{l_j}{s-1} - f \right] (\dot{\theta} \cos \phi - \dot{\phi} \theta \sin \phi) C_{damp} \underline{k} \\ \bar{F}_{damp\theta} &= \left\{ -C_{rad} \dot{z} + C_{damp} (\dot{\theta} \cos \phi - \dot{\phi} \theta \sin \phi) \sum_{v=1}^s \left[(v-1) \frac{l_j}{s-1} - f \right] \right\} \underline{k} \\ \bar{F}_{damp\theta} &= \left\{ -C_{rad} \dot{z} + C_{damp} (\dot{\theta} \cos \phi - \dot{\phi} \theta \sin \phi) \Sigma \right\} \underline{k}\end{aligned}\tag{N} \tag{A3.30}$$

A3.9. Damping forces - axial

The total axial damping force is:

$$\bar{F}_{dampax} = -C_{ax} \dot{x} \underline{i} \tag{N} \tag{A3.31}$$

A3.10. Translation of rotor (mass $M-m$):

Applying the forces to the translational equations of motion (Equation A2.22 to A2.24), and assuming small angles, yields:

$$\begin{aligned}\Sigma F(\underline{i}) : & -K_{ax} x - C_{ax} \dot{x} + B[\sin(n\psi t) - \sin(n\psi t + \alpha)]\theta + F_{fric} \theta - F_{cut} \phi - W\phi \\ & - m(\ddot{\theta} e \cos \psi t - \ddot{\phi} e \sin \psi t - 2\dot{\theta} \dot{\psi} e \sin \psi t - 2\dot{\phi} \dot{\psi} e \cos \psi t) = M\dot{v}_x + (M-m)(\dot{\phi} v_y + \dot{\theta} v_z)\end{aligned}\tag{N} \tag{A3.32}$$

$$\begin{aligned}\Sigma F(\underline{j}) : & -K_{rad} y - \phi \Gamma - C_{rad} \dot{y} - C_{damp} \dot{\phi} \Sigma - B[\sin(n\psi t) - \sin(n\psi t + \alpha)]\theta \phi \\ & - F_{fric} \theta \phi - F_{cut} - W - m(\ddot{\phi} a - e \dot{\psi}^2 \sin \psi t) = M\dot{v}_y + (M-m)(\dot{\phi} v_x - \dot{\theta} \phi v_z)\end{aligned}\tag{N} \tag{A3.33}$$

$$\begin{aligned}\Sigma F(\underline{k}) : & -K_{rad} z + \theta \Gamma - C_{rad} \dot{z} + C_{damp} (\dot{\theta} - \dot{\phi} \theta) \Sigma - B[\sin(n\psi t) - \sin(n\psi t + \alpha)] \\ & - F_{fric} - m(\ddot{\theta} a - e \dot{\psi}^2 \cos \psi t) = M\dot{v}_z + (M-m)(-\dot{\theta} v_x + \dot{\theta} \phi v_y)\end{aligned}\tag{N} \tag{A3.34}$$

A4. The moments applied to the rotor

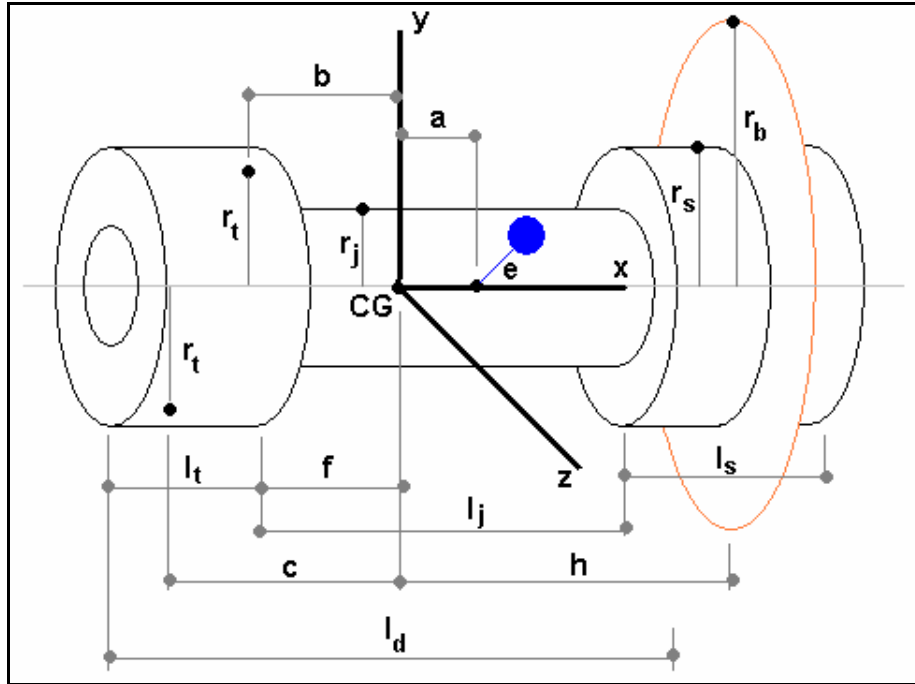


Figure A15: Applicable dimensions of the rotor.

The dimensions applicable to the forces on the rotor are as follows:

- The turbine radius, r_t (the position of the respective nozzles)
- The bearing journal radius, r_j .
- The blade radius, r_b .
- The flange and thrust face radius, r_s .
- The distance from the centre of gravity to the position of the imbalance, a .
- The radial distance from the imbalance mass to the rotor axis, e .
- The distance from the CG to the respective turbine nozzles, b and c .
- The distance from the CG to the blade, h .
- The distance from the CG to the turbine face, f .
- The length of the turbine, l_t .
- The length of the journal, l_j .
- The combined length of the two flanges, l_s .

A4.1. Moment due to turbine drive

Moment arms for the two forwards direction (clockwise) nozzles are:

$$\begin{aligned} \bar{r}_{fw1} &= -c\bar{i} - r_t\bar{j} \\ \bar{r}_{fw2} &= -c\bar{i} + r_t\bar{j} \end{aligned} \quad (m) \quad (A4.1)$$

Resulting moment:

$$\begin{aligned}\bar{T}_{fw} &= \bar{r}_{fw1} \times \bar{F}_{fw1} + \bar{r}_{fw2} \times \bar{F}_{fw2} \\ \bar{T}_{fw} &= [-c\underline{i} - r_t \underline{j}] \times [E + B \sin(n\omega t)] [\sin \theta \cos \phi \underline{i} - \sin \theta \sin \phi \underline{j} - \cos \theta \underline{k}] \\ &+ [-c\underline{i} + r_t \underline{j}] \times [-E + B \sin(n\omega t + \alpha)] [\sin \theta \cos \phi \underline{i} - \sin \theta \sin \phi \underline{j} - \cos \theta \underline{k}]\end{aligned}$$

$$\begin{aligned}\bar{T}_{fw} &= c[E + B \sin(n\omega t)] \sin \theta \sin \phi \underline{k} - c[E + B \sin(n\omega t)] \cos \theta \underline{j} \\ &+ r_t [E + B \sin(n\omega t)] \sin \theta \cos \phi \underline{k} + r_t [E + B \sin(n\omega t)] \cos \theta \underline{i} \\ &- c[E + B \sin(n\omega t + \alpha)] \sin \theta \sin \phi \underline{k} + c[E + B \sin(n\omega t + \alpha)] \cos \theta \underline{j} \\ &+ r_t [E + B \sin(n\omega t + \alpha)] \sin \theta \cos \phi \underline{k} + r_t [E + B \sin(n\omega t + \alpha)] \cos \theta \underline{i}\end{aligned}$$

$$\begin{aligned}\bar{T}_{fw} &= \{r_t [2E + B(\sin(n\omega t) + \sin(n\omega t + \alpha))]\cos \theta\} \underline{i} \\ &+ \{c[B(\sin(n\omega t + \alpha) - \sin(n\omega t))]\cos \theta\} \underline{j} \\ &+ \{c[B(\sin(n\omega t) - \sin(n\omega t + \alpha))]\sin \theta \sin \phi + r_t [2E + B(\sin(n\omega t) + \sin(n\omega t + \alpha))]\sin \theta \cos \phi\} \underline{k}\end{aligned}$$

(N·m) (A4.2)

A4.2. Moment due to cutting force

Moment arm:

$$\bar{r}_{cut} = h\underline{i} + r_b \underline{j} \quad (\text{m}) \quad (\text{A4.3})$$

Resulting moment:

$$\begin{aligned}\bar{T}_{cut} &= \bar{r}_{cut} \times \bar{F}_{cut} \\ \bar{T}_{cut} &= [h\underline{i} + r_b \underline{j}] \times F_{cut} [-\sin \phi \underline{i} - \cos \phi \underline{j}] \\ \bar{T}_{cut} &= -hF_{cut} \cos \phi \underline{k} + r_b F_{cut} \sin \phi \underline{k} \\ \bar{T}_{cut} &= [r_b F_{cut} \sin \phi - hF_{cut} \cos \phi] \underline{k}\end{aligned}$$

(N·m) (A4.4)

A4.3. Moment due to frictional force

Moment arm:

$$\bar{r}_{fric} = h\underline{i} + r_b \underline{j} \quad (\text{m}) \quad (\text{A4.5})$$

Resulting moment for forwards (clockwise) direction:

$$\begin{aligned}
 \bar{T}_{fric} &= \bar{r}_{fric} \times \bar{F}_{fric} \\
 \bar{T}_{fric} &= [h\underline{i} + r_b\underline{j}] \times F_{fric} [\sin \theta \cos \phi \underline{i} - \sin \theta \sin \phi \underline{j} - \cos \theta \underline{k}] \\
 \bar{T}_{fric} &= -hF_{fric} \sin \theta \sin \phi \underline{k} + hF_{fric} \cos \theta \underline{j} - r_b F_{fric} \sin \theta \cos \phi \underline{k} - r_b F_{fric} \cos \theta \underline{i} \\
 \bar{T}_{fric} &= -r_b F_{fric} \cos \theta \underline{i} + hF_{fric} \cos \theta \underline{j} + (-hF_{fric} \sin \theta \sin \phi - r_b F_{fric} \sin \theta \cos \phi) \underline{k}
 \end{aligned}$$

(N·m) (A4.6)

A4.4. Moment due to rotor imbalance

Moment arm:

$$\bar{r}_{unb} = a\underline{i} + e \sin \psi t \underline{j} + e \cos \psi t \underline{k}$$

(m) (A4.7)

Resulting moment:

$$\begin{aligned}
 \bar{T}_{unb} &= \bar{r}_{unb} \times \bar{F}_{unb} \\
 \bar{T}_{unb} &= (a\underline{i} + e \sin \psi t \underline{j} + e \cos \psi t \underline{k}) \times (-F_x \underline{i} - F_y \underline{j} - F_z \underline{k}) \\
 \bar{T}_{unb} &= (F_y e \cos \psi t - F_z e \sin \psi t) \underline{i} + (aF_z - F_x e \cos \psi t) \underline{j} + (F_x e \sin \psi t - aF_y) \underline{k}
 \end{aligned}$$

(N·m) (A4.8)

where the imbalance forces F_x , F_y and F_z are defined in Equations A3.8a to A3.8c. Thus Equation A4.8 is rewritten more completely as:

$$\begin{aligned}
 \bar{T}_{unb} &= (m(\dot{v}_y + \ddot{\phi}a - e\dot{\psi}^2 \sin \psi t) e \cos \psi t - m(\dot{v}_z + \ddot{\theta}a - e\dot{\psi}^2 \cos \psi t) e \sin \psi t) \underline{i} \\
 &+ (am(\dot{v}_z + \ddot{\theta}a - e\dot{\psi}^2 \cos \psi t) - m(\dot{v}_x + \ddot{\theta}e \cos \psi t - \ddot{\phi}e \sin \psi t - 2\dot{\theta}\dot{\psi}e \sin \psi t - 2\dot{\phi}\dot{\psi}e \cos \psi t) e \cos \psi t) \underline{j} \\
 &+ (m(\dot{v}_x + \ddot{\theta}e \cos \psi t - \ddot{\phi}e \sin \psi t - 2\dot{\theta}\dot{\psi}e \sin \psi t - 2\dot{\phi}\dot{\psi}e \cos \psi t) e \sin \psi t - am(\dot{v}_y + \ddot{\phi}a - e\dot{\psi}^2 \sin \psi t)) \underline{k}
 \end{aligned}$$

(N·m) (A4.9)

A4.5. Moments due to spring forces

A4.5.1 Moment due to translation y and rotation ϕ

Moment arm:

$$\bar{r}_\phi = \left[(v-1) \frac{l_j}{s-1} - f \right] \underline{i} + r_j \underline{j}$$

(m) (A4.10)

Resulting moment of all the springs:

$$\begin{aligned}
 \bar{T}_{spr\phi} &= \sum_{v=1}^s [\bar{r}_{\phi} \times \bar{F}_{v\phi}] \\
 \bar{T}_{spr\phi} &= \sum_{v=1}^s \left\{ \left[(v-1) \frac{l_j}{s-1} - f \right] \underline{i} + r_j \underline{j} \right\} \times \left\{ -yK_v - \phi K_v \left[(v-1) \frac{l_j}{s-1} - f \right] \right\} \underline{j} \\
 \bar{T}_{spr\phi} &= \sum_{v=1}^s \left[(v-1) \frac{l_j}{s-1} - f \right] \left[-K_v \left(y + \phi \left((v-1) \frac{l_j}{s-1} - f \right) \right) \right] \underline{k} \\
 \bar{T}_{spr\phi} &= -\sum_{v=1}^s yK_v \left[(v-1) \frac{l_j}{s-1} - f \right] \underline{k} - \sum_{v=1}^s \phi K_v \left[(v-1) \frac{l_j}{s-1} - f \right]^2 \underline{k} \\
 \bar{T}_{spr\phi} &= \left[-y\Gamma - \phi K_{ang} \right] \underline{k}
 \end{aligned}
 \tag{N·m} \tag{A4.11}$$

The function Γ has been defined in Equation A3.19 – in this instance it defines the component of the moment due to rotor translation. If the rotor's centre of gravity falls in the middle of the journal, translation has no effect on spring torque and this term is zero. The angular stiffness, K_{ang} , is defined as:

$$K_{ang} = \sum_{v=1}^s K_v \left[(v-1) \frac{l_j}{s-1} - f \right]^2 \tag{N·m/rad} \tag{A4.12}$$

Thus the angular stiffness is proportional to the radial stiffness and to the square of the journal length, as described in the literature (Powell, 1970). It is also seen to be dependent on the position of the CG.

A4.5.2. Moment due to translation z and rotation θ

Moment arm:

$$\bar{r}_{\theta} = \left[(v-1) \frac{l_j}{s-1} - f \right] \underline{i} - r_j \underline{k} \tag{m} \tag{A4.13}$$

Resulting moment of all the springs:

$$\begin{aligned}\bar{T}_{spr\theta} &= \sum_{v=1}^s [\bar{r}_\theta \times \bar{F}_{v\theta}] \\ \bar{T}_{spr\theta} &= \sum_{v=1}^s \left\{ \left[(v-1) \frac{l_j}{s-1} - f \right] \underline{i} - r_j \underline{k} \right\} \times \left\{ -K_v z + \theta \cos \phi K_v \left[(v-1) \frac{l_j}{s-1} - f \right] \right\} \underline{k} \\ \bar{T}_{spr\theta} &= -\sum_{v=1}^s \left\{ -K_v z \left[(v-1) \frac{l_j}{s-1} - f \right] + \left[(v-1) \frac{l_j}{s-1} - f \right]^2 \theta \cos \phi K_v \right\} \underline{j} \\ \bar{T}_{spr\theta} &= \sum_{v=1}^s K_v z \left[(v-1) \frac{l_j}{s-1} - f \right] \underline{j} - \sum_{v=1}^s \left[(v-1) \frac{l_j}{s-1} - f \right]^2 \theta \cos \phi K_v \underline{j} \\ \bar{T}_{spr\theta} &= [z\Gamma - \theta \cos \phi K_{ang}] \underline{j}\end{aligned}\tag{N·m} \tag{A4.14}$$

A4.6. Moments due to damping forces

A4.6.1. Moment due to translational velocity \dot{y} and angular velocity $\dot{\phi}$

Moment arm:

$$\bar{r}_\phi = \left[(v-1) \frac{l_j}{s-1} - f \right] \underline{i} + r_j \underline{j}\tag{m} \tag{A4.15}$$

Resulting moment:

$$\begin{aligned}\bar{T}_{damp\phi} &= \sum_{v=1}^s [\bar{r}_\phi \times \bar{F}_{d\phi}] \\ \bar{T}_{damp\phi} &= \sum_{v=1}^s \left\{ \left[(v-1) \frac{l_j}{s-1} - f \right] \underline{i} + r_j \underline{j} \right\} \times \left\{ -\dot{y} C_{damp} - \dot{\phi} C_{damp} \left[(v-1) \frac{l_j}{s-1} - f \right] \right\} \underline{j} \\ \bar{T}_{damp\phi} &= \sum_{v=1}^s \left[(v-1) \frac{l_j}{s-1} - f \right] \left[-\dot{y} C_{damp} - \dot{\phi} C_{damp} \left((v-1) \frac{l_j}{s-1} - f \right) \right] \underline{k} \\ \bar{T}_{damp\phi} &= -\sum_{v=1}^s \left[(v-1) \frac{l_j}{s-1} - f \right] \dot{y} C_{damp} \underline{k} - \sum_{v=1}^s \dot{\phi} C_{damp spr} \left[(v-1) \frac{l_j}{s-1} - f \right]^2 \underline{k} \\ \bar{T}_{damp\phi} &= [-\dot{y} C_{damp} \Sigma - \dot{\phi} C_{damp} \Sigma \Sigma] \underline{k}\end{aligned}\tag{N·m} \tag{A4.16}$$

The function $\Sigma\Sigma$, is defined as:

$$\Sigma\Sigma = \sum_{v=1}^s \left[(v-1) \frac{l_j}{s-1} - f \right]^2\tag{m^2} \tag{A4.17}$$

This term relates the total radial coefficient to the angular damping coefficient.

A4.6.2. Moment due to translational velocity \dot{z} and angular velocity $\dot{\theta}$

Moment arm:

$$\bar{r}_\theta = \left[(v-1) \frac{l_j}{s-1} - f \right] \underline{i} - r_j \underline{k} \quad (\text{m}) \quad (\text{A4.18})$$

Resulting moment of all the springs:

$$\begin{aligned} \bar{T}_{damp\theta} &= \sum_{v=1}^s \left[\bar{r}_\theta \times \bar{F}_{d\theta} \right] \\ \bar{T}_{damp\theta} &= \sum_{v=1}^s \left\{ \left[(v-1) \frac{l_j}{s-1} - f \right] \underline{i} - r_j \underline{k} \right\} \times \left\{ -C_{damp} \dot{z} + (\dot{\theta} \cos \phi - \dot{\phi} \theta \sin \phi) C_{damp} \left[(v-1) \frac{l_j}{s-1} - f \right] \right\} \underline{k} \\ \bar{T}_{damp\theta} &= -\sum_{v=1}^s \left\{ \left[(v-1) \frac{l_j}{s-1} - f \right] \left[-C_{damp} \dot{z} + \left((v-1) \frac{l_j}{s-1} - f \right) (\dot{\theta} \cos \phi - \dot{\phi} \theta \sin \phi) C_{damp} \right] \right\} \underline{j} \\ \bar{T}_{damp\theta} &= \sum_{v=1}^s C_{damp} \dot{z} \left[(v-1) \frac{l_j}{s-1} - f \right] \underline{j} - \sum_{v=1}^s \left[(v-1) \frac{l_j}{s-1} - f \right]^2 (\dot{\theta} \cos \phi - \dot{\phi} \theta \sin \phi) C_{damp} \underline{j} \\ \bar{T}_{damp\theta} &= \left[C_{damp} \dot{z} \Sigma - (\dot{\theta} \cos \phi - \dot{\phi} \theta \sin \phi) C_{damp} \Sigma \Sigma \right] \underline{j} \end{aligned} \quad (\text{N}\cdot\text{m}) \quad (\text{A4.19})$$

A4.7. Rotation of the rotor

Substituting the above moment definitions into the rotational equations of motion (Equations A2.17 to A2.19) yields a complete set of equations. For the case of moments around the x axis:

$$\begin{aligned} \Sigma M(\underline{i}): r_t [2E + B(\sin(n\omega t) + \sin(n\omega t + \alpha))] \cos \theta - r_b F_{fric} \cos \theta + m(\dot{v}_y + \ddot{\phi} a - e \dot{\psi}^2 \sin \psi t) e \cos \psi t \\ - m(\dot{v}_z + \ddot{\theta} a - e \dot{\psi}^2 \cos \psi t) e \sin \psi t = I_{xx} (\ddot{\psi} + \ddot{\theta} \phi + \dot{\theta} \dot{\phi}) \end{aligned} \quad (\text{N}\cdot\text{m}) \quad (\text{A4.20})$$

As this analysis pertains to a rotor at constant speed ($\dot{\psi}_{\text{mean}} = 0$), the frictional moment should equal the moment due to the mean turbine nozzle forces:

$$\begin{aligned} F_{fric} r_b \cos \theta &= 2E r_t \cos \theta \\ F_{fric} &= 2E \frac{r_t}{r_b} \end{aligned} \quad (\text{N}\cdot\text{m}) \quad (\text{A4.21})$$

As so, assuming small angles, Equation A4.23 can be rewritten as:

$$\begin{aligned} \Sigma M(\underline{i}): r_i [B(\sin(n\omega t) + \sin(n\omega t + \alpha))] + m(\dot{v}_y + \ddot{\phi}a - e\dot{\psi}^2 \sin\psi t)e \cos\psi t \\ - m(\dot{v}_z + \ddot{\theta}a - e\dot{\psi}^2 \cos\psi t)e \sin\psi t = I_{xx}(\ddot{\psi} + \ddot{\theta}\phi + \dot{\theta}\dot{\phi}) \end{aligned} \quad (\text{N}\cdot\text{m}) \quad (\text{A4.22})$$

which in itself means that any variation in rotor speed $\dot{\psi}$ will be due to the oscillation of the turbine nozzle forces. In addition, it is noted that:

$$F_{fric} = \mu F_{cut} \quad (\text{N}) \quad (\text{A4.23})$$

with μ representing the dynamic coefficient of friction between the blade and the diamond - thus moment summations around the j and z axes are as follows:

$$\begin{aligned} \Sigma M(\underline{j}): z\Gamma - \theta K_{ang} + \dot{z}C_{damp}\Sigma - (\dot{\theta} - \dot{\phi}\theta\phi)C_{damp}\Sigma\Sigma + cB[\sin(n\omega t + \alpha) - \sin(n\omega t)] \\ + h\mu F_{cut} + am(\dot{v}_z - e\dot{\psi}^2 \cos\psi t) - m(\dot{v}_x - \ddot{\phi}e \sin\psi t - 2\dot{\theta}\dot{\psi}e \sin\psi t - 2\dot{\phi}\dot{\psi}e \cos\psi t)e \cos\psi t \\ = (I_{yy} - a^2m + e^2m \cos^2\psi t)\ddot{\theta} - I_{yy}(\dot{\theta}\dot{\phi}\phi) + I_{xx}(\dot{\phi}\dot{\theta}\phi + \dot{\phi}\dot{\psi}) - I_{zz}(\dot{\phi}\dot{\theta}\phi) \end{aligned} \quad (\text{N}\cdot\text{m}) \quad (\text{A4.24})$$

$$\begin{aligned} \Sigma M(\underline{k}): -y\Gamma - \phi K_{ang} - \dot{y}C_{damp}\Sigma - \dot{\phi}C_{damp}\Sigma\Sigma + cB[\sin(n\psi t) - \sin(n\psi t + \alpha)]\theta\phi \\ + r_i[2E + B(\sin(n\psi t) + \sin(n\psi t + \alpha))]\theta + r_b F_{cut}\phi - hF_{cut} - h\mu F_{cut}\theta\phi \\ - r_b\mu F_{cut}\theta + m(\dot{v}_x + \ddot{\theta}.e \cos\psi t - 2\dot{\theta}\dot{\psi}.e \sin\psi t - 2\dot{\phi}\dot{\psi}.e \cos\psi t)e \sin\psi t \\ - am(\dot{v}_y - e\dot{\psi}^2 \sin\psi t) = \ddot{\phi}(I_{zz} + e^2m \sin^2\psi t + a^2m) + I_{yy}(\dot{\theta}^2\phi) - I_{xx}(\dot{\theta}^2\phi + \dot{\theta}\dot{\psi}) \end{aligned} \quad (\text{N}\cdot\text{m}) \quad (\text{A4.25})$$

Equations A3.32 to A3.34 as well as A4.22, A4.24 and A4.25 form the basis for the MATLAB Simulink model used to predict the rotor's dynamic characteristics. As the forces depend on the rotational motion and the moments are dependent on the motion of the centre of gravity, a separate solution of the above equations of motion is not possible.

Appendix B: Aerostatic Bearing Design Calculations

This appendix contains the design procedure for the aerostatic bearing. All of the equations stated below were sourced from the book by J. W. Powell, *Design of Aerostatic Bearings*, either from the text or from plotted graphs (in which case the equations were obtained by fitting curves to the available graphs).

B1. The input parameters

The following parameters are specified at the start of the design:

1. Journal diameter, D
2. Journal length, l_j
3. The larger radius of the thrust face, r_s
4. The mean radial clearance in the journal bearing, MRC
5. The mean axial clearance in the thrust bearing, MAC
6. The supply pressure, P_o
7. An estimated value for the journal exhaust pressure, P_{d2}
8. Atmospheric pressure at thrust exhaust, P_a
9. The jet type, i.e. either *annular* or *simple*
10. The jet position, i.e. either quarter-station ($j=0.25l_j$) or half-station ($j=0.5l_j$)
11. The number of jets per row, u
12. The intended gauge pressure ratio of journal section, K_{go}
13. The mean gas temperature, T
14. The gas specific heat ratio, γ
15. The gas constant, R

B2. The approximate load capacities from bearing dimensions

$$\text{For } D = 25.4 \text{ mm, } W^* = \frac{l_j^3}{2679.25} - \frac{l_j^2}{9.477} + 9.688l_j - 72.06 \quad (\text{N}) \quad (\text{B1})$$

$$\text{For } D = 50.8 \text{ mm, } W^* = -\frac{l_j^2}{14.504} + 15.271l_j - 136.12 \quad (\text{N}) \quad (\text{B2})$$

$$\text{For } D = 76.2 \text{ mm, } W^* = -\frac{l_j^2}{29.008} + 18.038l_j - 213.52 \quad (\text{N}) \quad (\text{B3})$$

$$\text{For } D = 101.6 \text{ mm, } W^* = \frac{l_j^2}{19.338} + 9.546l_j + 180.15 \quad (\text{N}) \quad (\text{B4})$$

$$\text{For } D = 127 \text{ mm, } W^* = \frac{l_j^2}{14.504} + 7.882l_j + 556.03 \quad (\text{N}) \quad (\text{B5})$$

The length is given in millimetres and the load capacity in Newtons. For bearing of which the diameter falls between the above set points, linear interpolation is used to obtain the approximate load capacity. The above load capacities apply to a bearing using simple jets at quarter stations and it must be noted that the use of annular jets can reduce the load capacity by as much as 30% (Powell, 1970). Half-station bearings can reduce the load capacity by as much as 50% on bearings with large l_j/D ratios (see Section B6). The above load capacities correspond to a supply pressure of 6.8 bar gauge and the following correction is required for other supply pressures:

$$W = W^* \times \frac{P_o - P_{d2}}{6.8} \quad (\text{N}) \quad (\text{B6})$$

where the supply and journal exhaust pressures are expressed in bars.

B3. The approximate bearing flow rate

The approximate gas flow rate for a journal bearing is:

$$fr^* = \frac{9.628D}{l_j} \quad (\text{//min}) \quad (\text{B7})$$

The following corrections factors apply to the flow rate:

$$\text{For pressure, } k_1 = 0.0433(P_o - P_{d2})^2 - 0.144(P_o - P_{d2}) + 0.26 \quad (\text{B8})$$

where the supply and journal exhaust pressures are expressed in bars.

$$\text{For the MRC (mm), } k_2 = \left(\frac{\text{MRC}}{0.0127} \right)^3 \quad (\text{B9})$$

$$\text{For the gauge pressure ratio, } k_3 = 3.661K_{go}^2 + 0.9793K_{go} + 0.0214 \quad (\text{B10})$$

The corrected flow rate is then

$$fr = fr^* \times k_1 \times k_2 \times k_3 \quad (\text{//min}) \quad (\text{B11})$$

If half-station jets are used, the flow rate is effectively halved:

$$fr_{half} = \frac{fr}{2} \quad (\text{//min}) \quad (\text{B12})$$

The above equations are used solely in the initial stages of the bearing design to gain some insight into the approximate bearing size required for the application.

B4. The simple jet size from the MRC

$$K_{go}=0.4, \quad d^* = 162.972MRC^2 + 5.0506MRC - 0.0046 \quad (\text{mm}) \quad (\text{B13})$$

$$K_{go}=0.6, \quad d^* = 283.872MRC^2 + 6.6182MRC - 0.0043 \quad (\text{mm}) \quad (\text{B14})$$

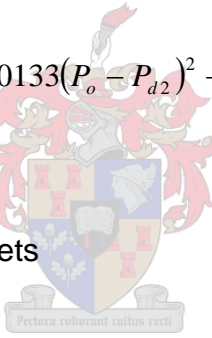
$$K_{go}=0.8, \quad d^* = 425.16MRC^2 + 9.4218MRC - 0.0027 \quad (\text{mm}) \quad (\text{B15})$$

where the MRC is in millimetres. For other gauge pressure ratios, linear interpolation is used. The following correction factors apply to the jet diameter:

$$\text{For the supply pressure, } k_4 = -0.0133(P_o - P_{d2})^2 + 0.1847(P_o - P_{d2}) + 0.5314 \quad (\text{B16})$$

$$\text{For the number of jets, } k_5 = \sqrt{\frac{8}{u}}, \quad (\text{B17})$$

where u is the number of jets



$$\text{For the } l/D \text{ ratio, } k_6 = \sqrt{\frac{D}{l_j}} \quad (\text{B18})$$

$$\text{For the station position, } j/l_j, \quad k_7 = \sqrt{\frac{l_j}{4j}} \quad (\text{B19})$$

For the exhaust pressure ratio,

$$k_8 = -56.932 \left(\frac{P_{d2} + 1}{P_o + 1} \right)^5 + 156.78 \left(\frac{P_{d2} + 1}{P_o + 1} \right)^4 - 163.77 \left(\frac{P_{d2} + 1}{P_o + 1} \right)^3 + 80.629 \left(\frac{P_{d2} + 1}{P_o + 1} \right)^2 - 19.485 \left(\frac{P_{d2} + 1}{P_o + 1} \right) + 2.7696$$

(B20)

where the supply and exhaust pressures are gauge pressures expressed in bars.

The correct jet diameter is thus:

$$d = d^* \times k_4 \times k_5 \times k_6 \times k_7 \times k_8 \quad (\text{mm}) \quad (\text{B21})$$

B5. The annular jet size from the MRC

$$K_{go}=0.4, \quad d^* = 62705.6MRC^3 - 1421.28MRC^2 + 17.8352MRC - 0.0114 \quad (\text{mm}) \quad (\text{B22})$$

$$K_{go}=0.6, \quad d^* = 1859.48MRC^2 - 0.1096MRC - 0.0025 \quad (\text{mm}) \quad (\text{B23})$$

$$K_{go}=0.8, \quad d^* = 4038.8MRC^2 - 3.13MRC + 0.0066 \quad (\text{mm}) \quad (\text{B24})$$

For other gauge pressure ratios, linear interpolation is used. The following correction factors apply to the jet diameter:

$$\text{For the supply pressure, } k_4 = -0.0197(P_o - P_{d2})^2 + 0.323(P_o - P_{d2}) + 0.1546 \quad (\text{B25})$$

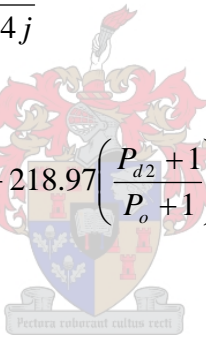
$$\text{For the number of jets, } k_5 = \frac{8}{u} \quad (\text{B26})$$

$$\text{For the } l_j/D \text{ ratio, } k_6 = \frac{D}{l_j} \quad (\text{B27})$$

$$\text{For the station position, } j/l_j, \quad k_7 = \frac{l_j}{4j} \quad (\text{B28})$$

For the exhaust pressure ratio,

$$k_8 = -62.516 \left(\frac{P_{d2} + 1}{P_o + 1} \right)^5 + 188.8 \left(\frac{P_{d2} + 1}{P_o + 1} \right)^4 - 218.97 \left(\frac{P_{d2} + 1}{P_o + 1} \right)^3 + 122.17 \left(\frac{P_{d2} + 1}{P_o + 1} \right)^2 - 33.998 \left(\frac{P_{d2} + 1}{P_o + 1} \right) + 4.5063 \quad (\text{B29})$$



The correct jet diameter is thus:

$$d = d^* \times k_4 \times k_5 \times k_6 \times k_7 \times k_8 \quad (\text{mm}) \quad (\text{B30})$$

B6. The theoretical load capacity – the load coefficient C_l

For $\frac{j}{l_j} = 0.5$ (half-station bearings)

$$1 \leq \frac{l_j}{D} < 1.5, \quad C_l = \frac{1 - l_j/D}{31.25} + 0.173 \quad (\text{B31})$$

$$1.5 < \frac{l_j}{D} < 2, \quad C_l = \frac{1.5 - l_j/D}{13.889} + 0.157 \quad (\text{B32})$$

$$2 < \frac{l_j}{D} \leq 3, \quad C_l = \frac{2.0 - l_j/D}{33.81} + 0.121 \quad (\text{B33})$$

For $\frac{j}{l_j} = 0.25$ (quarter station bearings)

$$1 \leq \frac{l_j}{D} < 1.5, \quad C_l = \frac{1 - \frac{l_j}{D}}{83.333} + 0.266 \quad (\text{B34})$$

$$1.5 < \frac{l_j}{D} < 2, \quad C_l = \frac{1.5 - \frac{l_j}{D}}{26.316} + 0.260 \quad (\text{B35})$$

$$2 < \frac{l_j}{D} \leq 3, \quad C_l = \frac{2.0 - \frac{l_j}{D}}{14.493} + 0.241 \quad (\text{B36})$$

The theoretical load capacity in Newtons is

$$W = 0.1 \times C_l \times l_j \times D \times (P_o - P_{d2}) \quad (\text{N}) \quad (\text{B37})$$

where the length and diameter of the journal are expressed in millimetres and the pressure drop over the journal is expressed in bars.

If annular jets are used:

$$W_{\text{annular}} = 0.7 \times W \quad (\text{N}) \quad (\text{B38})$$

The bearing radial stiffness is, $K_{\text{rad}} = \frac{2000W}{MRC}$ (N/m) (B39)

where the load capacity is in Newtons, and the MRC is in millimetres.

Bearing angular stiffness, $K_{\text{ang}} = \frac{K_{\text{rad}} \times l_j^2}{16 \times 10^6}$ (N·m/rad) (B40)

with the radial stiffness in Newtons per meter and the bearing length in millimetres.

B7. The theoretical flow rate

$$\text{For } P_o - P_{d2} = 0.68 \text{ bar, } fr^* = 10^{3.171 \log_{10} MRC + 0.986} \quad (\text{kg/s}) \quad (\text{B41})$$

$$\text{For } P_o - P_{d2} = 3.40 \text{ bar, } fr^* = 10^{3.047 \log_{10} MRC + 1.655} \quad (\text{kg/s}) \quad (\text{B42})$$

$$\text{For } P_o - P_{d2} = 6.12 \text{ bar, } fr^* = 10^{3.033 \log_{10} MRC + 1.994} \quad (\text{kg/s}) \quad (\text{B43})$$

The MRC is expressed in millimetres. For other pressure drops, linear interpolation can be used. The following correction factors apply to the theoretical flow rate:

$$\text{For the } D/l_j \text{ ratio, } k_9 = \frac{D}{l_j} \quad (\text{B44})$$

$$\text{For the gauge pressure ratio, } k_3 = 3.661K_{go}^2 + 0.9793K_{go} + 0.0214$$

The applicable flow rate for a quarter station bearing is thus:

$$fr = fr^* \times k_9 \times k_3 \quad (\text{kg/s}) \quad (\text{B45})$$

and if a half-station jet position is used, the applicable flow rate is:

$$fr = 0.5 \times fr^* \times k_9 \times k_3 \quad (\text{kg/s}) \quad (\text{B46})$$

B8. The theoretical pressure drop over the jet

The jet area for simple jets is:

$$A_{simple} = \pi \left(\frac{d}{2000} \right)^2 \quad (\text{m}^2) \quad (\text{B47})$$

where d is the jet diameter in millimetres. The jet area for annular jets is:

$$A_{annular} = \frac{\pi \times d \times MRC}{1 \times 10^6} \quad (\text{m}^2) \quad (\text{B48})$$

where the MRC and jet diameter are in millimetres.

The velocity at the jet throat is defined as

$$v = \frac{2 \times fr \times \frac{j}{l_j}}{u \times C_d \times \rho_d \times A} \quad (\text{m/s}) \quad (\text{B49})$$

where the bearing flow rate fr is given in kg/s, C_d is the discharge coefficient (taken as 0.8), ρ_d is the density at the throat of the jet (kg/m^3) and A is the jet area (m^2). However the density at the throat is not know, as the pressure at the throat has not yet been calculated – so at this stage an estimate of the density is used (Crowe, 2001).

The static pressure at the jet throat is defined as

$$P_{d2} = (P_o + 1) \left[1 - \frac{\gamma - 1}{2} \left(\frac{v}{\sqrt{\gamma R (T + 273.15)}} \right)^2 \right]^{\frac{\gamma}{\gamma - 1}} - 1 \quad (\text{bar, gauge}) \quad (\text{B50})$$

with the supply pressure expressed in bars gauge and the gas temperature in degrees Celsius.

The density at the throat using the calculated throat pressure, P_{d2} , is

$$\rho_d = \rho_o \left(\frac{P_d + 1}{P_o + 1} \right)^{\frac{1}{\gamma}} \quad (\text{kg/m}^3) \quad (\text{B51})$$

The new calculated density would be used to calculate a new iterated value for the velocity, and so the iterations would continue until the change in calculated density is within the desired precision. The critical pressure ratio over the jet is defined as

$$\frac{P_{d2} + 1}{P_o + 1} = \left(\frac{2}{\gamma + 1} \right)^{\frac{\gamma}{\gamma - 1}}$$

which for air ($\gamma = 1.4$) is 0.528. The pressure ratio over the jet must be kept higher than this value in order to ensure the jets are not choked, which could cause bearing instability.

B9. The axial bearing load capacity and stiffness

$$\text{Load capacity, } W_t = P_{d2} \times 0.1 \times \pi \times \frac{\left(r_s^2 - \left(\frac{D}{2} \right)^2 \left(2 \ln \left(\frac{2r_s}{D} + 1 \right) \right) \right)}{2 \ln \left(\frac{2r_s}{D} \right)} \quad (\text{N}) \quad (\text{B52})$$

where D is the journal diameter (mm), r_s is the larger thrust radius, and P_{d2} is the journal exhaust pressure in bars gauge.

$$\text{Axial stiffness, } K_{ax} = \frac{2880W_t}{MAC}, \quad (\text{N/m}) \quad (\text{B53})$$

with the MAC expressed in millimetres.

Appendix C: Computer Programs

C1. Bearing design program

%This program calculates specific parameters required for a successful aerostatic bearing design, using %thrust faces fed by the journal exhaust. Jet position can be either 1/4 or 1/2 station.

```
clear all
```

```
close all
```

```
clc
```

```
%%Input Data%%
```

```
D=25;           %Journal diameter, mm
L=45;           %Journal length, mm
b=25;           %Maximum radius of thrust face, mm
                %Minimum radius is the shaft radius, D/2
ho=0.0180;      %Mean radial clearance, mm
ht=0.0300;      %Mean axial clearance, mm
Po=6.0;         %Supply pressure, bar gauge
Pd2=0.6;        %Estimated journal exhaust pressure, bar gauge
jet=['annular']; %Specify the jet type
%jet=['simple.'];
l=0.25*L;       %Jet station, either 0.25 or 0.5 x L
n=8;            %Number of jets per row
Kgo=0.7;        %Desired gauge pressure ratio
T=15;          %Mean gas temperature, degrees Celcius
k=1.4;         %Specific heat ratio for gas
R=287;         %Gas constant, J/kg.K
```

```
%%Reference data%%
```

```
P_ref=6.8;      %Reference supply pressure, bar gauge
ho_ref=0.0254/2; %Reference journal clearance, mm
```

```
%%Calculating the ball park load capacity%%
```

```
u=2;
```

```
if D>=127
```

```
    disp(['Warning: Journal diameter is larger than calculations can predict.'])
```

```
end
```

```
if D<25.4
```

```
    u=L^3/2679.25-L^2/9.477+9.688*L-72.061;
```

```
    ld=(D/25.4)*u;
```

```

elseif D>=25.4 & D<50.8
    low=L^3/2679.25-L^2/9.477+9.688*L-72.061;
    u=-L^2/14.5038+15.271*L-136.1156;
    ld=((D-25.4)/25.4)*(u-low)+low;
elseif D>=50.8 & D<76.2
    low=-L^2/14.5038+15.271*L-136.1156;
    u=-L^2/29.008+18.0375*L-213.515;
    ld=((D-50.8)/25.4)*(u-low)+low;
elseif D>=76.2 & D<101.6
    low=-L^2/29.008+18.0375*L-213.515;
    u=L^2/19.3383+9.5459*L+180.153;
    ld=((D-76.2)/25.4)*(u-low)+low;
elseif D>=101.6 & D<127
    low=L^2/19.3383+9.5459*L+180.153;
    u=L^2/14.5038+7.8823*L+556.0277;
    ld=((D-101.6)/25.4)*(u-low)+low;
end

ld_coeff=(Po-Pd2)/P_ref;           %Load coefficient due to supply pressure
W_bp=ld*ld_coeff;                 %Ball park load capacity of bearing, N

%%Calculating the ball-park flow rate%%
fr_bp=(D*9.6277/L);              %Bearing flow rate, l/min, Fig 3.2, Pg 70
fr_coeff1=0.0433*(Po-Pd2)^2-0.1441*(Po-Pd2)+0.26; %Flow rate pressure coefficient 1, Fig 3.2, Pg 70
fr_coeff2=(ho/ho_ref)^3;         %Flow rate clearance coefficient 2, Fig 3.2, Pg 70
fr_coeff3=3.6607*Kgo^2+0.9793*Kgo+0.0214;
                                %Flow rate gauge ratio coefficient 3, Fig 3.12, Pg 82, only @ 6.7 bar gauge
fr_bp=fr_bp*fr_coeff1*fr_coeff2*fr_coeff3; %Ball park flow rate, l/min

%%Calculating the ball-park jet diameter%%
if Kgo>0.8
    disp(['Warning: Pressure ratio is larger than calculations can predict.'])
end

if jet=='simple.'
    %Calculating feed hole diameter for simple orifices%
    if Kgo<0.4
        u=40.743*(ho^2)^2+2.5253*(ho^2)-0.0046;
        d=(Kgo/0.4)*u;
    elseif Kgo>=0.4 & Kgo<0.6

```

```

low=40.743*(ho*2)^2+2.5253*(ho*2)-0.0046;
u=70.968*(ho*2)^2+3.3091*(ho*2)-0.0043;
d=((Kgo-0.4)/0.2)*(u-low)+l;

```

```
elseif Kgo>=0.6 %& Kgo<0.8
```

```

low=70.968*(ho*2)^2+3.3091*(ho*2)-0.0043;
u=106.29*(ho*2)^2+4.7109*(ho*2)-0.0027;
d=((Kgo-0.6)/0.2)*(u-low)+low;

```

```
else
```

```
disp('Error - gauge pressure ratio is out of bounds')
```

```
end
```

```
hole_coeff1=-0.0133*(Po-Pd2)^2+0.1847*(Po-Pd2)+0.5314; %First hole pressure coefficient, Fig 3.8, Pg77
```

```
hole_coeff2=sqrt(8/n); %Second hole jet coefficient, Fig 3.8, Pg77
```

```
hole_coeff3=sqrt(D/L); %Third hole L/D coefficient, Fig 3.8, Pg77
```

```
hole_coeff4=sqrt(L/(4*I)); %Fourth hole station coefficient, Fig 3.8, Pg77
```

```
hole_coeff5=-56.932*((Pd2+1)/(Po+1))^5+156.78*((Pd2+1)/(Po+1))^4-163.77*((Pd2+1)/(Po+1))^3+...
80.629*((Pd2+1)/(Po+1))^2-19.485*((Pd2+1)/(Po+1))+2.7696; %Fourth hole Pd2/Po coeffic., Fig 3.19,
```

```
Pg88
```

```
d=d*hole_coeff1*hole_coeff2*hole_coeff3*hole_coeff4*hole_coeff5;
```

```
elseif jet=='annular'
```

```
%Calculating feed hole diameter for annular orifices%
```

```
if Kgo<0.4
```

```

u=7838.2*(ho*2)^3-355.32*(ho*2)^2+8.9176*(ho*2)-0.0114;
d=(Kgo/0.4)*u;

```

```
elseif Kgo>=0.4 & Kgo<0.6
```

```

low=7838.2*(ho*2)^3-355.32*(ho*2)^2+8.9176*(ho*2)-0.0114;
u=464.87*(ho*2)^2-0.0548*(ho*2)-0.0025;
d=((Kgo-0.4)/0.2)*(u-low)+low;

```

```
elseif Kgo>=0.6 %& Kgo<0.8
```

```

low=464.87*(ho*2)^2-0.0548*(ho*2)-0.0025;
u=1009.7*(ho*2)^2-1.565*(ho*2)+0.0066;
d=((Kgo-0.6)/0.2)*(u-low)+low;

```

```
else
```

```
disp('Error - Gauge pressure ratio is out of bounds')
```

```
end
```

```
hole_coeff1=-0.0197*(Po-Pd2)^2+0.323*(Po-Pd2)+0.1546; %First hole pressure coefficient, Fig 3.10, Pg79
```

```
hole_coeff2=(8/n); %Second hole jet coefficient, Fig 3.10, Pg79
```

```
hole_coeff3=D/L; %Third hole L/D coefficient, Fig 3.8, Pg77
```

```
hole_coeff4=L/(4*I); %Fourth hole station coefficient, Fig 3.8, Pg77
```

The Design and Development of a High-speed Aerostatic Bearing

```
hole_coeff5=-62.516*((Pd2+1)/(Po+1))^5+188.8*((Pd2+1)/(Po+1))^4-218.97*((Pd2+1)/(Po+1))^3+...
```

```
122.17*((Pd2+1)/(Po+1))^2-33.998*((Pd2+1)/(Po+1))+4.5063;%Fourth hole Pd2/Po coeffic., Fig 3.19, Pg88
```

```
d=d*hole_coeff1*hole_coeff2*hole_coeff3*hole_coeff4*hole_coeff5;
```

```
else
```

```
disp(['Error - incorrect jet type specified - either "simple" or "annular"'])
```

```
end
```

```
dd=d*10;dd=round(dd);dd=dd/10;
```

```
%%Calculating the theoretical load coefficient and capacity%%
```

```
if I/L==0.5
```

```
if L/D>=1 & L/D<1.5
```

```
CI=(1-L/D)/31.25+0.173;
```

```
elseif L/D>=1.5 & L/D<2
```

```
CI=(1.5-L/D)/13.889+0.157;
```

```
elseif L/D>=2 & L/D<3
```

```
CI=(2-L/D)/23.81+0.121;
```

```
else
```

```
disp('Error - L/D ratio is out of bounds.')
```

```
CI=0;
```

```
end
```

```
elseif I/L==0.25
```

```
if L/D>=1 & L/D<1.5
```

```
CI=(1-L/D)/83.333+0.266;
```

```
elseif L/D>=1.5 & L/D<2
```

```
CI=(1.5-L/D)/26.316+0.260;
```

```
elseif L/D>=2 & L/D<3
```

```
CI=(2-L/D)/14.493+0.241;
```

```
else
```

```
disp('Error - L/D ratio is out of bounds.')
```

```
CI=0;
```

```
end
```

```
else
```

```
disp('Error - Jet station incorrect, must be either 0.25 x L or 0.5 x L')
```

```
CI=0;
```

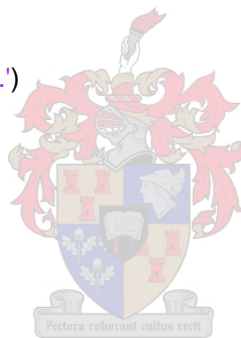
```
end
```

```
W=0.1*CI*L*D*(Po-Pd2); %Theoretical load capacity, N
```

```
if jet=='annular'
```

```
W=W*0.7;
```

```
end
```



```

Krad=2*W/(ho/1000);           %Radial stiffness, N/m
Kang=Krad*(L/1000)^2/16;      %Angular stiffness, Nm/rad

%%Calculating the flow rate, kg/s%%
if Po-Pd2>=0.68 & Po-Pd2<3.4
    low=10^(3.170678*log10(ho)+0.986312);
    u=10^(3.047364*log10(ho)+1.654843);
    fr=(u-low)*((Po-Pd2)-0.68)/(3.4-0.68)+low;
elseif Po-Pd2>=3.4 & Po-Pd2<=6.122
    low=10^(3.047364*log10(ho)+1.654843);
    u=10^(3.033464*log10(ho)+1.993894);
    fr=(u-low)*((Po-Pd2)-3.4)/(6.12-3.4)+low;
else
    disp('Error-Pressure drop Po-Pd2 is out of bounds')
end
fr=fr*D/L;                    %Flow rate compensaion for bearing dimensions, Fig 3.17, Pg 87
fr=fr*fr_coeff3;              %Flow rate gauge ratio coefficient 3, Fig 3.12, Pg 82, only @ 6.7 bar gauge

if l==0.5*L
    fr=fr*0.5;                %Flow rate compensation for 1/2 station jet position, Fig 3.17, Pg 87
end

%%Confirming pressure drops with flow theory%%
a=sqrt(k*R*(T+273.15));       %Speed of sound at throat, m/s
crit_rat=(2/(k+1))^(k/(k-1)); %Critical pressure ratio across jet, Pd1/Po

if jet=='simple.'
    jet_area=pi*(d/2000)^2;
elseif jet=='annular'
    jet_area=pi*(d/1000)*(ho/1000); %Jet area, m2
else
    disp('Error - jet must be specified as either "simple." or "annular"')
end

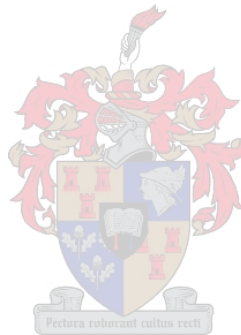
po=((Po+1)*100000/(R*(T+273.15))); %Density of gas, supply conditions, kg/m3
Cd=0.8;                          %Coeff of discharge
pd_i=0.8*po;                       %Initial estimate of density of gas at throat, kg/m3
diff=1;

```

The Design and Development of a High-speed Aerostatic Bearing

```
while diff>0.1
v=(fr*2*I)/(n*L*Cd*pd_i*jet_area);    %Velocity at throat, m/s
Pd1=(Po+1)*(1-((k-1)/2)*(v/a)^2)^(k/(k-1))-1;    %Static pressure at throat, gauge, bar
pd_f=po*((Pd1+1)/(Po+1))^(1/k);    %New iterated throat density
diff=abs(pd_i-pd_f);
pd_i=pd_f;
%pause
end

%%Thrust bearing calculations%%
W_t=(Pd2)*0.1*pi*(b^2-(D/2)^2*(2*log(2*b/D)+1))/(2*log(2*b/D));
    %Axial load capacity
K_ax=2880*W_t/ht;
```



Appendix D: Experimental Data

D1. Sawing tests

Table D1: RMS acceleration values for sawing tests performed with the aerostatic diamond saw (m/s²)

Test	Accelerometer position	
	Clamp	Housing
1	44.17 x 10 ⁻³	29.31 x 10 ⁻³
2	41.17 x 10 ⁻³	28.45 x 10⁻³
3	46.69 x 10 ⁻³	29.16 x 10 ⁻³
4	40.94 x 10 ⁻³	29.18 x 10 ⁻³
5	36.99 x 10⁻³	28.60 x 10 ⁻³
6	48.22 x 10 ⁻³	30.87 x 10⁻³
7	53.64 x 10⁻³	28.54 x 10 ⁻³
Mean	44.55 x 10⁻³	29.16 x 10⁻³

Table D2: RMS acceleration values for sawing tests performed with the conventional diamond saw (m/s²)

Test	Accelerometer position	
	Clamp	Base
1	84.84 x 10 ⁻³	137.82 x 10⁻³
2	94.45 x 10 ⁻³	118.72 x 10 ⁻³
3	105.45 x 10 ⁻³	103.48 x 10 ⁻³
4	164.79 x 10⁻³	91.67 x 10 ⁻³
5	86.28 x 10 ⁻³	99.19 x 10 ⁻³
6	50.78 x 10 ⁻³	96.29 x 10 ⁻³
7	54.37 x 10 ⁻³	98.16 x 10 ⁻³
8	48.55 x 10⁻³	87.28 x 10 ⁻³
9	61.07 x 10 ⁻³	85.57 x 10⁻³
10	140.17 x 10 ⁻³	97.11 x 10 ⁻³
Mean	89.08 x 10⁻³	101.53 x 10⁻³

D2. Specifications of equipment used in the EMA

Modal hammer

PCB Piezotronics

Model: 086C03

Serial Number: 14604

2.13 mV/N

Accelerometer 1

PCB Piezotronics

Model: 353B15

Serial Number 75360

Sensitivity: 10.75 mV/g

Electromagnetic shaker

IMV corporation

Model: VibroPet PET-01

P/N: 460548

Sep 2004

Accelerometer 2

PCB Piezotronics

Model: 353B15

Serial Number 75361

Sensitivity: 10.03 mV/g

Dynamic load cell

Brüel and Kjaer

Type: 8200

Serial Number: 1149723

3.88 pC/N

Accelerometer 3

PCB Piezotronics

Model: 353B15

Serial Number 75613

Sensitivity: 10.28 mV/g

Charge amplifier

Brüel and Kjaer

Type: 2635

Serial Number: 1100007

Polytec laser vibrometer

Polytec laser measuring instruments

Model: PVD 100

1% accuracy calibration range: 20 – 22 000 Hz.

Siglab processing unit

Serial Number: 11564

Manufactured: 48500 Kato Rd.

Fremont, CA

94538-7385

High pass filter used: 5 kHz

Low pass filter used: None

Measurement range used: 20 mm/s

